Foreword

The Advanced Microwave Scanning Radiometer (AMSR) is a multi-frequency, dual-polarized microwave radiometer that detects microwave emissions from the Earth's surface and atmosphere. Various geophysical parameters, particularly those related to water (H2O), can be estimated from AMSR data. In addition to the proven parameters such as water vapor, precipitation, and sea surface wind speed, novel geophysical parameters, including sea surface temperature and soil moisture, are expected to be retrieved by using new frequency channels. The largest ever microwave radiometer antenna enables us to perform continuous global observation with high spatial resolution. Long-term record of AMSR measurements will play an important role in climate change monitoring as well as in providing indispensable information for understanding the Earth's climate system, including water and energy circulation. Near real-time products will be used for investigating satellite data assimilation into weather forecasting models and will contribute to improving forecast accuracy.

AMSR is scheduled to be launched on board the Advanced Earth Observing Satellite-II (ADEOS-II) in 2002. ADEOS-II is an integrated observing platform with multiple sensors covering the spectrum from visible to microwave frequencies. In addition to AMSR, a combination of these sensors will provide a means of examining the Earth's phenomena from various aspects. AMSR-E on the NASA EOS Aqua is an enhanced model of the AMSR on ADEOS-II. AMSR-E also will be launched in 2002. I hope that these papers will be helpful to utilize the AMSR and AMSR-E data of which will be available soon.

March 2002

Dr. Akira Shibata
AMSR lead scientist

EORC Bulletin/Technical Report

-Special Issue on AMSR Retrieval Algorithms-

Contents

Page No

Development of AMSR and AMSR-E retrieval algorithms at EORC

Keiji Imaoka
Earth Observation Research Center / NASDA

1. Introduction

The Advanced Microwave Scanning Radiometer (AMSR) is a multi-frequency, dual-polarized microwave radiometer that detects microwave emissions from the Earth's surface and atmosphere. Various geophysical parameters, particularly those related to water (H_2O), can be estimated from AMSR data. In addition to the proven parameters such as water vapor, precipitation, and sea surface wind speed, novel geophysical parameters, including sea surface temperature and soil moisture, are expected to be retrieved by using new frequency channels. The largest ever microwave radiometer antenna enables us to perform continuous global observation with high spatial resolution. Long-term records of AMSR measurements will play an important role in climate change monitoring as well as in providing indispensable information for understanding the Earth's climate system, including water and energy circulation. Near-real-time products will be used for investigating satellite data assimilation into weather forecasting models and will contribute to improving forecast accuracy. In this technical report, we will summarize the theoretical basis and descriptions of an each retrieval algorithm.

2. Algorithm Development

NASDA issued the first Research Announcement (RA) in October 1995 to solicit standard algorithms for ADEOS-II AMSR and GLI. Standard algorithms will be installed at the Earth Observation Center (EOC) to operationally produce Level 2 and 3 geophysical products. The AMSR sensor team was organized based on this announcement. After the decision of providing AMSR-E to the EOS PM-1 satellite, the team has also been responsible for AMSR-E standard algorithms. Retrieval algorithms for AMSR standard products have been evaluated and selected through an algorithm inter-comparison process by the AMSR sensor team. The inter-comparison procedure was mainly based on a comparison between in-situ or aircraft data and retrieved geophysical parameters from brightness temperatures of existing space-borne sensors such as the Special Sensor Microwave/Imager (SSM/I). Although the comparison showed little differences in the performance of algorithms, the day-1 algorithms (i.e. the algorithms at launch phase) and supporting PIs were selected based on this result (e.g. whether he or she could meet report and program deadlines). The AMSR algorithm selection board was held at EORC in May 2000. As a result of this board, the soil moisture product was re-defined as a research product at the launch phase due to the difficulties of accurate retrieval. For geophysical parameters with two algorithm candidates, one algorithm was selected as standard and the other one was positioned as a research algorithm. Current day-1 algorithm investigators are listed in Table 1. These day-1 algorithms will be used at EOC during the first six-months after launch. After the real AMSR brightness temperatures are obtained, this selection will be re-shuffled, and one algorithm will be selected based on its real performance. Through the 2nd Research Announcement, several PIs have joined the project as research algorithm investigators. These PIs will be added to the list at the next opportunity.

Table 1. Day-1 algorithms for AMSR and AMSR-E

Geophysical products	Standard	Research
Integrated water vapor	Takeuchi	-
Integrated cloud liquid water	Wentz	-
Precipitation	Petty	Liu
Sea surface wind speed	Shibata	-
Sea surface temperature	Shibata	Wentz
Sea ice concentration	Comiso	-
Snow depth	Chang	Koike
Soil moisture	-	Njoku, Jackson, Paloscia, Koike

3. Algorithm integration testing

EORC is responsible for proto-typing and testing the AMSR data retrieval system. We asked the algorithm PIs to submit their source codes for retrieval algorithms. Prior to this request, NASDA distributed the “common library,” that is a kind of interfacing toolkit between the PI environment and the NASDA processing system. We can easily integrate PI source codes written using this common library into our processing system. During fiscal year 2000, we were provided the algorithms twice, corresponding to the distributions of different version of the common library. Since the AMSR has not flown yet, no real brightness temperatures are available to check the condition and performance of each algorithm. As the input data for the testing, we generated AMSR simulated brightness temperatures by using existing microwave radiometer data such as SSM/I and SMMR with slight corrections for incident angle and center frequencies. Radiative transfer calculations were also used for nonexistent frequency channels. Through the algorithm integration testing, we have confirmed that most of the algorithms functioned properly. Since the AMSR simulated data are not ideal, we have to wait for the real AMSR data to investigate algorithm performance. Sample browse images of the retrieval results are shown in Fig. 1.

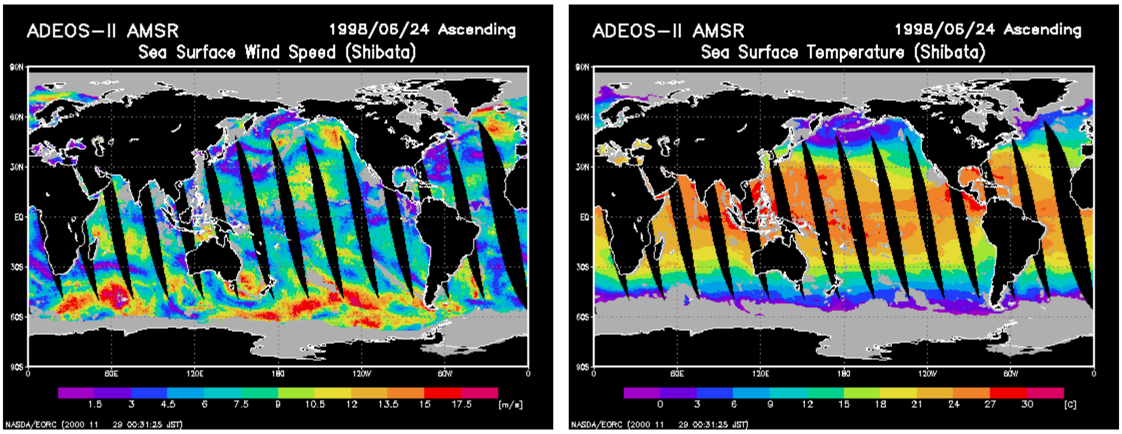

Fig. 1. Global images generated by AMSR processing system at EORC. Images of sea surface wind speed (left) and sea surface temperature (right) are shown as examples. Input data are AMSR simulated ascending passes on June 24, 1998.

Algorithm theoretical basis document (ATBD) of the algorithm to derive total water vapor content from ADEOS-II/AMSR

Yoshiaki Takeuchi
Numerical Prediction Division / Japan Meteorological Agency

1. Introduction

An algorithm for the physical-statistical retrieval of total water vapor content (PWA) from satellite-based microwave radiometers named AMSR has been described. Input data are brightness temperature (T_{BB}) of 6 channels, i.e.19 GHz V/H, 24 GHz V/H, 37 GHz V/H, observation time, latitude and longitude. Ancillary data are land/open sea/sea ice map data, sea surface temperature data, sea surface wind speed data, temperature data at 850 hPa, and a few look-up tables. Sea surface temperature (SST), sea surface wind speed (Vs), and temperature at 850hPa (T85) is given by global analysis, forecast data or another standard product by AMSR etc.. Several flags, which are related to success/failure and accuracy, are added to each result by the algorithm.

The characteristics of this algorithm are the follows:

- One retrieval is carried out by measurement in a field of view.
- The algorithm is applicable over open sea region.
- The algorithm is based on single-layer atmosphere model.
- Complicated radiative transfer calculation and detailed temperature and water vapor profile as a first guess are unnecessary.
- An iteration calculation is included to obtain atmospheric transmittance and vertical mean atmospheric temperature. The iteration is stable.
- Dependencies of surface emissivity to SST and Vs are considered statistically.
- Ancillary data such as land/open sea/sea ice map, surface temperature, and sea surface wind speed and temperature at 850 hPa are needed.
- The dynamic range of the algorithm is 0-70 Kg/m^2 for PWA.
- The algorithm assures that the probability of retrieved PWA is equivalent to that of radio sonde of match-up data set.
- Flag related to success/failure and accuracy is added to each result.

2. Background and forward model

This algorithm is based on a model consists of single-layer atmosphere and sea surface as shown in Fig.2.1. The atmosphere includes water vapor and cloud liquid water as absorber and emitter at microwave region. Sea surface is assumed to be Fresnel reflection surface.

Tr is square of atmospheric transmittance at a frequency and a satellite zenith angle (θs) , namely microwave emitting direction. Ta is vertical mean temperature of atmosphere at the frequency and θs . Tr and Ta depend on vertical profile of temperature, water vapor, and cloud liquid water. We ignore the dependency of Tr and Ta to polarization since the dependency can be detected only in heavy rain region by measurements of higher frequency.

To be exact, Ta also depends slightly the direction of radiation transfer, i.e. upward or downward, due to inhomogeneity of temperature and water vapor. In our algorithm, we define Ta as the average of upward Ta and downward Ta.

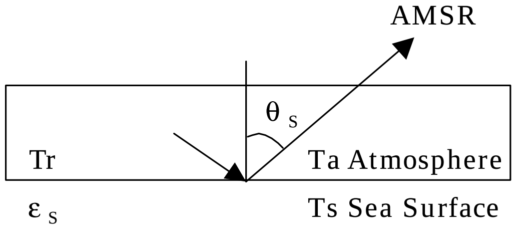

Fig.2.1 RT model for AMSR

ε_{SV} and ε_{SH} are sea surface emissivity for vertical and horizontal polarization, respectively. ε_{SV} and ε_{SH} depend on frequency, SST, Vs and θs.

By using the model, the difference between brightness temperature of vertical polarization T_V and that of horizontal polarization T_H at a frequency is given by

$$T_V - T_H = Tr*(\varepsilon_{SV} - \varepsilon_{SH})*T, \qquad ($$

where

$$T \equiv Ta + (SST-Ta)/Tr^{1/2}.$$

Brightness temperature T_{BB} at a frequency is related to Tr and ε_S as

$$T_{BB} = \alpha*\{1-Tr*(1-\varepsilon_S)\},$$

where vertical mean temperature of atmosphere-sea surface system α is defined by

$$\alpha \equiv Ta+(SST-Ta)*Tr^{1/2}*\varepsilon_S/\{1-(1-\varepsilon_S)*Tr\}. \qquad (2.4)$$

From (2.3) and (2.4), Tr and Ta can be calculated by the following manner. For 19 GHz V/H, 24 GHz V and 37 GHz V/H,

1) ε_S is calculated from frequency, SST, Vs, and θ s.

2) Initial value of Tr is set.

$$Tr = \exp(-0.2) \qquad (2.5)$$

3) Ta can be approximated as a function of Tr and T85. Ta is determined from a two dimensional look-up table.

$$Ta = Ta(Tr,T85) \qquad (2.6)$$

4) α is calculated by (2.4).

5) Tr is calculated using the formula derived from (2.3).

$$Tr = (1-T_{BB}/\alpha)/(1-\varepsilon_S) \qquad (2.7)$$

6) From 5), two Tr value can be calculated both for vertical polarization channel and horizontal polarization channel, then calculate new Tr by taking square root of the product of Tr_V and Tr_H.

$$Tr = (Tr_V*Tr_H)^{1/2} \qquad (2.8)$$

7) Step 3) to 6) are repeated until Tr value is converged. Usually, this iteration calculation is stable and converges within a few iterations.

When Tr is obtained, optical depth of atmosphere τ is calculated from Tr.

$$\tau = -0.5*\ln(Tr) \qquad (2.9)$$

τ is summation of optical depth of water vapor and optical depth of cloud liquid water.

$$\tau = (kv*PWA + kl*LWC)/\cos(\theta s), \qquad (2.10)$$

where PWA is total water vapor content, LWC is total cloud liquid water content, kv is vertical mean absorption coefficient of water vapor, kl is vertical mean absorption coefficient of cloud liquid water. kv and kl depend vertical profile of temperature, water vapor and cloud liquid water and frequency. Tr at 19GHz is denoted as Tr19. Tr at 24GHz is denoted as Tr24. From (2.9) and (2.10), PWA can be calculated by the following formula:

$$PWA = 0.5*\cos(\theta s)*\{kl24*\ln(Tr19)-kl19*\ln(Tr24)\} /(kv24*kl19-kv19*kl24). \qquad (2.11)$$

However, it is difficult to calculate kv and kl theoretically because kv and kl depend vertical profile of temperature, water vapor and liquid water. Instead of the theoretical calculation, we construct water vapor content index (PWI) as a linear combination of ln(Tr19) and ln(Tr24). In addition, we introduce a cloud liquid water index CWI, which is deduced from (2.1) and (2.2) for 19GHz and 37GHz.

$$CWI = \ln\{(T19V-T19H)/(\varepsilon_S 19V-\varepsilon_S 19H)/T19\} - \ln\{(T37V-T37H)/(\varepsilon_S 37V-\varepsilon_S 37H)/T37\} \quad (2.12)$$

where T19 and T37 are given by

$$T19 = Ta19+(SST-Ta19)/Tr19^{1/2}, \quad (2.13)$$
$$T37 = Ta37+(SST-Ta37)/Tr37^{1/2}. \quad (2.14)$$

In conclusion, PWI is calculated by

$$PWI = \beta*\ln(Tr19)-\ln(Tr24)+\gamma*CWI \quad (2.15)$$

where β and a constant γ is determined so that we can get the maximum correlation between PWI and PWA from radio sonde in the match-up data set described later. Since it is found that β strongly depends SST, we give β as a function of SST. β is given at SST of 0°C , 16°C , 24°C , 28°C , 30°C and β at any SST is given by interpolating these values.

3 Detail description of the algorithm

This section describes the detail of the algorithm. Input data of these programs are shown in Table 3.1 and flags added by the algorithm are summarized in Table 3.2.

3.1 Land and sea ice mask

Land and sea ice is masked by using land/ocean flag and sea ice data. Sea ice data will be revised once a day by using the latest data such as AMSR sea ice level-3 products. If a FOV of AMSR is judged as land or sea ice, then the flag 'land/sea ice' is set and the retrieval is quit.

3.2 Quality check of AMSR brightness temperature data

1) Brightness temperatures T19V, T19H, T24V, T24H, T37V and T37H are within the range from 90 K to 300 K,
2) T19V-T19H is positive,
3) T24V-T24H is positive,
4) T37V-T37H is positive, and
5) T24V-T19V is less than TBD K.

If above conditions are false, then the flag 'bad TBB' is added and the retrieval is quit.

3.3 Quality check of ancillary data

If sea surface wind speed (Vs) of ancillary data set is out of the range from 0 to 60 m/s, a default value Vs = 5 m/s is set.

If sea surface temperature (SST) of ancillary data set is out of the range from 0 to 35 °C, the flag 'others' is added and the retrieval is quit.

If temperature at 850 hPa (T85) of ancillary data set is out of the range from 200 K to 300 K, a default value T85 = SST - 10 K is set.

3.4 Calculation of index of cloudiness and its quality check

Sea surface emissivities (ε_S) at 19 GHz V/H, 24 GHz V/H, and 37 GHz V/H are calculated from frequency, SST, and θ_S theoretically, and then corrected with SST and Vs. λ is given by look-up table and δ is a constant.

$$\varepsilon_{SH} = 1-(1-\varepsilon_{SH})\lambda^{\delta}, \ \varepsilon_{SV} = 1-(1-\varepsilon_{SV})\lambda^{\delta -1} \quad (3.1)$$

The index of cloudiness is calculated by the formula:

$$CCI = \ln\{(T19V-T19H)/(\varepsilon_S 19V-\varepsilon_S 19H) /(T37V-T37H)*(\varepsilon_S 37V-\varepsilon_S 37H)\}. \qquad (3.2)$$

If the CCI is less than -0.05, the flag 'bad TBB' is added and the retrieval is quit.

3.5 Decision of clear, cloudy, or rain category

If T19V is larger than 240 K, it is assumed to be rainy condition.
If T19V is less than 240 K and CCI is larger than 0.2, it is assumed to be cloudy condition.
If T19V is less than 240 K and CCI is less than 0.2, it is assumed to be clear condition.

3.6 Calculation of vertical mean temperature of atmosphere and square of atmospheric transmittance and their quality check

For each channel, i.e. 19GHz V/H, 24GHz V/H, 37GHz V/H, square of atmospheric transmittance (Tr) and vertical mean temperature of atmosphere (Ta) are calculated from temperature at 850hPa (T85), sea surface emissivity (ε_S), sea surface temperature (SST) and brightness temperature iteratively. The details are described at section 2. In the case that Ta cannot be obtained or α is less than T_{BB}, the flag 'bad TBB' is added and the retrieval is quit.

3.7 Calculations of water vapor content index and cloud liquid water index

Water vapor content index (PWI) is calculated from (2.15) and (2.12).

3.8 Conversion PWI to water vapor content

PWI is converted to total water vapor content (PWA, kg/m^2) using a look-up table. If PWI is out of range of look-up table, the flag 'low accuracy' is added.

flag	description	availability
normal	normal (clear condition)	available
cloudy	normal (cloudy condition)	available
rainy	normal (rainy condition)	available
land/sea ice	land or sea ice region	inavailable
low accuracy	accuracy may be low	available
bad TBB	brightness temperature is illegal	inavailable
others	no sea surface temperature failure of sea surface emissivity estimation	inavailable

Table 3.1 List of input data for PWA retrievals

flag	description	availability
normal	normal (clear condition)	available
cloudy	normal (cloudy condition)	available
rainy	normal (rainy condition)	available
land/sea ice	land or sea ice region	inavailable
low accuracy	accuracy may be low	available
bad TBB	brightness temperature is illegal	inavailable
others	no sea surface temperature failure of sea surface emissivity estimation	inavailable

Table 3.2 Summary of flags added by the algorithm

3.9 Heavy rain correction to water vapor content

In the case of rainy category, PWA is corrected by T19H/T19V.

If T19H/T19V is less than 0.884, PWA = PWA-1.51.
If T19H/T19V is more than 0.884, PWA = PWA+(T19H/T19V-0.884)/(0.960-0.884)*16.5-1.51.

4. How to construct look-up tables and to decide retrieval coefficients

This section describes the procedure for determination of several coefficients used in the algorithm, proposal for a match-up data set, from which the coefficients are determined. The scheme of coefficient decision should be in automated processing appropriate for operational retrievals.

Look-up tables and several coefficients for the retrieval are derived from a match-up data set between AMSR observation and in-situ observation, i.e., radio sonde data of international radio sonde network. The GANAL analysis provided by JMA and AMSR level3 products should be included in the match-up data set.
Table 4.1 shows proposed list of elements to be included in the match-up data set. The data set is also used in validation.

Radio sonde at island or coastal area
Sonde ID
Observation time (min)
Pressure (hPa), Temperature (K), Relative humidity (%) at all level
PWA from sonde profile (kg/m^2)
PWA from GANAL at sonde station (kg/m^2)
AMSR observation within 150km from sonde station
Observation time (min)
Latitude, Longitude (deg)
Time lag between sonde obs. & AMSR obs. (min)
Distance between sonde station & AMSR FOV (km)
Granule number, Line number, Swath number
AMSR Land /Ocean flag
AMSR incidence angle (deg)
AMSR sun azimuth/ elevation (deg)
AMSR brightness temperature (K)
PWA from AMSR observation (kg/m^2)
GANAL interpolated at AMSR FOV
SST (K), Surface wind U,V (m/s)
Temperature (K), Relative humidity (%)
PWA from GANAL at AMSR FOV (kg/m^2)
AMSR level3 interpolated at AMSR FOV
SST (K), Sea Ice
Sea Winds level3 interpolated at AMSR FOV
Surface wind U,V (m/s)

Table 4.1 Proposed list of coefficients for retrieval and validation

4.1 Look-up table of sea surface emissivity correction on sea surface temperature and sea surface wind

A coefficient λ defined as (4.1) is calculated with the match-up data set between radio sonde, sea surface temperature, sea surface wind and AMSR T_{BB}. Then the results are compiled into two dimensional table with axis of SST and Vs.

$$\lambda = \{(1-T_{BBH}/\alpha_H)/(1-T_{BBV}/\alpha_V)\} /\{(1-\varepsilon_{SH})/(1-\varepsilon_{SV})\} \qquad (4.1)$$

4.2 Look-up table to calculate Ta from T85 and Tr

Ta and Tr is calculated theoretically from temperature and water vapor profile observed by radio sonde in the match-up data set. The results are compiled as a look-up table to get Ta from T85 and Tr. Optical parameters used in the radiative transfer calculation are refered to Janssen (1993).

4.3 Coefficients to construct PWI from linear combination of atmospheric optical depth at 24GHz and that at 19GHz.

It is estimated with a match-up data set between radio sonde data and T_{BB} so that the correlation between PWI and PWA accomplish maximum. The β(Ts) and constants γ and δ will be determined after launch of AMSR.

4.4 Look-up table from PWI to PWA

The look-up table is designed as the provability of PWA with AMSR retrievals is equivalent to that of PWA with radio sonde.

4.5 Coefficients for heavy precipitation correction for water vapor content

It is estimated with a match-up data set between PWA sonde and PWA AMSRnocor and T19H/T19V.

Finally, It is noted that careful treatment of producing match-up data set is essential to attain the accuracy require-ment of AMSR total water vapor amount. Well checked radio sonde data, brightness temperature data, and good collocation data should be selected. Consistency between the match-up data set and a validation data set is also essential to evaluate the algorithm correctly.

Reference

Janssen, M.A. Ed.(1993) Atmospheric Remote Sensing by Microwave Radiomeroty,
Jhon Wiley & Sons, Inc., 572pp.

AMSR Ocean Algorithm

Frank J. Wentz
Remote Sensing Systems

1. Overview and Background Information

1.1. Introduction

With the advent of well-calibrated satellite microwave radiometers, it is now possible to obtain long time series of geophysical parameters that are important for studying the global hydrologic cycle and the Earth's radiation budget. Over the world's oceans, these radiometers simultaneously measure profiles of air temperature and the three phases of atmospheric water (vapor, liquid, and ice). In addition, surface parameters such as the near-surface wind speed, the sea-surface temperature, and the sea ice type and concentration can be retrieved. A wide variety of hydrological and radiative processes can be studied with these measurements, including air-sea and air-ice interactions (i.e., the latent and sensible heat fluxes, fresh water flux, and surface stress) and the effect of clouds on radiative fluxes. The microwave radiometer is truly a unique and valuable tool for studying our planet.

This Algorithm Theoretical Basis Document (ATBD) focuses on the Advanced Microwave Scanning Radiometer (AMSR) that is scheduled to fly in December 2000 on the NASA EOS-PM1 platform. AMSR will measure the Earth's radiation over the spectral range from 7 to 90 GHz. Over the world's oceans, it will be possible to retrieve the four important geophysical parameters listed in Table 1. The rms accuracies given in Table 1 come from past investigations and on-going simulations that will be discussed. Rainfall can also be retrieved, which is discussed in a separate AMSR ATBD.

We are confident that the expected retrieval accuracies for wind, vapor, and cloud will be achieved. The Special Sensor Microwave Image (SSM/I) and the TRMM microwave imager (TMI) have already demonstrated that these accuracies can be obtained. The AMSR wind retrievals will probably be more accurate than that of SSM/I and less affected by atmospheric moisture. A comparison between sea surface temperatures (SST) from TMI with buoy measurements indicate an rms accuracy between 0.5 and 0.7 K. One should keep in mind that part of the error arises from the temporal and spatial mismatch between the buoy measurement and the 50 km satellite footprint. Furthermore, the satellite is measuring the temperature at the surface the ocean (about 1 mm deep) whereas the buoy is measuring the bulk temperature near 1 m below the surface. There are still some concerns with regards to the sea-surface temperature retrieval, which are discussed in Section 1.5.

This document is version 2 of the AMSR Ocean Algorithm ATBD. The primary difference between this version and the earlier version is that the emissivity model for the 10.7 GHz has been updated using data from TMI. In addition, there are several small updates to the radiative transfer model (RTM).

Table 1. Expected Retrieval Accuracy for the Ocean Products

Geophysical Parameter	Rms Accuracy
Sea-surface temperature T_S	0.5 K
Near-surface wind speed W	1.0 m/s
Vertically integrated (i.e., columnar) water vapor V	1.0 mm
Vertically integrated cloud liquid water L	0.02 mm

1.2. Objectives of Investigation

There are two major objectives of this investigation. The first is to develop an ocean retrieval algorithm that will retrieve T_S, W, V, and L to the accuracies specified in Table 1. These products will be of great value to the Earth science community. The second objective is to improve the radiative transfer model (RTM) for the ocean surface and non-raining atmosphere. The 6.9 and 10.7 GHz channels on AMSR will provide new information on the RTM at low frequencies. Experience has shown that these two objectives are closely linked. A better understanding of the RTM leads to more accurate retrievals. A better understanding of the RTM also leads to new remote sensing techniques such as using radiometers to measure the ocean wind vector.

1.3. Approach to Algorithm Development

Radiative transfer theory provides the relationship between the Earth's brightness temperature T_B (K) as measured by AMSR and the geophysical parameters T_S, W, V, and L. This ATBD addresses the inversion problem of finding T_S, W, V, and L given T_B. We place a great deal of emphasis on developing a highly accurate RTM. Most of our AMSR work thus far has been the development and refinement of the RTM. This work is now completed, and Section 2 describes the RTM in considerable detail.

The importance of the RTM is underscored by the fact that AMSR frequency, polarization, and incidence angle selection is not the same as previous satellite radiometers. Table 2 compares AMSR with other radiometer systems. Albeit some of the differences are small, they are still significant enough to preclude developing AMSR algorithms by simply using existing radiometer measurements. The differences in frequencies and incidence angle must be taken into account when developing AMSR algorithms.

2. Geophysical Model for the Ocean and Atmosphere

2.1. Introduction

The key component of the ocean parameter retrieval algorithm is the geophysical model for the ocean and atmosphere. It is this model that relates the observed brightness temperature (T_B) to the relevant geophysical parameters. In remote sensing, the specification of the geophysical model is sometimes referred to as the forward problem in contrast to the inverse problem of inverting the model to retrieve parameters. An accurate specification of the geophysical model is the crucial first step in developing the retrieval algorithm.

2.2. Radiative Transfer Equation

We begin by deriving the radiative transfer model for the atmosphere bounded on the bottom by the Earth's surface and on the top by cold space. The derivation is greatly simplified by using the absorption-emission approximation in which radiative scattering from large rain drops and ice particles is not included. Over the spectral range from 6 to 37 GHz, the absorption-emission approximation is valid for clear and cloudy skies and for light rain up to about 2 mm/h. The results of *Wentz and Spencer* [1997] indicate that only 3% of the SSM/I observations over the oceans viewed rain rates exceeding 2 mm/h. Thus, the absorption-emission model to be presented will be applicable to about 97% of the AMSR ocean observations.

In the microwave region, the radiative transfer equation is generally given in terms of the radiation brightness temperature (T_B), rather than radiation intensity. So we first give a brief discussion on the relationship between radiation intensity and T_B. Let P_λ denote the power within the wavelength range $d\lambda$, coming from a surface area dA, and propagating into the solid angle $d\Omega$. The specific intensity of radiation I_λ is then defined by

$$P_\lambda = I_\lambda \cos\theta_i \, d\lambda \, dA \, d\Omega \tag{1}$$

The specific intensity is in units of erg/s-cm^3-steradian. The angle θ_i is the incidence angle defined as the angle between the surface normal and the propagation direction. For a black body, I_λ is given by Planck's law to be [*Reif*, 1965]

$$I_\lambda = \frac{2hc^2}{\lambda^5\left[\exp\left(hc/\lambda kT\right)-1\right]} \tag{2}$$

where c is the speed of light (2.998×10^{10} cm/s), h is Planck's constant (6.626×10^{-27} erg-s), k is Boltzmann's constant (1.381×10^{-16} erg/K), λ (cm) is the radiation wavelength, and T (K) is the temperature of the black body. Consider a surface that is emitting radiation with a specific intensity I_λ. Then the brightness temperature T_B for this surface is defined as the temperature at which a black body would emit the radiation having specific intensity I_λ. In the microwave region, the exponent in (2) is small compared to unity, and (2) can be easily inverted to give T_B in terms of I_v.

$$T_B = \frac{\lambda^4 I_\lambda}{2kc} \tag{3}$$

This approximation is the well known Rayleigh Jeans approximation for $\lambda >> hc/kT$.

In terms of T_B, the differential equation governing the radiative transfer through the atmosphere is

$$\frac{\partial T_B}{\partial s} = -\alpha(s)\left[T_B(s) - T(s)\right] \tag{4}$$

where the variable s is the distance along some specified path through the atmosphere. The terms $\alpha(s)$ and T(s) are the absorption coefficient and the atmospheric temperature at position s. Equation (4) is simply stating that the change in T_B is due to (1) the absorption of radiation arriving at s and (2) to emission of radiation emanating from s. We let s = 0 denote the Earth's surface, and let s = S denote the top of the atmosphere (i.e., the elevation above which $\alpha(s)$ is essentially zero).

Two boundary conditions that correspond to the Earth's surface at the bottom and cold space at the top are applied to equation (4). The surface boundary conditions states that the upwelling brightness temperature at the surface $T_{B\uparrow}$ is the sum of the direct surface emission and the downwelling radiation that is scattered upward by the rough surface [*Peake*, 1959].

$$T_{B\uparrow}(\mathbf{k_i},0) = E(\mathbf{k_i})T_S + \frac{\sec\theta_i}{4\pi}\int_0^{\pi/2}\sin\theta_s d\theta_s \int_0^{2\pi} d\varphi_s T_{B\downarrow}(\mathbf{k_s},0)\left[\sigma_{o,c}(\mathbf{k_s},\mathbf{k_i}) + \sigma_{o,\times}(\mathbf{k_s},\mathbf{k_i})\right] \tag{5}$$

where the first T_B argument denotes the propagation direction of the radiation and the second argument denotes the path length s. The unit propagation vectors $\mathbf{k_i}$ and $\mathbf{k_s}$ denote the direction of the upwelling and downwelling radiation, respectively. In terms of polar angles in a coordinate system having the z-axis normal to the Earth's surface, these propagation vectors are given by

$$\mathbf{k_i} = \left[\cos\varphi_i \sin\theta_i, \sin\varphi_i \sin\theta_i, \cos\theta_i\right] \tag{6a}$$

$$\mathbf{k_s} = -\left[\cos\varphi_s \sin\theta_s, \sin\varphi_s \sin\theta_s, \cos\theta_s\right] \tag{6b}$$

The first term in (5) is the emission from the surface, which is the product of the surface temperature T_S and the surface emissivity $E(\mathbf{k_i})$. The second term is the integral of downwelling radiation $T_{B\downarrow}(\mathbf{k_s})$ that is scattered in direction $\mathbf{k_i}$. The integral is over the 2π steradian of the upper hemisphere. The rough surface scattering is characterized by the bistatic normalized radar cross sections (NRCS) $\sigma_{o,c}(\theta_s,\theta_i)$ and $\sigma_{o,\times}(\theta_s,\theta_i)$. These cross sections specify what fraction of power coming from $\mathbf{k_s}$ is scattered into $\mathbf{k_i}$. The subscripts c and × denote co-polarization (i.e., incoming and outgoing polarization are the same) and cross-polarization (i.e., incoming and outgoing polarizations are orthogonal), respectively. The cross sections also determine the surface reflectivity $R(\mathbf{k_i})$ via the following integral.

$$R(\mathbf{k_i}) = \frac{\sec\theta_i}{4\pi}\int_0^{\pi/2}\sin\theta_s d\theta_s \int_0^{2\pi} d\varphi_s \left[\sigma_{o,c}(\mathbf{k_s},\mathbf{k_i}) + \sigma_{o,\times}(\mathbf{k_s},\mathbf{k_i})\right] \tag{7}$$

The surface emissivity $E(\mathbf{k_i})$ is given by Kirchhoff's law to be

$$\mathrm{E}(\mathbf{k_i}) = 1 - \mathrm{R}(\mathbf{k_i}) \tag{8}$$

It is important to note that equations (5) an (7) provide the link between passive microwave radiometry and active microwave scatterometry. The scatterometer measures the radar backscatter coefficient, which is simply $\sigma_{o,c}(-\mathbf{k_i},\mathbf{k_i})$.

The upper boundary condition for cold space is

$$T_{B\downarrow}(\mathbf{k_s},S) = T_C \tag{9}$$

This simply states that the radiation coming from cold space is isotropic and has a magnitude of $T_C = 2.7$ K.

The differential equation (4) is readily solved by integrating and applying the two boundary conditions (5) and (9). The result for the upwelling brightness temperature at the top of the atmosphere (i.e., the value observed by Earth-orbiting satellites) is

$$T_{B\uparrow}(\mathbf{k_i},S) = T_{BU} + \tau\left[ET_S + T_{B\Omega}\right] \tag{10}$$

where T_{BU} is the contribution of the upwelling atmospheric emission, τ is the total transmittance from the surface to the top of the atmosphere, E is the Earth surface emissivity given by (8), and $T_{B\Omega}$ is the surface scattering integral in (5). The atmospheric terms can be expressed in terms of the transmittance function $\tau(s_1,s_2)$

$$\tau(s_1,s_2) = \exp\left(-\int_{s_1}^{s_2} ds\ \alpha(s)\right) \tag{11}$$

which is the transmittance between points s_1 and s_2 along the propagation path $\mathbf{k_s}$ or $\mathbf{k_i}$. The total transmittance τ in (10) is given by

$$\tau = \tau(0,S) \tag{12}$$

and the upwelling and downwelling atmosphere emissions are given by

$$T_{BU} = \int_0^S ds\ \alpha(s)\ T(s)\ \tau(s,S) \tag{13a}$$

$$T_{BD} = \int_0^S ds\ \alpha(s)\ T(s)\ \tau(0,s) \tag{13b}$$

The sky radiation scattering integral is

$$T_{B\Omega} = \frac{\sec\theta_i}{4\pi}\int_0^{\pi/2}\sin\theta_s d\theta_s \int_0^{2\pi} d\varphi_s (T_{BD} + \tau T_C)\left[\sigma_{o,c}(\mathbf{k_s},\mathbf{k_i}) + \sigma_{o,\times}(\mathbf{k_s},\mathbf{k_i})\right] \tag{14}$$

Thus, given the temperature T_S and absorption coefficient α at all points in the atmosphere and given the surface bistatic cross sections, T_B can be rigorously calculated. However, in practice, the 3-dimensional specification of T_S and α over the entire volume of the atmosphere is not feasible, and to simplify the problem, the assumption of horizontal uniformity is made. That is to say, the absorption is assumed to only be a function of the altitude h above the Earth's surface, i.e., $\alpha(s) = \alpha(h)$. To change the integration variable from ds to dh, we note that for the spherical Earth

$$\frac{\partial s}{\partial h} = \frac{1+\delta}{\sqrt{\cos^2\theta + \delta(2+\delta)}} \tag{15}$$

where θ is either θ_i or θ_s, $\delta = h/R_E$, and R_E is the radius of the Earth. In the troposphere $\delta << 1$, and an excellent approximation for $\theta < 60°$ is,

$$\frac{\partial s}{\partial h} = \sec\theta \tag{16}$$

With this approximation and the assumption of horizontal uniformity, the above equations reduce to the following expressions.

$$\tau(h_1, h_2, \theta) = \exp\left(-\sec\theta \int_{h_1}^{h_2} dh\ \alpha(h)\right) \tag{17}$$

$$\tau = \tau(0, H, \theta_i) \tag{18}$$

$$T_{BU} = \sec\theta_i \int_0^H dh\ \alpha(h)\ T(h)\ \tau(h, H, \theta_i) \tag{19a}$$

$$T_{BD} = \sec\theta_s \int_0^H dh\ \alpha(h)\ T(h)\ \tau(0, h, \theta_s) \tag{19b}$$

Thus, the brightness temperature computation now only requires the vertical profiles of T(h) and $\alpha(h)$ along with the surface cross sections. The following two sections discuss the atmospheric model for $\alpha(h)$ and the sea-surface model for the cross sections, respectively. In closing, we note that the AMSR incidence angle is 55° and hence approximation (16) is quite valid, with one exception. In the scattering integral, θ_s goes out to 90°, and in this case we use (15) to evaluate the integral.

2.3. Model for the Atmosphere

In the microwave spectrum below 100 GHz, atmospheric absorption is due to three components: oxygen, water vapor, and liquid water in the form of clouds and rain [*Waters*, 1976]. The sum of these three components gives the total absorption coefficient (napers/cm).

$$\alpha(h) = \alpha_O(h) + \alpha_V(h) + \alpha_L(h) \tag{20}$$

Numerous investigators have studied the dependence of the oxygen and water vapor coefficients on frequency ν (GHz), temperature T (K), pressure P (mb), and water vapor density ρ_V (g/cm^3) [*Becker and Autler*, 1946; *Rozenkranz*, 1975; *Waters*, 1976; *Liebe*, 1985]. To specify α_O and α_V as a function of (ν, T, P, ρ_V) we use the *Liebe* [1985] expressions with one modification. The self-broadening component of the water vapor continuum is reduced by a factor of 0.52 (see below). The liquid water coefficient α_L comes directly from the Rayleigh approximation to Mie scattering and is a function of T and the liquid water density ρ_L (g/cm^2) (see below). Figure 3 shows the total atmospheric absorption for each component. Results for three water vapor cases (10, 30, and 60 mm) are shown. The cloud water content is 0.2 mm. This corresponds to a moderately heavy non-raining cloud layer.

Let A_I denote the vertically integrated absorption coefficient.

$$A_I = \int_0^H dh\ \alpha_I(h) \tag{21}$$

where h is the height (cm) above the Earth's surface and subscript I equals O, V, or L. Equations (17) and (18) then give the total transmittance to be

$$\tau = \exp[-\sec\theta_i (A_O + A_V + A_L)] \tag{22}$$

Assuming for the moment that the atmospheric temperature is constant, i.e., T(h) = T, then the integrals in equations (19) can be exactly evaluated in closed form to yield

$$T_{BU} = T_{BD} = (1 - \boldsymbol{t})T \tag{23}$$

In reality, the atmospheric temperature does vary with h, typically decreasing at a lapse rate of about -5.5 C/km in the lower to mid troposphere. In view of (23), we find it convenient to parameterize the atmospheric model in terms of the following upwelling and downwelling effective air temperatures:

$$\mathrm{T_U} = \mathrm{T_{BU}} \,/\, (1 - \tau) \tag{24a}$$

$$\mathrm{T_D} = \mathrm{T_{BD}} \,/\, (1 - \tau) \tag{24b}$$

These effective temperatures are indicative of the air temperature averaged over the lower to mid troposphere. Note that in the absence of significant rain, T_U and T_D are very similar in value, with T_U being 1 to 2 K colder.

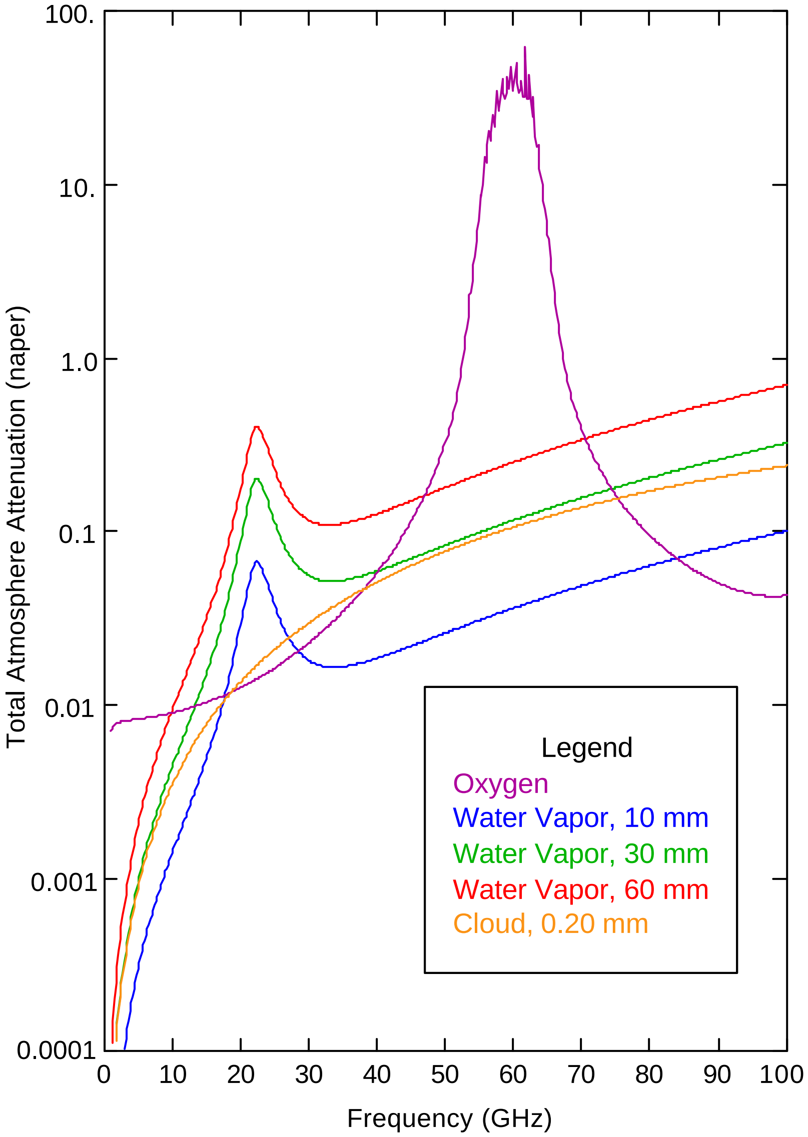

Fig. 3. The atmospheric absorption spectrum for oxygen, water vapor, and cloud water. Results for three water vapor cases (10, 30, and 60 mm) are shown. The cloud water content is 0.2 mm which corresponds to a moderately heavy non-raining cloud layer.

In view of the above equations, one sees that the atmospheric model can be parameterized in terms of the following 5 parameters:

1. Upwelling effective temperature T_U
2. Downwelling effective temperature T_D
3. Vertically integrated oxygen absorption A_O
4. Vertically integrated water vapor absorption A_V
5. Vertically integrated liquid water absorption A_L

To study the properties of the first four parameters, we use a large set of 42,195 radiosonde flights launched from small islands [*Wentz*, 1997]. These radiosonde reports provide air temperature T(h), air pressure p(h), and water vapor density $\rho_V(h)$ at a number of levels in the troposphere. From these data, the coefficients α_O and α_V are computed from the *Liebe* [1985] expressions, except that the water vapor continuum term is modified as discussed in the next paragraph. Performing the numerical integrations as indicated above, T_U, T_D, A_O, and A_V are found for each radiosonde flight. In addition, the vertically integrated water vapor V is also computed.

$$V = 10 \int_0^H dh \;\; r_V(h) \tag{25}$$

where $\rho_V(h)$ is in units of g/cm^3, and the leading factor of 10 converts from g/cm^2 to mm.

Wentz [1997] computed A_V directly from collocated SSM/I and radiosonde observations. At 19, 22, and 37 GHz, the Liebe A_V was found to be 4%, 3%, and 20% higher than the SSM/I-derived value, respectively. To quote *Liebe* [1985]: 'Water vapor continuum absorption has been a major source of uncertainty in predicting millimeter wave attenuation rates, especially in the window ranges.' The frequency of 37 GHz is in a water vapor window and is most affected by the continuum. It should be noted that Liebe also needed to rely on combined radiometer-radiosonde measurements to infer the continuum in the 6 to 37 GHz region. Liebe's data set in this spectral region is rather limited and does not contain any 37 GHz observations. We believe the SSM/I method of deriving A_V is more accurate than Liebe's method, and hence adjust the *Liebe* [1985] water vapor spectrum so that it will agree with the SSM/I results. We find that very good agreement is obtained by reducing the self-broadening component of the water vapor continuum by a factor of 0.52. After this adjustment, the agreement at all three frequencies is within ± 1%.

Figure 4 shows the T_D values computed from the 42,195 radiosondes plotted versus V. Three frequencies are shown (19, 22, and 37 GHz), and the curves are quite similar. The solid lines in the figure show equation (26), and vertical bars show the ± one standard deviation of T_D derived from the radiosondes. For low to moderate values of V (0 to 40 mm), T_D increases with V, and above 40 mm, T_D reaches a relatively constant value of 287 K. The T_U versus V curves (not shown) are very similar except that T_U is 1 to 2 K colder. The following least-square regressions are found to be a good approximation of the T_D, T_U versus V relationship:

(26a)

$$T_U = T_D + b_6 + b_7 V \tag{26b}$$

where

$$T_V = 273.16 + 0.8337\ V - 3.029 \times 10^{-5} V^{3.33} \qquad V \le 48 \tag{27a}$$

$$T_V = 301.16 \qquad V > 48 \tag{27b}$$

and

$$\varsigma(T_S - T_V) = 1.05 \cdot T_S - T_V \cdot 1 - \frac{(T_S - T_V)^2}{1200} \qquad |T_S - T_V| \le 20K \tag{27c}$$

$$V(T_S - T_V) = \text{sign}(T_S - T_V) \cdot 14K \qquad |T_S - T_V| > 20K \tag{27d}$$

V is in units of millimeters and all temperatures are in units of Kelvin. When evaluating (26a), the expression is linearly extrapolated when V is greater than 58 mm. We have included a small additional term that is a function of the difference between the sea-surface temperature T_S and T_V, which represents the sea-surface temperature that is typical for water vapor V. The term $V(T_S - T_V)$ accounts for the fact that the effective air temperature is typically higher (lower) for the case of unusually warm (cold) water. The T_V versus V relationship was obtained by regressing the climatology sea-surface temperature at the radiosonde site to V derived from the radiosondes. Over the full range of V, the rms error in approximation (26) is typically about 3 K. Table 4 gives the b_0 through b_7 coefficients for all 8 AMSR frequencies.

The vertically integrated oxygen absorption A_O is nearly constant over the globe, with a small dependence on the air temperature. We find the following expression to be a very good approximation for A_O:

$$A_O = a_{O1} + a_{O2}(T_D - 270) \tag{28}$$

Table 4 gives the a_O coefficients for the 8 AMSR frequencies, and Table 5 gives the rms error in this approximation for the 8 frequencies. At 23.8 GHz and below, the error is negligible, being 0.0003 napers or less. At 36.5 GHz, the error is still quite small, being 0.0008 napers. Note that 0.001 napers roughly corresponds to a T_B error of 0.5 K. For the 50.3 and 52.8 GHz oxygen band channels, the error is considerably larger, but (28) is not used for the oxygen band channels. Rather the oxygen band channels can be used to retrieve T_D.

Table 4. Model Coefficients for the Atmosphere

Freq. (GHz)	6.93E+0	10.65E+0	18.70E+0	23.80E+0	36.50E+0	50.30E+0	52.80E+0	89.00E+0
b_0 (K)	239.50E+0	239.51E+0	240.24E+0	241.69E+0	239.45E+0	242.10E+0	245.87E+0	242.58E+0
b_1 (K mm^{-1})	213.92E–2	225.19E–2	298.88E–2	310.32E–2	254.41E–2	229.17E–2	250.61E–2	302.33E–2
b_2 (K mm^{-2})	–460.60E–4	–446.86E–4	–725.93E–4	–814.29E–4	–512.84E–4	–508.05E–4	–627.89E–4	–749.76E–4
b_3 (K mm^{-3})	457.11E–6	391.82E–6	814.50E–6	998.93E–6	452.02E–6	536.90E–6	759.62E–6	880.66E–6
b_4 (K mm^{-4})	–16.84E–7	–12.20E–7	–36.07E–7	–48.37E–7	–14.36E–7	–22.07E–7	–36.06E–7	–40.88E–7
b_5	0.50E+0	0.54E+0	0.61E+0	0.20E+0	0.58E+0	0.52E+0	0.53E+0	0.62E+0
b_6 (K)	–0.11E+0	–0.12E+0	–0.16E+0	–0.20E+0	–0.57E+0	–4.59E+0	–12.52E+0	–0.57E+0
b_7 (K mm^{-1})	–0.21E–2	–0.34E–2	–1.69E–2	–5.21E–2	–2.38E–2	–8.78E–2	–23.26E–2	–8.07E–2
a_{O1}	8.34E–3	9.08E–3	12.15E–3	15.75E–3	40.06E–3	353.72E–3	1131.76E–3	53.35E–3
a_{O2} (K^{-1})	–0.48E–4	–0.47E–4	–0.61E–4	–0.87E–4	–2.00E–4	–13.79E–4	–2.26E–4	–1.18E–4
a_{V1} (mm^{-1})	0.07E–3	0.18E–3	1.73E–3	5.14E–3	1.88E–3	2.91E–3	3.17E–3	8.78E–3
a_{V2} (mm^{-2})	0.00E–5	0.00E–5	–0.05E–5	0.19E–5	0.09E–5	0.24E–5	0.27E–5	0.80E–5

Table 5. RMS Error in Oxygen and Water Vapor Absorption Approximation

Freq. (GHz)	6.93	10.65	18.70	23.80	36.50	50.30	52.80	89.00
Oxygen, A_O	0.0002	0.0002	0.0003	0.0003	0.0008	0.0062	0.0163	0.0009
Vapor, A_V	0.0001	0.0002	0.0011	0.0013	0.0025	0.0042	0.0046	0.0129

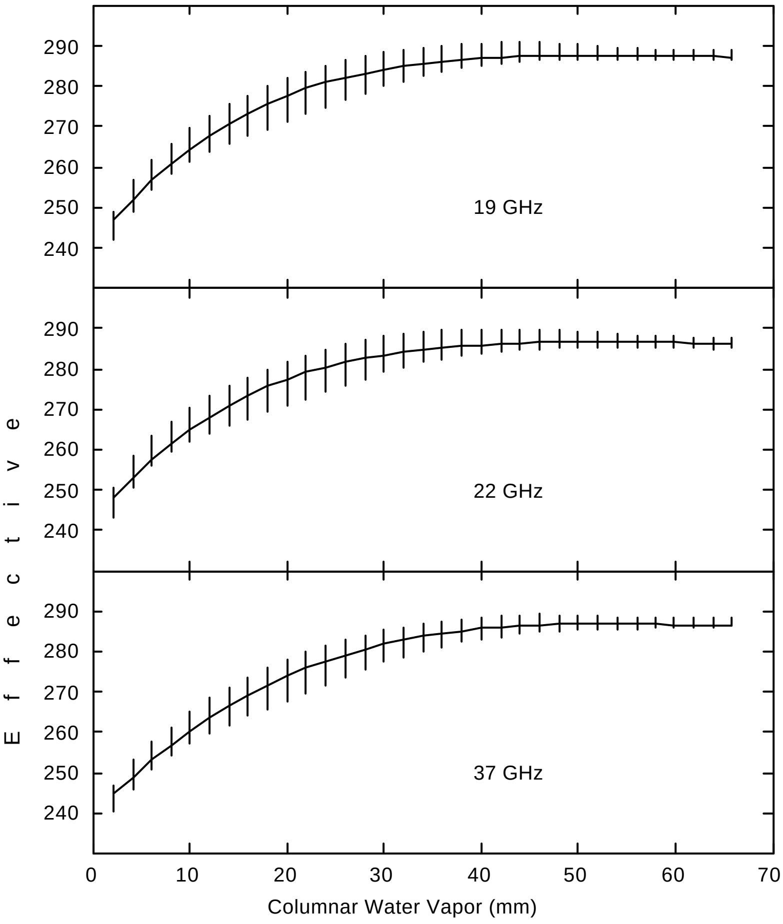

Fig. 4. The effective air temperature T_D for downwelling radiation plotted versus the RAOB columnar water vapor. The solid curve is the model value, and the vertical bars are the ± one standard deviation of T_D derived from radiosondes.

The vapor absorption A_V is primarily a linear function of V, although there is a small second order term. We find the following expression is a good approximation for A_V:

$$A_V = a_{V1}V + a_{V2}V^2 \tag{29}$$

Table 4 gives the a_V coefficients for the 8 AMSR frequencies, and Table 5 gives the rms error in this approximation for the 8 frequencies. For the 6.9 and 10.7 AMSR channels, the rms error in this approximation is negligible, being 0.0002 napers or less. In the 18.7 to 36.5 range, the error remains relatively small (0.001 to 0.0025 napers), but not negligible.

The final atmospheric parameter to be specified is the vertically integrated liquid water absorption A_L. When the liquid water drop radius is small relative to the radiation wavelength, the absorption coefficient α_L (cm^{-1}) is given by the Rayleigh scattering approximation [*Goldstein*, 1951]:

$$\alpha_L = \frac{6\pi\rho_L(h)}{\lambda\rho_o}\,\mathrm{Im}\left(\frac{1-\varepsilon}{2+\varepsilon}\right) \tag{30}$$

where λ is the radiation wavelength (cm), $\rho_L(h)$ is the density (g/cm^3) of cloud water in the atmosphere given as a function of h, ρ_o is the density of water ($\rho_o \approx 1$ g/cm^3), and ε is the complex dielectric constant of water. Note that the dielectric constant varies with temperature and hence is also a function of h. Substituting (30) into (21) gives

$$A_L = \frac{0.6\pi L}{\lambda}\,\mathrm{Im}\left(\frac{1-\varepsilon}{2+\varepsilon}\right) \tag{31}$$

where L is the vertically integrated liquid water (mm) given by

$$L = 10\int_0^H dh\;\rho_L(h) \tag{32}$$

The leading factor of 10 converts from g/cm^2 to mm. In deriving (31), we have assumed the cloud is at a constant temperature. For the more realistic case of the temperature varying with height, ε should be evaluated at some mean effective temperature for the cloud. The specification of ε as a function of temperature and frequency is given in Section 2.4. An excellent approximation for (31) is found to be

$$A_L = a_{L1}\left[1 - a_{L2}(T_L - 283)\right] L \tag{33}$$

where T_L is the mean temperature of the cloud, and the a_L coefficients are given in Table 6 for the 8 AMSR frequencies. The error in this approximation is ≤ 1% over the range of T_L from 273 to 288 K, which is negligible compared to other errors such as the uncertainty in specifying the cloud temperature T_L. Note that in the retrieval algorithm, the error in specifying T_L only effects the retrieved value of L. The retrieval of the other parameters only requires the spectral ratio of A_L, which is essentially independent of T_L due to the fact that a_{L2} is spectrally flat.

In the absence of rain, the cloud droplets are much smaller than the radiation wavelengths being considered, and equations (31) and (33) are valid. When rain is present, Mie scattering theory must be used to compute A_L. For light rain not exceeding 2 mm/h and for frequencies between 6 and 37 GHz, the Mie scattering computations give the following approximation [*Wentz and Spencer*, 1998]:

Table 6. Coefficients for Rayleigh Absorption and Mie Scattering.

Freq (GHz)	6.93	10.65	18.70	23.80	36.50	50.30	52.80	89.00
a_{L1}	0.0078	0.0183	0.0556	0.0891	0.2027	0.3682	0.4021	0.9693
a_{L2}	0.0303	0.0298	0.0288	0.0281	0.0261	0.0236	0.0231	0.0146
a_{L3}	0.0007	0.0027	0.0113	0.0188	0.0425	0.0731	0.0786	0.1506
a_{L4}	0.0000	0.0060	0.0040	0.0020	-0.0020	-0.0020	-0.0020	-0.0020
a_{L5}	1.2216	1.1795	1.0636	1.0220	0.9546	0.8983	0.8943	0.7961

$$A_R = a_{L3}\cdot\left[1 + a_{L4}\cdot(T_L - 283)\right]\cdot H\cdot R^{a_{L5}} \tag{34a}$$

The rain column height H (in km) can be approximated by:

$$H = 1 + 0.14\cdot(T_S - 273) - 0.0025\cdot(T_S - 273)^2 \qquad \text{if } T_S < 301 \tag{34b}$$

$$H = 2.96 \qquad \text{if } T_S \geq 301, \tag{34c}$$

where T_S denotes the sea surface temperature (in K). The rain rate R (in mm/h) is related to the liquid cloud water density L by

$$L = 0.18 \cdot 1 + \sqrt{HR}\ . \qquad (34d)$$

In deriving (34a) we have used a *Marshall and Palmer* [1948] drop size distribution.

2.4. Dielectric Constant of Sea-Water and the Specular Sea Surface

A key component of the sea-surface model is the dielectric constant ε of sea water. The parameter is a complex number that depends on frequency ν, water temperature T_S, and water salinity s. The dielectric constant is given by [*Debye*,1929; *Cole and Cole*, 1941] as

$$\varepsilon = \varepsilon_\infty + \frac{\varepsilon_S - \varepsilon_\infty}{1 + \left[j\lambda_R / \lambda \right]^{1-\eta}} - \frac{2j\sigma\lambda}{c} \qquad (35)$$

where $j = \sqrt{-1}$, λ (cm) is the radiation wavelength, ε_∞ is the dielectric constant at infinite frequency, ε_S is the dielectric constant for zero frequency (i.e., the static dielectric constant), and λ_R (cm) is the relaxation wavelength. The spread factor η is an empirical parameter that describes the distribution of relaxation wavelengths. The last term accounts for the conductivity of salt water. In this term, σ (sec^{-1}, Gaussian units) is the ionic conductivity and c is the speed of light.

Several investigators have developed models for the dielectric constant of sea water. In the *Stogryn* [1971] model the salinity dependence of ε_S and λ_R was based on the *Lane and Saxton* [1952] laboratory measurements of saline solutions. Stogryn noted that the Lane- Saxton measurements for distilled water did not agree with those of other investigators. The *Klein and Swift* [1977] model is very similar to Stogryn model except that the salinity dependence of ε_S was based on more recent 1.4 GHz measurements [*Ho and Hall*, 1973; *Ho et al.,* 1974]. Klein-Swift noted that their ε_S was significantly different from that derived from the Lane and Saxton measurements. It appears that there may be a problem with Lane-Saxton measurements. However, in the Klein-Swift model, the salinity dependence of λ_R was still based on the Lane-Saxton measurements. We analyzed all the measurements used by Stogryn and Klein-Swift and concluded that the Lane-Saxton measurements of ε for both distilled water and salt water were inconsistent with the results reported by all other investigators. Therefore, we completely exclude the Lane-Saxton measurements from our model derivation.

The model to be presented is very similar to the Klein-Swift model, with two exceptions. First, since we excluded Lane-Saxton measurements, the salinity dependence of λ_R is different. For cold water (0 to 10 C), our λ_R is about 5% lower than the Klein-Swift value and for warm water (30 C), it is about 1% higher. Second, our value for ε_∞ is 4.44 and the Klein-Swift value is 4.9, which was the value used by Stogryn. In the Stogryn model, $\eta = 0$, whereas in the Klein-Swift model, $\eta = 0.02$. *Grant et al.* [1957] pointed out that the choice of ε_∞ depends on the choice for η, where $\eta = 0 \rightarrow \varepsilon_\infty = 4.9$ and $\eta = 0.02 \rightarrow \varepsilon_\infty = 4.5$. Thus the Klein-Swift value of $\varepsilon_\infty = 4.9$ is probably too high. In terms of brightness temperatures, these λ_R and ε_∞ differences are most significant at the higher frequencies. For example, at 37 GHz and $\theta_i = 55°$, the difference in specular brightness temperatures produced by our model and the Klein-Swift model differ by about ± 2 K. Analyses of SSM/I observations show that our new model, as compared to the Klein-Swift model, produces more consistent retrievals of ocean parameters. For example, using the Klein-Swift model resulted in an abundance of negative cloud water retrievals in cold water. This problem no longer occurs with the new model. (The negative cloud water problem was the original motivation for doing this reanalysis of the ε model.)

We first describe the dielectric constant model for distilled water, and then extend the model to the more general case of a saline solution. The static dielectric constant ε_{S0} for distilled water has been measured by many investigators. The more recent measurements [*Malmberg and Maryott,* 1956; *Archer and Wang*, 1990] are in very good agreement (0.2%). The *Archer and Wang* [1990] values for ε_{S0}, which are reported in the *Handbook of Chemistry and Physics* [*Lide*,1993], are regressed to the following expression:

$$\varepsilon_{S0} = 87.90 \exp(-0.004585\ t_S) \qquad (36)$$

where t_S is the water temperature in Celsius units. The accuracy of the regression relative to the point values for ε_{S0} is 0.01% over the range from 0 to 40 C.

The other three parameters for the dielectric constant of distilled water are the relaxation wavelength λ_{R0}, the spread factor η, and ε_∞. We determine these parameters by a least-squares fit of (35) to laboratory measurements ε_{mea} of the dielectric constant for the range from 1 to 40 GHz. A literature search yielded ten papers reporting ε_{mea} for distilled water. Values for λ_{R0}, η, and ε_∞ are found so as to minimize the following quantity:

$$Q = \left[\mathrm{Re}(\varepsilon - \varepsilon_{mea}) \right]^2 + \left[\mathrm{Im}(\varepsilon - \varepsilon_{mea}) \right]^2 \qquad (37)$$

The relaxation wavelength is a function of temperature [*Grant et al.*, 1957], but it is generally assumed that η and ε_∞ are independent of temperature. The least squares fit yields η = 0.012, ε_∞= 4.44, and

$$\lambda_{R0} = 3.30 \ \exp(-0.0346 \ t_S + 0.00017 \ t_S^2) \tag{38}$$

These values are in good agreement with those obtained by other investigators. Our λ_{R0} agrees with the expression derived by *Stogryn* [1971] to within 1%. The values for η (ε_∞) reported in the literature vary from 0 to 0.02 (4 to 5). Note that using a larger value for η necessitates using a smaller value for ε_∞.

The presence of salt in the water produces ionic conductivity σ and modifies ε_S and λ_R. It is generally assumed that η and ε_∞ are not affected by salinity. *Weyl* [1964] found the following regression for the conductivity of sea water.

$$s = 3.39 \times 10^9 C^{0.892} \exp(-\Delta_t z) \tag{39}$$

$$z = 2.03\times10^{-2} + 1.27\times10^{-4}\Delta_t + 2.46\times10^{-6}\Delta_t^2 - C\left(3.34\times10^{-5} - 4.60\times10^{-7}\Delta_t + 4.60\times10^{-8}\Delta_t^2\right) \tag{40}$$

$$C = 0.5536 \ s \tag{41}$$

$$\Delta_t = 25 - t_S \tag{42}$$

where s and C are salinity and chlorinity in units of parts/thousand. Note that we have converted the Weyl conductivity to Gaussian units of $\sec^{-1}$.

To determine the effect of salinity on ε_S, we use low frequency (1.43 and 2.65 GHz) measurements of ε for sea water and saline solutions [*Ho and Hall*, 1973; *Ho et al.*, 1974]. For the Ho-Hall data, only the real part of the dielectric constant is used in the fit. Klein and Swift reported that the measurements of the imaginary part were in error. To determine the effect of salinity on λ_R, we use higher frequency (3 to 24 GHz) measurements of ε for saline solutions [*Haggis et al.*, 1952; *Hasted and Sabeh*, 1953; *Hasted and Roderick,* 1958]. A least-squares fit to these data shows that the salinity dependence of ε_S and λ_R can be modeled as

$$e_S = e_{S0} \ \exp\left(-3.45\times10^{-3} s + 4.69\times10^{-6} s^2 + 1.36\times10^{-5} s t_S\right) \tag{43}$$

$$l_R = l_{R0} - 6.54\times10^{-3}\left(1 - 3.06\times10^{-2} t_S + 2.0\times10^{-4} t_S^2\right) s \tag{44}$$

The accuracy of the dielectric constant model is characterized in terms of its corresponding specular brightness temperature T_B. For each laboratory measurement of ε, we compute the specular T_B for an incidence angle of 55° using the Fresnel equation (45) below. Two T_B's are computed: one using ε_{mea} and the other using the model ε coming from the above equations. For the low frequency Ho-Hall data, the rms difference between the 'measurement' T_B and the 'model' T_B is about 0.1 K for v-pol and 0.2 K for h-pol. For the higher frequency data set, the rms difference is 0.8 K for v-pol and 0.5 K for h-pol.

Once the dielectric constant is known, the v-pol and h-pol reflectivity coefficients ρ_V and ρ_H for a specular (i.e., perfectly flat) sea surface are calculated from the well-known Fresnel equations

$$\rho_v = \frac{\varepsilon\cos\theta_i - \sqrt{\varepsilon - \sin^2\theta_i}}{\varepsilon\cos\theta_i + \sqrt{\varepsilon - \sin^2\theta_i}} \tag{45a}$$

$$\rho_h = \frac{\cos\theta_i - \sqrt{\varepsilon - \sin^2\theta_i}}{\cos\theta_i + \sqrt{\varepsilon - \sin^2\theta_i}} \tag{45b}$$

where θ_I is the incidence angle. The power reflectivity R is then given by

$$R_{0p} = \left|\rho_p\right|^2 \tag{46}$$

where subscript 0 denotes that this is the specular reflectivity and subscript p denotes polarization.
An analysis using TMI data indicates small deviations from the model function for the dielectric constant of sea water as discussed above. The effect is mainly noted in the v-pol reflectivity. In order to account for these small differences a correction term of

$$\Delta R_{0V} = 4.887\cdot10^{-8} - 6.108\cdot10^{-8}\cdot T_S - 273^3$$

is added to the v-pol reflectivity R_{0V} in (46). The resulting changes in the brightness temperature range from about +0.14K in cold water to about –0.36K in warm water.

2.5. The Wind-Roughened Sea Surface

It is well known that the microwave emission from the ocean depends on surface roughness. A calm sea surface is characterized by a highly polarized emission. When the surface becomes rough, the emission increases and becomes less polarized (except at incidence angles above 55° for which the vertically polarized emission decreases). There are three mechanisms that are responsible for this variation in the emissivity. First, surface waves with wavelengths that are long compared to the radiation wavelength mix the horizontal and vertical polarization states and change the local incidence angle. This phenomenon can be modeled as a collection of tilted facets, each acting as an independent specular surface [*Stogryn,* 1967]. The second mechanism is sea foam. This mixture of air and water increases the emissivity for both polarizations. Sea foam models have been developed by *Stogryn* [1972] and *Smith* [1988]. The third roughness effect is the diffraction of microwaves by surface waves that are small compared to the radiation wavelength. *Rice* [1951] provided the basic formulation for computing the scattering from a slightly rough surface. *Wu and Fung* [1972] and *Wentz* [1975] applied this scattering formulation to the problem of computing the emissivity of a wind-roughened sea surface.

These three effects can be parameterized in terms of the rms slope of the large-scale roughness, the fractional foam coverage, and the rms height of the small-scale waves. Each of these parameters depends on wind speed. *Cox and Munk* [1954], *Monahan and O'Muircheartaigh* [1980], and *Mitsuyasu and Honda* [1982] derived wind speed relationships for the three parameters, respectively. These wind speed relationships in conjunction with the tilt+foam+diffraction model provide the means to compute the sea-surface emissivity. Computations of this type have been done by *Wentz* [1975, 1983] and are in general agreement with microwave observations.

In addition to depending on wind speed, the large-scale rms slope and the small-scale rms height depend on wind direction. The probability density function of the sea-surface slope is skewed in the alongwind axis and has a larger alongwind variance than crosswind variance [*Cox and Munk*, 1954]. The rms height of capillary waves is very anisotropic [*Mitsuyasu and Honda*, 1982]. The capillary waves traveling in the alongwind direction have a greater amplitude than those traveling in the crosswind direction. Another type of directional dependence occurs because the foam and capillary waves are not uniformly distributed over the underlying structure of large-scale waves. *Smith's* [1988] aircraft radiometer measurements show that the forward plunging side of a breaking wave exhibits distinctly warmer microwave emissions than does the back side. In addition, the capillary waves tend to cluster on the downwind side of the larger gravity waves [*Cox*, 1958; *Keller and Wright*, 1975]. The dependence of foam and capillary waves on the underlying structure produces an upwind-downwind asymmetry in the sea-surface emissivity.

The anisotropy of capillary waves is responsible for the observed dependence of radar backscattering on wind direction [*Jones et al.,* 1977]. The upwind radar return is considerably higher than the crosswind return. Also, the modulation of the capillary waves by the underlying gravity waves causes the upwind return to be generally higher than the downwind return. These directional characteristics of the radar return have provided the means to sense wind direction from aircraft and satellite scatterometers [*Jones et al.,* 1979].

To model the rough sea surface, we begin by assuming the surface can be partitioned into foam-free areas and foam-covered areas within the radiometer footprint. The fraction of the total area that is covered by foam is denoted by f. The composite reflectivity is then given by

$$R = (1-f)R_{\text{clear}} + f\kappa R_{\text{clear}} \tag{47}$$

where R_{clear} is the reflectivity of the rough sea surface clear of foam, and the factor κ accounts for the way in which foam modifies the reflectivity. As discussed above, foam tends to decrease the reflectivity, and hence $\kappa < 1$. The reflectivity of the clear, rough sea surface is modeled by the following equation:

$$R_{\text{clear}} = (1-\beta)\ R_{\text{geo}} \tag{48}$$

where R_{geo} is the reflectivity given by the standard geometric optics model (see below) and the factor $1-\beta$ accounts for the way in which diffraction modifies the geometric-optics reflectivity. *Wentz* [1975] showed that the inclusion of diffraction effects is a relatively small effect and hence β small compared to unity.

Combining the above two equations gives

$$R = (1-F)R_{\text{geo}} \tag{49}$$

$$F = f + \beta - f\beta - f\kappa + f\kappa\beta \tag{50}$$

where F is a 'catch-all' term that accounts for both foam and diffraction effects. All of the terms that makeup F are small compared to unity, and the results to be presented show that F < 10%. The reason we lump foam and diffraction effects together is that they both are difficult to model theoretically. Hence, rather than trying to compute F theoretically, we let F be a model parameter that is derived empirically from various radiometer experiments. However, the R_{geo} term is theoretically computed from the geometric optics. Thus, the F term is a measure of that portion of the wind-induced reflectivity that is not explained by the geometric optics.

The geometric optics model assumes the surface is represented by a collection of tilted facets, each acting as an independent reflector. The distribution of facets is statistically characterized in terms of the probability density function $P(S_u,S_c)$ for the slope of the facets, where S_u and S_c are the upwind and crosswind slopes respectively.

Given this model, the reflectivity can be computed from equation (7). To do this, the integration variables θ_s,ϕ_s in (7) are transformed to the surface slope variables. The two equations governing this transformation are

$$\mathbf{k}_\mathbf{s} = \mathbf{k}_\mathbf{i} - 2(\mathbf{k}_\mathbf{i} \cdot \mathbf{n})\mathbf{n} \tag{51}$$

$$\mathbf{n} = \frac{\left[\,-\mathrm{S}_\mathrm{u},\ -\mathrm{S}_\mathrm{c},\ 1\right]}{\sqrt{1+\mathrm{S}_\mathrm{u}^2+\mathrm{S}_\mathrm{c}^2}} \tag{52}$$

where **n** is the unit normal vector for a given facet. Transforming (7) to the S_u,S_c integration variables yields

$$R_{geo} = \frac{\int dS_u \int dS_c P(S_u,S_c)\sqrt{1+S_u^2+S_c^2}\,(\mathbf{k}_\mathbf{i}\cdot\mathbf{n})\left|(\mathbf{p}\cdot\mathbf{h}_\mathbf{i})r_h\mathbf{h}_\mathbf{s}+(\mathbf{p}\cdot\mathbf{v}_\mathbf{i})r_v\mathbf{v}_\mathbf{s}\right|^2\left[c(\mathbf{k}_\mathbf{s})(1-R_\times)+R_\times\right]}{\int dS_u \int dS_c P(S_u,S_c)\sqrt{1+S_u^2+S_c^2}\ (\mathbf{k}_\mathbf{i}\cdot\mathbf{n})} \tag{53}$$

where **p** is the unit vector specifying the reflectivity polarization. The unit vectors $\mathbf{h}_\mathbf{i}$ and $\mathbf{v}_\mathbf{i}$ ($\mathbf{h}_\mathbf{s}$ and $\mathbf{v}_\mathbf{s}$) are the horizontal and vertical polarization vectors associated with the propagation vector $\mathbf{k}_\mathbf{i}$ ($\mathbf{k}_\mathbf{s}$) as measured in the tilted facet reference frame. These polarization vectors in the tilted frame of reference are given by

$$\mathbf{h}_\mathbf{j} = \frac{\mathbf{k}_\mathbf{j}\times\mathbf{n}}{\left|\mathbf{k}_\mathbf{j}\times\mathbf{n}\right|} \tag{54a}$$

$$\mathbf{v}_\mathbf{j} = \mathbf{k}_\mathbf{j}\times\mathbf{h}_\mathbf{j} \tag{54b}$$

where subscript j = i or s. The terms ρ_v and ρ_h are the v-pol and h-pol Fresnel reflection coefficients given above. The last factor in (53) accounts for multiple reflection (i.e., radiation reflecting off of one facet and then intersecting another). $\chi(\mathbf{k}_\mathbf{s})$ is the shadowing function given by *Wentz* [1975], and $R_\times$ is the reflectivity of the secondary intersection. The shadowing function $\chi(\mathbf{k}_\mathbf{s})$ essentially equals unity except when $\mathbf{k}_\mathbf{s}$ approaches surface grazing angles.

The interpretation of (53) is straightforward. The integration is over the ensemble of tilted facets having a slope probability of $P(S_u,S_c)$. The term $\sqrt{1+S_u^2+S_c^2}\ (\mathbf{k}_\mathbf{i}\cdot\mathbf{n})$ is proportional to the solid angle subtended by the tilted facet as seen from the observation direction specified by $\mathbf{k}_\mathbf{i}$. The term $\left|(\mathbf{p}\cdot\mathbf{h}_\mathbf{i})r_h\mathbf{h}_\mathbf{s}+(\mathbf{p}\cdot\mathbf{v}_\mathbf{i})r_v\mathbf{v}_\mathbf{s}\right|^2$ is the reflectivity of the tilted facet. And, the denominator in (53) properly normalizes the integral.

To specify the slope probability we use a Gaussian distribution as suggested by *Cox and Munk* [1954], and we assume that the upwind and crosswind slope variances are the same. Wind direction effects are considered in Section 2.7. Then, the slope probability is given by

$$P(S_u,S_c) = \left(p\Delta S^2\right)^{-1}\exp\left[\frac{-S_u^2-S_c^2}{\Delta S^2}\right] \tag{55}$$

where ΔS^2 is the total slope variance defined as the sum of the upwind and crosswind slope variances. Ocean waves with wavelengths shorter than the radiation wavelength do not contribute to the tilting of facets and hence should not be included in the ensemble specified by $P(S_u,S_c)$. For this reason, the effective slope variance ΔS^2 increases with frequency, reaching a maximum value referred to as the optical limit. The results of *Wilheit and Chang* [1980] and *Wentz* [1983] indicate that the optical limit is reached near ν = 37 GHz. Hence, for $\nu \geq 37$ GHz, we use the *Cox and Munk* [1954] expression for optical slope variance. For lower frequencies, a reduction factor is applied to the Cox and Munk expression. This reduction factor is based on ΔS^2 values derived from the SeaSat SMMR observations [*Wentz*, 1983].

$$\Delta\mathrm{S}^2 = 5.22\times10^{-3}\,\mathrm{W} \qquad \nu \geq 37\ \mathrm{GHz} \tag{56a}$$

$$\Delta\mathrm{S}^2 = 5.22\times10^{-3}\left[1-0.00748(37-\nu)^{1.3}\right]\mathrm{W} \qquad \nu < 37\ \mathrm{GHz} \tag{56b}$$

where W is the wind speed (m/s) measured 10 m above the surface. Note the Cox and Munk wind speed was measured at a 12.5 m elevation. Hence, their coefficient of 5.12×10^{-3} is increased by 2% to account for our wind being referenced to a 10 m elevation.

The sea-surface reflectivity R_{geo} is computed for a range of winds varying from 0 to 20 m/s, for a range of sea-surface temperatures varying from 273 to 303 K, and for a range of incidence angles varying from 49° to 57°. These computations require the numerical evaluation of the integral in equation (53). The integration is done over the range $\mathrm{S}_\mathrm{u}^2+\mathrm{S}_\mathrm{c}^2 \leq 4.5\Delta\mathrm{S}^2$. Facets with slopes exceeding this range contribute little to the integral, and it is not clear if a Gaussian slope distribution is even applicable for such large slopes. Analysis shows that the computed ensemble of R_{geo} is well approximated by the following regression:

$$R_{geo} = R_0 - [r_0 + r_1\theta_i - 53 + r_2 T_S - 288 + r_3\theta_i - 53 T_S - 288]W \qquad (57)$$

where the first term R_0 is the specular power reflectivity given by (46) and the second term is the wind-induced component of the sea-surface reflectivity. The r coefficients are given in Table 7 for all AMSR channels. Equation (57) is valid over the incidence angle from 49° to 57°. It approximates the θ_i and T_S variation of R_{geo} with an equivalent accuracy of 0.1 K. The approximation error in the wind dependence is larger. In the geometric optics computations, the variation of R_{geo} with wind is not exactly linear. In terms of T_B, the non-linear component of R_{geo} is about 0.1 K at the lower frequencies and 0.5 K at the higher frequencies. However, in view of the general uncertainty in the geometric optics model, we will use the simple linear expression for R_{geo}, and let the empirical F term account for any residual non-linear wind variations, as is discussed in the next paragraph.

In the case of the coefficients r_2 we do not use the geometric optics model coefficients (Table 7) but rather use the following empirically derived forms (units are s/m-K):

$$r_{2_{V-pol}} = -2.1 \cdot 10^{-5} \qquad (58)$$

$$r_{2_{h-pol}} = -5.5 \cdot 10^{-5} + 0.989 \cdot 10^{-6} \cdot 37 - v \qquad \text{if} \quad n \le 37 \qquad (59a)$$

$$r_{2_{h-pol}} = -5.5 \cdot 10^{-5} \qquad \text{if} \quad n > 37. \qquad (59b)$$

This accounts for the observations that the wind induced emissivity is less in warm water. This effect was observed during the monsoons in the Arabian sea.

Table 7. Model Coefficients for Geometric Optics

Freq. (GHz)	6.93E+0	10.65E+0	18.70E+0	23.80E+0	36.50E+0	50.30E+0	52.80E+0	89.00E+0
v-pol r_0	–0.27E–03	–0.32E–03	–0.49E–03	–0.63E–03	–1.01E–03	–1.20E–03	–1.23E–03	–1.53E–03
h-pol r_0	0.54E–03	0.72E–03	1.13E–03	1.39E–03	1.91E–03	1.97E–03	1.97E–03	2.02E–03
v-pol r_1	–0.21E–04	–0.29E–04	–0.53E–04	–0.70E–04	–1.05E–04	–1.12E–04	–1.13E–04	–1.16E–04
h-pol r_1	0.32E–04	0.44E–04	0.70E–04	0.85E–04	1.12E–04	1.18E–04	1.19E–04	1.30E–04
v-pol r_2	0.01E–05	0.11E–05	0.48E–05	0.75E–05	1.27E–05	1.39E–05	1.40E–05	1.15E–05
h-pol r_2	0.00E–05	–0.03E–05	–0.15E–05	–0.23E–05	–0.36E–05	–0.32E–05	–0.30E–05	0.00E–05
v-pol r_3	0.00E–06	0.08E–06	0.31E–06	0.41E–06	0.45E–06	0.35E–06	0.32E–06	–0.09E–06
h-pol r_3	0.00E–06	–0.02E–06	–0.12E–06	–0.20E–06	–0.36E–06	–0.43E–06	–0.44E–06	–0.46E–06
r_0 in units of s/m, r_1 in units of s/m-deg, r_2 in units of s/m-K, r_3 in units of s/m-deg-K								

In the 10-37 GHz band, the F term is found from collocated SSM/I-buoy and TMI-buoy observations. The procedure for finding F is essentially the same as described by *Wentz* [1997] for finding the wind-induced emissivity, but in this case we first remove the geometric optics contribution to R. The F term is found to be a monotonic function of wind speed described by

$$F = m_1 W \qquad W < W_1 \qquad (60a)$$

$$F = m_1 W + \tfrac{1}{2}(m_2 - m_1)(W - W_1)^2 / (W_2 - W_1) \qquad W_1 \le W \le W_2 \qquad (60b)$$

$$F = m_2 W - \tfrac{1}{2}(m_2 - m_1)(W_2 + W_1) \qquad W > W_2 \qquad (60c)$$

This equation represents two linear segments connected by a quadratic spline such that the function and its first derivative are continuous. The spline points are $W_1 = 3\,m/s$ and $W_2 = 12\,m/s$ for the v-pol and $W_1 = 7\,m/s$ and $W_2 = 12\,m/s$ for the h-pol , respectively. The m coefficients are found so that the T_B model matches the SSM/I observations in the and TMI observations when the buoy wind is used to specify W. For the lowest channel $n = 6.9\,GHz$ no data exist yet and we have simply used the same values as for the $n = 10.65\,GHz$ channel. This will be updated as soon as AMSR data become available. Table 8 summarizes the results for m_1 and m_2 at the 8 AMSR frequencies for v and h polarizations. Both coefficients flatten out and reach a maximum for $n \ge 37$ GHz.

Table 8. The coefficients m_1 and m_2. Units are s/m.

Freq. (GHz)	6.93	10.65	18.70	23.80	36.50	50.30	52.80	89.00
v-pol m_1	0.00020	0.00020	0.00140	0.00178	0.00257	0.00260	0.00260	0.00260
h-pol m_1	0.00200	0.00200	0.00293	0.00308	0.00329	0.00330	0.00330	0.00330
v-pol m_2	0.00690	0.00690	0.00736	0.00730	0.00701	0.00700	0.00700	0.00700
h-pol m_2	0.00600	0.00600	0.00656	0.00660	0.00660	0.00660	0.00660	0.00660

These results indicate that diffraction plays a significant role in modifying the sea-surface reflectivity. If diffraction were not important, β would be 0 in equation (50), and F would be proportional to the fractional foam coverage f. Since f is essentially zero for W < 7 m/s, m_1 would be 0. This is not the case, and we interpret the m_1 coefficient as an indicator of diffraction.

2.6. Atmospheric Radiation Scattered by the Sea Surface

The downwelling atmospheric radiation incident on the rough sea surface is scattered in all directions. The scattering process is governed by the radar cross section coefficients σ_o as indicated by equation (14). For a perfectly flat sea surface, the scattering process reduces to simple specular reflection, for which radiation coming from the zenith angle θ_s is reflected into zenith angle θ_i , where $\theta_s = \theta_i$. In this case, the reflected sky radiation is simply RT_{BD}. However, for a rough sea surface, the tilted surface facets reflect radiation for other parts of the sky into the direction of zenith angle θ_i. Because the downwelling radiation T_{BD} increases as the secant of the zenith angle, the total radiation scattered from the sea surface is greater than that given by simple specular reflection. The sea-surface reflectivity model discussed in the previous section is used to compute the scattered sky radiation $T_{B\Omega}$. These computations show that $T_{B\Omega}$ can be approximated by

$$T_{B\Omega} = [(1+\Omega)(1-\tau)(T_D - T_C) + T_C]\ R \tag{61}$$

where R is the sea-surface reflectivity given by (49), T_{BD} is the downwelling brightness temperature from zenith angle θ_i given by (24), and Ω is the fit parameter. The second term in the brackets is the isotropic component of the cold space radiation. This constant factor can be removed from the integral. The fit parameter for v-pol and h-pol is found to be

$$\Omega_V = [2.5 + 0.018(37-\nu)\ ][\Delta S^2 - 70.0\Delta S^6]\ \tau^{3.4} \tag{62a}$$

$$\Omega_H = [6.2 - 0.001(37-\nu)^2\ ][\Delta S^2 - 70.0\Delta S^6]\ \tau^{2.0} \tag{62b}$$

where ν is frequency (GHz) and ΔS^2 is the effective slope variance given by (56). The term $\Delta S^2 - 70.0\Delta S^6$ reaches a maximum at $\Delta S^2 = 0.069$. For $\Delta S^2 > 0.069$, the term is held at its maximum value of 0.046. Ω_V has a linear dependence on frequency, whereas Ω_H has a quadratic dependence, reaching a maximum value at $\nu = 37$ GHz. For $\nu > 37$ GHz, both Ω_V and Ω_H are held constant at their maximum values. Approximation (62) is valid for the range of incidence angles from 52° to 56°. For moderately high winds (12 m/s) and a moist atmosphere (high vapor and/or heavy clouds), the scattering process increases the reflected 37 GHz radiation by about 1 K for v-pol and 5 K for h-pol. At 7 GHz, the increase is much less, being about 0.2 K for v-pol and 0.8 K for h-pol. The accuracy of the above approximation as compared to the theoretical computation is about 0.03 K and 0.2 K at 7 and 37 GHz, respectively. Note that when the atmospheric absorption becomes very large (i.e., τ is small), Ω tends to zero because the sky radiation for a completely opaque atmosphere is isotropic.

2.7. Wind Direction Effects

The anisotropy of the sea-surface roughness produces a variation of the brightness temperature versus wind direction, as discussed in Section 2.5. In the 19 to 37 GHz band, *Wentz* [1992] determined this wind direction signal using collocated SSM/I T_B's and buoy wind vectors. At an incidence angle near 53°, the wind direction signal exhibits the following second-order harmonic variation with wind direction:

$$\Delta E_{19-37} = \gamma_1 \cos\phi + \gamma_2 \cos 2\phi \tag{63}$$

where ΔE is the change in the sea-surface emissivity and ϕ is the wind-direction angle relative to the azimuth-look angle. When $\phi = 0°$ (180°), the observation is upwind (downwind). The subscript 19-37 denotes that the results are for the 19-37 GHz band. The amplitude coefficients γ_1 and γ_2 are found to be essentially the same for both 19 and 37 GHz. The coefficients are different for the two polarizations and do vary with wind speed as given below

$$\gamma_{1V} = \ \ 7.83\times10^{-4}W - 2.18\times10^{-5}W^2 \tag{64a}$$

$$\gamma_{2V} = -4.46\times10^{-4}W + 3.00\times10^{-5}W^2 \tag{64b}$$

$$\gamma_{1H} = \quad 1.20\times10^{-3}\,W - 8.57\times10^{-5}\,W^2 \tag{65a}$$

$$\gamma_{2H} = -8.93\times10^{-4}\,W + 3.76\times10^{-5}\,W^2 \tag{65b}$$

In *Wentz* [1992], the wind direction signal was expressed in terms of a brightness temperature change rather than an emissivity change, and the wind speed was referenced to a 19.5 m anemometer height. In the above equations, we have converted the *Wentz* [1992] expressions from ΔT_B to ΔE and use a 10 m reference height for W.

Little is known about the wind direction signal for frequencies below 19 GHz. Some very preliminary data from the Japanese AMSR aircraft simulations suggests that the signal decreases with decreasing frequency. Other than this, there are no experimental data on the variation of T_B versus ϕ at 6.9 and 10.7 GHz. As an educated guess on what will be observed at these lower frequencies we reduce the wind direction signal from its value at 19 GHz by a factor of 0.82 at 10.7 GHz and by a factor of 0.62 at 6.9 GHz.

The result for the wind direction signal from (64) and (65) should be regarded as preliminary. Recent aircraft data *Yueh et al.* [1999] as well as a first analysis of TMI measurements suggest that at wind speeds below 8 m/s the wind direction signal is noticeably smaller than the one obtained from (64) and (65), especially for the h-pol. A reanalysis of the directional signal using data from 5 SSM/I satellites between 1987 and 1999 as well as recent TMI data is currently under way.

3. The Ocean Retrieval Algorithm

3.1 Introduction

In general, there are three types of ocean retrieval algorithms:

1. Multiple linear regression algorithms
2. Non-linear, iterative algorithms
3. Post-launch *in-situ* regression algorithms

The first two types are physical algorithms in the sense that radiative transfer theory is used in their derivation. The third type is purely statistical with little or no consideration of the underlying physics. We now describe each of these algorithms and discuss their strengths and weaknesses.

3.2 Multiple Linear Regression Algorithm

Consider a linear process in which a set of inputs denoted by the column vector **X** is transformed to a set of outputs denoted by the column vector **Y**. The linear process is then characterized by the matrix **A** that relates **Y** to **X**.

$$\mathbf{Y} = \mathbf{AX} \tag{66}$$

The measurement of Y usually contains some noise **e** and is denoted by

$$\tilde{\mathbf{Y}} = \mathbf{Y} + \mathrm{e} = \mathbf{AX} + \mathrm{e} \tag{67}$$

The retrieval problem is then to estimate **X** given $\tilde{\mathbf{Y}}$. The most commonly used criteria for estimating **X** is to find **X** such that the variance between **Y** and $\tilde{\mathbf{Y}}$ is minimized. Using this criteria, one finds the well known least-squares solution:

$$\hat{\mathbf{X}} = (\mathbf{A}^{\mathbf{T}}\Xi^{-1}\mathbf{A})^{-\mathbf{1}}\mathbf{A}^{\mathbf{T}}\Xi^{-1}\tilde{\mathbf{Y}} \tag{68}$$

where **X** is the correlation matrix for the error vector **e**. If the errors are uncorrelated, then **X** is diagonal.

For our application, the system input vector **X** is the set of geophysical parameters **P** and the output vector $\tilde{\mathbf{Y}}$ is the set of T_B measurements. Note that X and Y can be non-linear functions of P and T_B, respectively without violating the requirement for linearity between **X** and **Y**. For example, the relationship between T_B and atmospheric parameters V and L can be approximated by

$$T_B \approx T_E\{1 - R\ \exp[-2\sec\boldsymbol{q}_i(A_O + a_V V + a_L L)]\} \tag{69}$$

where T_E is an effective temperature of the ocean-atmosphere system which is relatively constant. Then,

$$\ln(T_E - T_B) = \ln(RT_E) - 2\sec\boldsymbol{q}_i(A_O + a_V V + a_L L) \tag{70}$$

From this we see that the relationship between T_B and V, L can be linearized by transforming from **Y** = T_B to **Y** = $\ln(T_E - T_B)$. *Wilheit and Chang* [1980] followed this approach and used a value of 280 K for T_E. As a further extension, **Y** can also include higher order terms such as T_B^2 and $T_{B37V}\,T_{B23H}$.

Likewise, the input X can be a nonlinear transformation of the geophysical parameters P. For example, the wind speed dependence of T_B (i.e., $\partial T_B/\partial W$) increases with wind speed, and the relationship can be made linear by the following transformation

$$W' = W \qquad W < W_1 \tag{71a}$$
$$W' = W + M_1 (W - W_1)^2 \qquad W_1 \le W \le W_2 \tag{71b}$$
$$W' = M_2 W - M_3 \qquad W > W_2 \tag{71c}$$

This transformation represents two linear segments connected by a quadratic spline such that the function and its first derivative are continuous.

Thus the requirement of linearity is not as constraining as it might first appear, and a generalized linear statistical regression algorithm can be represented by

$$P_j = \Re\left[c_{0j} + \sum_{i=1}^{I} c_{ij} \Im(T_{Bi}) \right] \tag{72}$$

where $\Im$ and $\Re$ are linearizing functions. Subscript i denotes the AMSR channel (1 = 6.9V, 2 = 6.9H, etc.), and subscript j denotes the parameter to be retrieved (1 = T_S, 2 = W, 3 = V, 4 = L). For AMSR, our initial design for the linear regression algorithm discussed in the next section uses the following linearizing functions:

$$\Im(T_B) = T_B \qquad \nu = 6.9 \text{ and } 10.7 \text{ GHz} \tag{73a}$$
$$\Im(T_B) = -\ln(290 - T_B) \qquad \nu = 18.7,\ 23.8, \text{ and } 36.5 \text{ GHz} \tag{73b}$$
$$\Re(X) = X \tag{74}$$

After testing the initial algorithm, we will experiment with additional linearizing functions, such as the wind speed linearization given by (71).

In principle, the c_{ij} coefficients can be found from (68) given the **A** matrix and the error correlation matrix $\mathbf{X}$. However, even after the linearizing functions are applied, the relationship of **Y** versus **X** is not strictly linear, and the elements of **A** matrix are not constant, but rather vary with **P**. One could find a linear approximation for the **Y** versus **X** relationship, and then derive the c_{ij} coefficients from (68). However, we prefer the more direct approach suggested by *Wilheit and Chang* [1980] in which brightness temperatures are computed for an ensemble of environmental scenes and then multiple linear regression is used to derive the c_{ij} coefficients, as is discussed in the following section.

3.3. Derivation and Testing of the Linear Regression Algorithm

The derivation of the c_{ij} coefficients in the AMSR linear regression algorithm is shown in Figure 5. A large ensemble of ocean-atmosphere scenes are first assembled. The specification of the atmospheres comes from 42,195 quality-controlled radiosonde flights launched from small islands during the 1987 to 1990 time period [*Wentz*, 1997]. One half of these radiosonde flights are used for deriving the c_{ij} coefficients, and the other half is withheld for testing the algorithm. A cloud layer of various columnar water densities ranging from 0 to 0.3 mm is superimposed on the radiosonde profiles. Underneath these simulated atmospheres, we place a rough ocean surface. The sea-surface temperature T_S is randomly varied from 0 to 30 C, the wind speed W is randomly varied from 0 to 20 m/s, and the wind direction ϕ is randomly varied from 0 to 360°. About 400,000 scenes are generated in this manner.

In nature, there is a strong correlation between T_S and W. We could have incorporated this correlation into the ensemble of the scene. For example, we could have discarded cases of very cold water and very high water vapor, which never occur in nature. However, for now we include these unrealistic cases in order to determine if the algorithm is

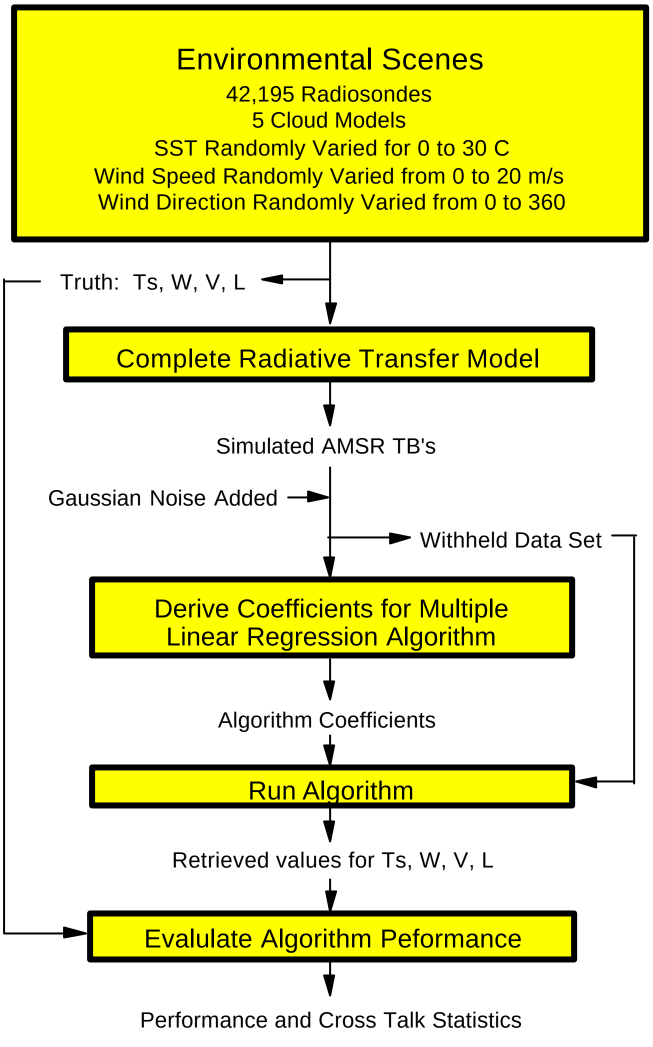

Fig. 5. Derivation and testing of the linear regression algorithm

truly capable of separating the T_S signal from the V signal.

Atmospheric brightness temperatures T_{BU} and T_{BD} and transmittance τ are computed from the radiosonde + cloud profiles of T(h), p(h), ρ_V(h), and ρ_L(h) using equations (17), (18) and (19). The reflectivity R of the rough sea surface is computed according to the equations given in Section 2.5, and the atmospheric radiation scattered from the sea surface $T_{B\Omega}$ is computed from (61). Wind direction effects are included as described in Section 2.7. Finally, the brightness temperature T_B as seen by AMSR is found by combining the atmospheric and sea-surface components, as is expressed by (10).

Noise is added to the simulated AMSR T_B's. This noise represents the measurement error in the AMSR T_B's. The measurement error depends on the spatial resolution. At a 60-km resolution, which is commensurate with the 6.9 GHz footprint, the measurement error is 0.1 K. A random number generator is used to produce Gaussian noise having a standard deviation of 0.1 K. This noise is added to the simulated T_B's. At this point in the simulation, we could also add modeling error to the T_B's. Modeling error accounts for the difference between the model and nature. It is a very difficult parameter to determine since it involves physical processes which are not sufficiently understood to be included in the current model. For now, we are not including any modeling error in the simulations, but we will be investigating this problem in the future.

Given the noise-added simulated T_B's, the standard multiple linear regression technique is used to find the c_{ij} coefficients. The coefficients are found such that the rms difference between P_j and the true value for the specified environmental scene is minimized. For the initial set of simulations, we use all 10 lower frequency channels (i.e., 6.9, 10.7, 18.7, 23.8 and 36.5 GHz, dual polarization). Later on, we will investigate the utility of using a reduced set of channels.

The algorithm is tested by repeating the above process, only this time using the withheld environmental scenes. The geophysical parameters T_S, W, V, and L are computed from the noise-added T_B's using equation (72). Statistics on the error in P_i are accumulated. The results are shown in Figure 6. The solid line in the figure shows the mean retrieval error, and the dashed lines show the one standard deviation envelope. The retrieval error for each of the four parameters is plotted versus the four parameters in order to show the crosstalk error matrix. The diagonal in the crosstalk matrix verifies that the dynamic range of a given parameter is correct, and the off-diagonal plots verify that there is no crosstalk error in the retrieval.

The results look quite good. There is a little crosstalk, but it is quite small. Table 9 gives the overall rms error for the retrievals. Wind direction variability is a major source of error in the T_S retrieval. When wind direction variability is removed from the simulations, the T_S retrieval error decreases to 0.3 C. The wind direction problem is further discussed in Sections 1.5 and 4.3.

We again emphasize that these results are very preliminary. There is much more work to do. For example, the cloud models need to be more variable and the performance of the relatively simple LSR algorithm needs to be compared with the non-linear algorithm discussed in the next section.

Table 9. Preliminary Estimate of Retrieval Error

Ocean Parameter	Rms Error
Sea-Surface Temperature	0.58 C
Wind Speed	0.86 m/s
Columnar Water Vapor	0.57 mm
Columnar Cloud Water	0.017 mm

3.4. Non-Linear, Iterative Algorithm

The major shortcoming of the multiple linear regression algorithm is that the non-linearities in the T_B versus **P** relationship are handled in an *ad hoc* manner. The linearization functions are only approximations, and the inclusion of second order terms such as T_B^2 and $T_{B37V}\,T_{B23H}$ do not really describe the inverse of the T_B versus **P** relationship. A more rigorous treatment of the non-linearity problem is to express the T_B versus **P** relationship in terms of a non-linear model function F(**P**), and then invert the following set of equations

$$T_{Bi} = F_i(\mathbf{P}) + \varepsilon_i \qquad (75)$$

where subscript i denotes the observation number and ε_i is the measurement noise. The number of observations must be equal to or greater than the number of unknown parameters (i.e., the number of elements in **P)**. For each set of AMSR observations, equations (75) are inverted to yield **P**. This method is much more numerically intensive than the linear regression algorithm in which there is a fixed relationship between **P** and T_B. However, given today's computers, the computational burden is no longer a problem.

Equation (75) is solved using an extension of Newton's iterative method. In Newton's method, the model function is expressed as a Taylor expansion:

$$T_{Bi} = F_i(\overline{\mathbf{P}}) + \sum_{j=1}^{4} \left(P_j - \overline{P}_j\right) \frac{\partial F_i}{\partial P_j}\bigg|_{\overline{\mathbf{P}}} + O^2 + \boldsymbol{\varepsilon}_i \tag{76}$$

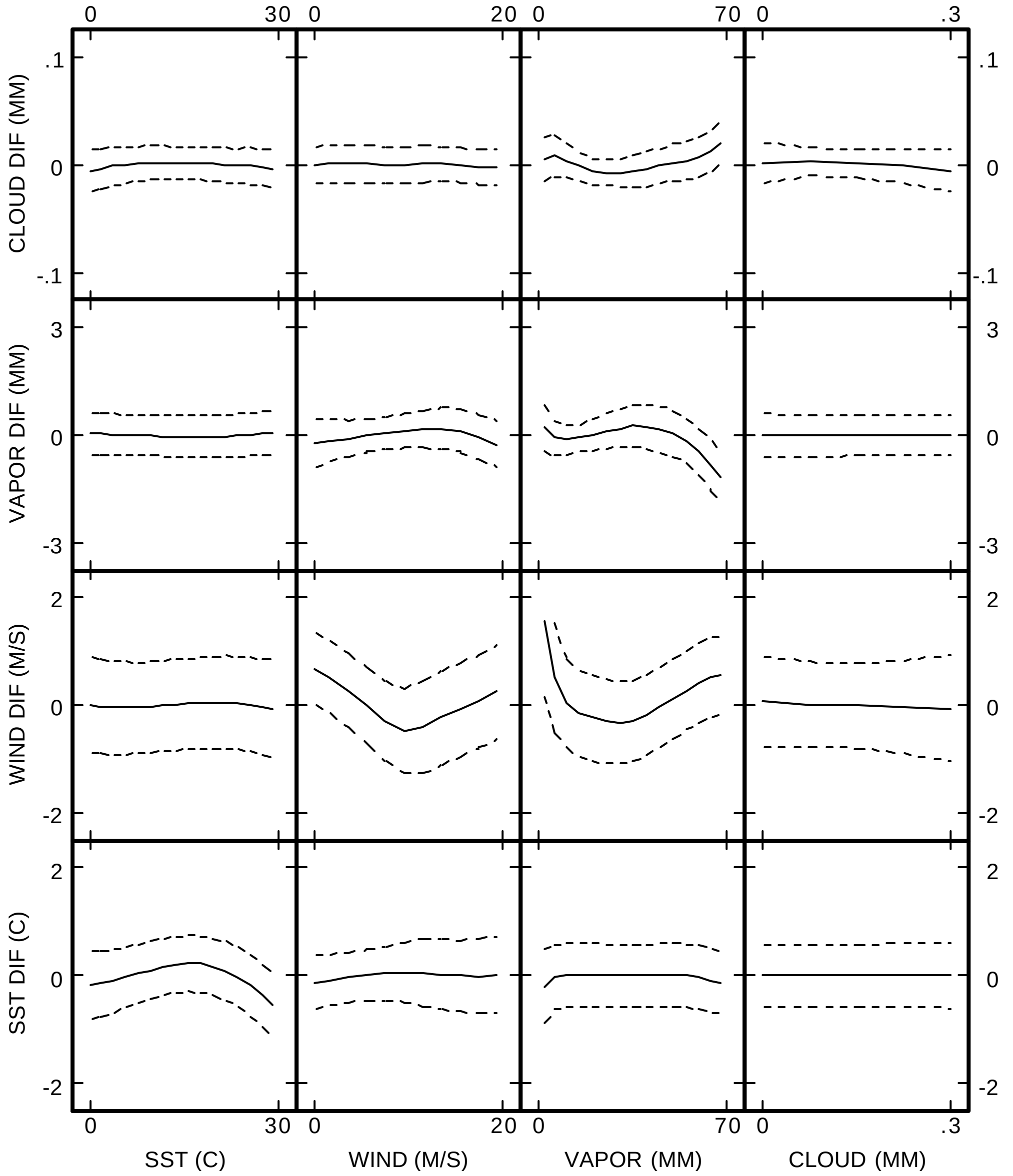

Fig 6. Preliminary results for the linear statistical regression algorithm for AMSR. The solid line in the figure shows the mean retrieval error, and the dashed lines show the one standard deviation envelope. The retrieval error for each of the four parameters is plotted versus the four parameters in order to show the crosstalk error matrix. The diagonal in the crosstalk matrix verifies that the dynamic range of a given parameter is correct, and the off-diagonal plots verifies that there is no crosstalk error in the retrieval.

where $\overline{\mathbf{P}}$ is a first guess value for **P** and O^2 represents the higher order terms in the expansion. This system of simultaneous equations is written in matrix form as

$$\Delta\mathbf{T_B} = \mathrm{A}\ \Delta\mathbf{P} + \mathbf{O}^2 + \mathrm{e} \tag{77}$$

where **A** is a matrix of $i \times j$ elements and $\Delta\mathbf{T_B}$, $\Delta\mathbf{P}$, and $\boldsymbol{\varepsilon}$ are column vectors. The elements of **A,** $\Delta\mathbf{T_B}$, and $\Delta\mathbf{P}$ are

$$A_{ij} = \left.\frac{\partial F_i}{\partial P_j}\right|_{\overline{\mathbf{P}}} \tag{78}$$

$$\Delta \mathrm{T}_{\mathrm{B}i} = \mathrm{T}_{\mathrm{B}i} - \mathrm{F}_i(\overline{\mathbf{P}}) \tag{79}$$

$$\Delta \mathrm{P}_j = \mathrm{P}_j - \overline{\mathrm{P}}_j \tag{80}$$

Equation (77) is solved by ignoring the higher order terms (i.e., by setting O^2 to zero), and the solution is

$$\mathbf{P} = \overline{\mathbf{P}} + (\mathbf{A}^{\mathbf{T}}\Xi^{-1}\mathbf{A})^{-1}\mathbf{A}^{\mathbf{T}}\Xi^{-1}\Delta\mathbf{T_B} \tag{81}$$

where Ξ is the error correlation matrix. This procedure is then repeated with **P** from (81) replacing $\overline{\mathbf{P}}$, and several such iterations are performed. For the no-noise case ($\boldsymbol{\varepsilon} = 0$), Ξ drops out of the formulation and an exact solution is obtained when $\Delta\mathbf{T_B}$ goes to zero. For the noise case, a solution is found when $\Delta\mathbf{T_B}$ reaches some constant minimum value.

The solution of P can be constrained by the inclusion of *a priori* information. This is accomplished by including additional equations in (77). For example, if ancillary information on wind direction were available, then the following equation could be added to (77)

$$\phi = \bar{\bar{\phi}} + \varepsilon_\phi \tag{82}$$

where $\bar{\bar{\phi}}$ is the a priori estimate of ϕ and ε_ϕ is the rms uncertainty in that estimate. Similar constraining equations can be included for other types of information such as the vertical distribution of water vapor and air temperature.

In general, there is no guarantee that a solution will be found using this method. Furthermore, if a solution is found, there is no guarantee that it is an unique solution. However for the case of AMSR, the relationships between **P** and T_B are quasi-linear in that $\partial T_B/\partial P > 0$ for all channels except 36.5 GHz in cold water, for which $\partial T_B/\partial T_S$ is < 0. Experience has shown that a solution is nearly always found. It also appears that this solution is unique, but this needs to be verified.

We have been assuming that the T_B versus **P** relationship can be exactly described by a non-linear model function F. In this case, the non-linear, iterative algorithm has the distinct advantage of finding the exact solution. In comparison, the **P** found by the linear regression algorithm would be in error by some degree due to the nonlinearities. However, in practice it is not possible to exactly represent the T_B versus **P** relationship in terms a model function F(**P**). For example, the T_B not only depends on the columnar content of water vapor but also on vertical distribution of the vapor. Thus, some approximations need to be made when going from the integral equations of radiative transfer to a simplified model function F(**P**). These assumptions were discussed in length in Section 2. In the derivation of the linear regression algorithm, the complete integral formulation of the radiative transfer theory is used, and there is no need for the simplifying assumptions.

In comparing the two types of algorithms, there is a tradeoff between errors due to non-linearities in the linear regression algorithm and errors due to simplifying assumptions in the non-linear, iterative algorithm. Our plan is to develop and test both types of algorithms in parallel, compare their relative performance, and then select one or the other.

3.5. Post-Launch *In-Situ* Regression Algorithm

After AMSR is launched, purely statistical algorithms can be developed by collocating the AMSR T_B's with selected *in-situ* sites. A simple least-squares regression is then found that relates the *in situ* parameter to the T_B's. The mathematical form of this type of algorithm is identical to the linear regression algorithm given by (72). The difference is that the c_{ij} coefficients are not derived from radiative transfer theory, but rather from the regression to the *in situ* data. Examples of this type of algorithm are the *Goodberlet et al.* [1989] SSM/I wind algorithm and the *Alishouse et al.* [1990] SSM/I water vapor algorithm.

The strength of the purely statistical algorithm is that it does not require a radiative transfer model, and hence it is not affected by modeling errors. The weaknesses are:

1. The algorithm for AMSR cannot be developed until after launch.
2. Large *in situ* data sets covering the full range of global conditions must be assembled and collocated with the AMSR observations.

3. The purely statistical algorithm is keyed to specific sensor parameters such as frequency and incidence angle. For example, none of the algorithms developed for SSM/I can be applied to AMSR. In contrast, SSM/I algorithms based on radiative transfer theory can be interpolated to the new AMSR frequencies and incidence angle.

4. Cross-talk among the various geophysical parameters is a problem for the statistical algorithm. For example, consider sea-surface temperature T_S and water vapor V which are highly correlated on a global scale. A purely statistical algorithm will mimic this correlation and will generate a T_S product that is always highly correlated with V. In nature, when the true V changes and T_S remains constant (i.e., a weather system passing by), the statistical algorithm will erroneously report a change in T_S.

5. For the case of cloud water retrieval, for which there is no reliable *in situ* data, this type of algorithm cannot be used.

We think it is a mistake to ignore the physics when developing an algorithm. It may be the case that relatively simple regressions can be used to retrieve some of the parameters. However, it is important that these regressions be understood in the context of radiative transfer theory. Thus, after AMSR is launched and the collocated *in situ* data are available, we will calibrate the pre-launch algorithm by making small adjustments to the radiative transfer model rather than developing purely statistical algorithms. This calibration activity is discussed in the Section 5.

3.6. Incidence Angle Variations

The retrieval of sea-surface temperature and wind speed are sensitive to incidence angle variations. A 1° error in specifying θ_i produces a 6 C error in T_S and a 5 m/s error in W. Thus, it is crucial that the incidence angle be accurately known and that the retrieval algorithm accounts for incidence angle variations.

The pointing knowledge for the PM platform is specified to be 0.03°/axis. This figure is the 3-standard deviation error in the knowledge of the roll, pitch, and yaw. Yaw variations do not affect the incidence angle, but roll and pitch do. The corresponding 3-standard deviation error in incidence angle is approximately 0.05°. The retrieval accuracy for the geophysical parameters are in terms of a 1-standard deviation error, so we convert the incidence angle error to a 1-standard deviation error of 0.016°, and this results in a 0.1 C error in the T_S retrieval and a 0.1 m/s error in the W retrieval. The specification of pointing knowledge for the PM platform is, therefore, sufficient. However, the pointing knowledge of the AMSR instrument is yet to be specified. We will be paying close attention to this instrument specification.

In the non-linear, iterative algorithm, incidence angle is an explicit parameter in the model function, and hence θ_i variations are easily handled by simply assigning a value to θ_i before doing the inversion process. There are two possible methods for handling incidence angle variation in the linear regression algorithm. First, include incidence angle as an additional term in the regression or second, normalize the T_B's to some constant incidence angle, say 55°, before applying the regression. This normalization is expressed by

$$T_B\left(55^\circ\right) = T_B\left(\theta_i\right) + \mu \cdot \theta_i - 55^\circ \qquad (83)$$

where μ represents the derivative $\partial T_B/\partial\theta_i$, which depends on the T_S, W, V, and L. We find that μ can be accurately approximated by a T_B regression of the type given by (73). This method works well when the incidence angle variations are ± 1° or less, which should be the case for AMSR.

6. References

Alishouse, J.C., S. Synder, J. Vongsathorn, and R.R. Ferraro, Determination of oceanic total precipitable water from the SSM/I, *IEEE Trans. Geoscience and Remote Sensing, 28,* 811-816, 1990.

Archer, D.G., and P. Wang, The dielectric constant of water and debye-huckel limiting law slopes, *J. Phys. Chem. Ref. Data, 19,* 371, 1990.

Becker, G.E., and S.H. Autler, Water vapor absorption of electromagnetic radiation in the centimeter wave-length range, *Phys. Rev*., *70*(5/6), 303-307, 1946.

Cole, K.S., and R.H. Cole, Dispersion and absorption in dielectrics, *J. Chemical Physics, 9,* 341-351, 1941.

Cox, C.S., Measurements of slopes of high-frequency wind waves, *J. Mar. Res*., *16*, 199-225, 1958.

Cox, C.S., and W.H. Munk, Measurement of the roughness of the sea surface from photographs of the sun's glitter, *J. Opt. Soc. Am., 44,* 838-850, 1954.

Debye, R., *Polar Molecules,* Chemical Catalog, New York, 1929.

Goldstein, H., Attenuation by condensed water, *Propagation of Short Radio Waves, MIT Rad. Lab. Ser., 13,* McGraw-Hill, New York: 1951.

Goodberlet, M.A., C.T. Swift, and J.C. Wilkerson, Remote sensing of ocean surface winds with the SSM/I, *J. Geophys. Res., 94*, 14547-14555, 1989.

Grant, E., T. Buchanan, and H. Cook, Dielectric behavior of water at microwave frequencies, *J. Chem. Phys*., *26*, 156-161, 1957.

Haggis, G.H., J.B. Hasted, T.J. Buchanan, The dielectric properties of water in solutions, *J. Chem. Phys.*, *20*, 1452-1465, 1952.

Hasted, J.B., and S. El Sabeh, The dielectric properties of water in solutions, *Trans. Faraday Soc.*, *49*, 1003-1011, 1953.

Hasted, J.B., and G. Roderick, Dielectric properties of aqueous and alcoholic electrolytic solutions, *J. Chem. Phys.*, *29*, 17-26, 1958.

Ho, W., and W. F. Hall, Measurements of the dielectric properties of sea water and NaCl solutions at 2.65 GHz, *J. Geophys. Res.*, *78*, 6301-6315, 1973.

Ho, W.W., A.W. Love, and M. J. Van Melle, Measurements of the dielectric properties of sea water at 1.43 GHz, *NASA Contractor Report CR-2458*, 1974.

Jones, W.L., P.G. Black, D.M. Boggs, E.M. Bracalente, R.A. Brown,, G. Dome, J.A. Ernst, I.M. Halberstam, J.E. Overland, S. Peteherych, W.J. Pierson, F.J. Wentz, P.M. Woiceshyn, and M.G. Wurtele, Seasat scatterometer: Results of the Gulf of Alaska workshop, *Science*, *204*, 1413-1415, 1979.

Keller, W.C., and J.W. Wright, Microwave scattering and the straining of wind-generated waves, *Radio Sci.*, *10*, 139-147, 1975.

Klein, L.A., and C.T. Swift, An improved model for the dielectric constant of sea water at microwave frequencies, *IEEE J. Oceanic Eng.*, *OE-2*, 104-111, 1977.

Lane, J.A., and J.A. Saxton, Dielectric dispersion in pure polar liquids at very high frequencies, III. The effect of electrolytes in solution, Proc. Roy. Soc., A213, 531-545, 1952.

Lide, D.R, *Handbook of Chemistry and Physics, 74th Edition*, CRC Press, Ann Arbor, p. 6-10, 1993.

Liebe, H.J., An updated model for millimeter wave propagation in moist air, *Radio Sci.*, *20*, 1069-1089, 1985.

Malmberg, C., and A. Maryott, Dielectric constant of water from 0° to 100°C, *J. Res. Nat. Bureau of Standards*, *56*, 1-8, 1956.

Marshall, T.S., and W.McK. Palmer, The distribution of raindrops with size, *J. Meteor.*, *5*, 165-166, 1948.

Mitsuyasu, H., and T. Honda, Wind-induced growth of water waves, *J. Fluid Mech.*, *123*, 425-442, 1982.

Monahan, E.C., and I. O'Muircheartaigh, Optimal power-law description of oceanic whitecap coverage dependence on wind speed, *J. Phys. Oceanogr.*, *10*, 2094-2099, 1980.

Peake, W.H., Interaction of electromagnetic waves with some natural surfaces, *IEEE Trans. Antennas Propagat.*, *AP-7*, S324-S329, 1959.

Reif, F., *Fundamentals of Statistical and Thermal Physics*, McGraw-Hill, Inc., San Francisco, p. 381-388, 1965.

Rice, S.O., Reflection of electromagnetic waves from slightly rough surfaces, *Commun. Pure Appl. Math*, *4*, 351-378, 1951.

Rosenkranz, P.W., Shape of the 5 mm oxygen band in the atmosphere, *IEEE Tran. Antennas Propag.*, *AP-23*(4), 498-506, 1975.

Smith, P.M., The emissivity of sea foam at 19 and 37 GHz, *IEEE Trans. Geosci. Remote Sensing*, *GE-26*, 541-547, 1988.

Stogryn, A., The apparent temperature of the sea at microwave frequencies, *IEEE Trans. Antennas Propagat.*, *AP-15*, 278-286, 1967.

Stogryn, A., Equations for calculating the dielectric constant of saline water, *IEEE Trans. Microwave Theory Tech.*, *MTT-19*, 733-736, 1971.

Stogryn, A., The emissivity of sea foam at microwave frequencies, *J. Geophys. Res.*, *77*, 1650-1666, 1972.

Waters, J.R., Absorption and emission by atmospheric gases, *in Methods of Experimental Physics*, vol. 12B, edited by M.L. Meeks, chap. 2.3, Academic, Orlando, Fla., 1976.

Wentz, F.J., A two-scale scattering model for foam-free sea microwave brightness temperatures, *J. Geophys. Res.*, *80*, 3441-3446, 1975.

Wentz, F.J., A model function for ocean microwave brightness temperatures, *J. Geophys. Res.*, *88*, 1892-1908, 1983.

Wentz, F.J., Measurement of oceanic wind vector using satellite microwave radiometers, *IEEE Trans. Geosci. and Remote Sensing*, *30*, 960-972, 1992.

Wentz, F.J., A well-calibrated ocean algorithm for SSM/I, *J. Geophys. Res.*,*102*, 8703-8718, 1997.

Wentz, F.J., and R.W. Spencer, SSM/I rain retrievals within an unified all-weather ocean algorithm, *J. Atmospheric Science*, *55*, 1613-1627, 1998.

Weyl, P.K., On the change in electrical conductance of sea water with temperature, *Limnol. Oceanogr.*, *9*, 75-78, 1964.

Wilheit, T.T., and A.T.C. Chang, An algorithm for retrieval of ocean surface and atmospheric parameters from the observations of the Scanning Multichannel Microwave Radiometer (SMMR), *Radio Science*, *15*, 525-544, 1980.

Wu, S.T., and A.K. Fung, A non-coherent model for microwave emission and backscattering from the sea surface, *J. Geophys. Res.*, *77*, 5917-5929, 1972.

Yueh, S.H., W.J. Wilson, K. Li and and S.J. Dinardo, Polarimetric microwave brightness signatures of ocean wind directions, *IEEE Trans. Geosci. and Remote Sensing*, *37*, 949-959, 1999.

AMSR Precipitation Rate Retrieval Algorithm
--
Theoretical Basis and Operation

Grant W. Petty
Atmospheric and Oceanic Sciences
University of Wisconsin-Madison

1. Introduction

The Standard (pre-launch) Algorithm selected for over-ocean precipitation retrieval for the Advanced Microwave Scanning Radiometer (AMSR) is an adaptation of the algorithm developed for the Special Sensor Microwave/Imager (SSM/I) by Petty (1994a,b). The principle features that distinguish this algorithm from other rain rate algorithms include the following:

- Physical information concerning surface rain rate is supplied by the polarization difference at each frequency utilized in the inversion. As shown by Petty (1994a), a simple monotonic relationship exists between the local polarization difference and the total optical transmittance of the rain cloud at the frequency in question. The polarization difference is normalized with respect to a hypothetical cloud-free value under similar background conditions, thus eliminating variable water vapor and surface wind speed as important sources of systematic error in the retrieval.

- Scattering information at 89 GHz, as embodied by the *S* index of Petty (1994b), is postulated to contain only indirect information about surface rain intensity and it is therefore utilized only to generate the "first guess" rain rate field at high resolution. The first guess value at a local is modified only to the degree necessary to eliminate inconsistencies between calculated and observed polarization differences at the lower frequencies.

- The algorithm undertakes a spatial inversion of the polarization differences at the various frequencies utilized in the retrieval. That is, it iteratively seeks a high-resolution (5 km) rain rate field which is simultaneously consistent, to within specified tolerances, with the low-resolution fields of polarization difference observed at multiple frequencies. The disparate channel resolutions are explicitly accounted for in this inversion.

2. Algorithm Operation

2.1 Theoretical Basis

A number of factors make the optimal estimation of rain rate more difficult than the retrieval of many other parameters, such as column water vapor, column cloud water, etc. Examples include: (1) much larger optical thicknesses of precipitation and thus a high degree of non-linearity in both the forward and inverse problems; (2) the complexity of the interactions of microwave radiation (including scattering) with diverse liquid and frozen hydrometeors, whose physical and optical properties are highly variable in space and time; (3) the relative indirectness of the relationship between path-integrated cloud properties observable from space and surface precipitation rate; (4) the relatively poor spatial resolution of microwave radiometers compared with the horizontal scale of variability of rainfall; and (5) the highly 3-dimensional structure of many rain clouds. The last of these problems is further complicated by the oblique (55°) viewing angle of the AMSR, since it will often be emission from the sides and surface reflections of rain clouds, rather than their tops, that play a dominant role in FOV-averaged microwave radiances (Petty, 1994a; Petty *et al.*, 1994).

In view of the numerous physical and structural variables determining radiometer-observed brightness temperatures in any given pixel containing precipitation, it is important to make use of complementary information from as many channels as possible. It is further advisable to avoid attributing too great of precision to theoretically derived relationships, since such relationships generally do not allow for large departures of real rain clouds from common ideal assumptions, such as plane-parallel geometry.

The multichannel spatial inversion approach developed by Petty (1994b) attempts to achieve a balance between excessive reliance on uncertain physical models and excessive dependence on ad hoc statistical relationships and assumptions about beamfilling, etc. It attempts to maximize the use of the available information, but does so primarily by reference to observed path attenuation, rather than emission or scattering, so as to reduce the impact of uncertainties in the properties of frozen hydrometeors aloft.

This method is unusual in explicitly solving for a high-resolution rain field which is simultaneously consistent with the observed low-resolution polarizations at all frequencies, after allowing for the overlap and varying size of the effective fields of view (EFOVs). It also makes generous allowance for uncertainties in the highly simplified forward model and for geophysical noise of other types; thus, forward calculations are not forced to exactly agree with the observations but rather are considered consistent if they fall within a specified range of the observed values for each relevant microwave frequency.

In order to adapt the Petty (1994b) rain rate algorithm to the AMSR, two major revisions were necessary: (1) modification of the assumed antenna pattern and overlap coefficients utilized in the spatial inversion, and (2) development of a simple forward model for predicting brightness temperatures and polarizations specifically at AMSR frequencies and viewing angles. Furthermore, because the original SSM/I version of the algorithm was designed to operate within a much larger specialized display and analysis program for that sensor, considerable rewriting and reorganization of the C language code was necessary in order to repackage the algorithm as a self-contained subroutine (currently about 4000 lines of C and Fortran code).

2.1.1 *P* AND *S* INDICES

The foundation of the Petty (1994b) ocean rain rate algorithm lies in the use of polarization information to decouple scattering and attenuation information at a given microwave frequency. This information can then be utilized separately in the retrieval, weighted according to its relative directness as a measure of surface precipitation intensity.

As observed by the satellite, polarized brightness temperatures respond to uniform rainfall in the manner indicated by Fig. 1. For all frequencies, brightness temperatures first increase due to emission by rainfall as seen against a radiometrically cold ocean background. With increasing rain rate, saturation occurs first at the highest frequencies. At higher rain rates, scattering due primarily to large ice particles above the melting level begins to depresses brightness temperatures again. This effect is most pronounced at the highest frequencies, and its magnitude and spectral dependence is strongly dependent on assumptions about ice particle size and concentration above the melting level.

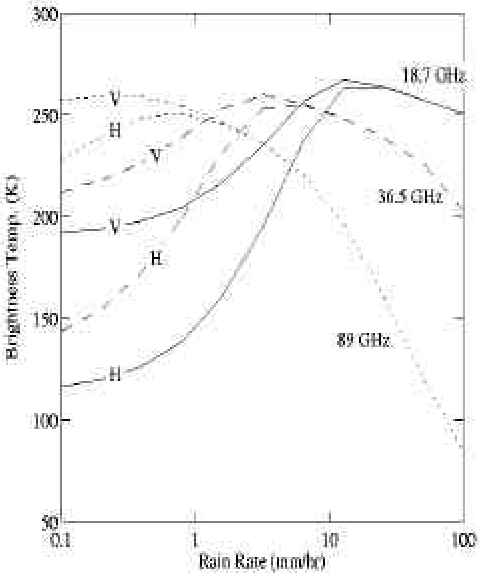

Figure 1: Idealized relationship between brightness temperature and surface rain rate for selected AMSR frequencies.

From this general behavior, it is clear that single-channel brightness temperatures from the AMSR yield an ambiguous measure of rain intensity, since it cannot be determined from the single brightness temperature whether one is on the left or right side of the peak for a given curve. Theoretically, one could resolve the ambiguity by using multiple frequencies at a single polarization, but this requires possibly unwarranted assumptions about the uniformity of rainfall within the widely differing FOVs of the respective channels.

When one considers the *difference* between the vertical and horizontal polarizations observed at a given frequency, the double-valuedness of the relationship disappears. The observed polarization difference $DT=T_V-T_H$

is essentially a monotonic measure of the visibility of polarized ocean surface emission through and between clouds and rain (this relationship breaks down somewhat in optically thick rain, owing to subtle effects by oriented ice particles). However, DT depends on other environmental properties as well, most notably total column water vapor V and surface wind speed U. It is therefore advantageous to define a so-called *normalized polarization* P as

$$P = \frac{\Delta T}{\Delta T_0 (U, V, ...)} \tag{1}$$

where DT_0 is the estimated cloud-free polarization difference at the time and location in question. The utility of this definition of P depends on one being able to make a reasonable estimate of U and V in locations of rainfall. This is accomplished either by direct retrieval from the AMSR data if the rain intensity is not too great or by interpolation into the rainy pixels from surrounding pixels.

Once P has been calculated for a given AMSR frequency, it serves as a physically direct index of total FOV-averaged path attenuation at that frequency due to clouds and rain only. It can be shown that, to a reasonable approximation (in view of many other unavoidable sources of error),

$$P \approx t^{a} \tag{2}$$

in the case of horizontal uniform coverage by rain and cloud, where τ is the oblique-path microwave transmittance through the rain layer, and $\alpha \approx 1.7$ is approximately independent of frequency. Although a minor modification is required to account for the polarizing effects of ice particles in optically thick rain clouds, the above relationship serves as the primary basis for inferring rain intensity in a given FOV. Fig. 2 depicts P as derived from the dual-polarization brightness temperature curves appearing in the left panel of the same figure.

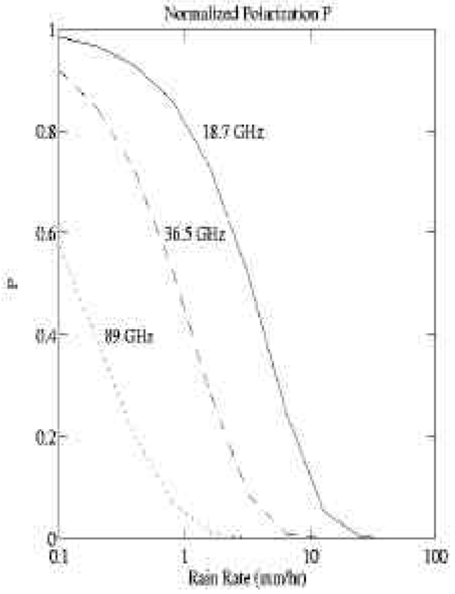

Figure 2: Idealized relationship between normalized polarization *P* and rain rate for selected AMSR frequencies.

Once a rain cloud becomes optically thick, the normalized polarization P saturates at a value near zero and yields no further information about surface intensity. Beyond that point, only the magnitude of the brightness temperature depression due to scattering by ice yields qualitative information about rain intensity. This information is indirect, because there is no unique relationship between the concentration and size of ice particles aloft and the intensity of surface precipitation. The so-called scattering signature is therefore weighted lightly in the algorithm, determining the surface rain rate only in cases where the estimate is not contradicted by evidence from the more physically direct P. In practice, this is accomplished by using the scattering information to specify the "first guess" rain rate and then modifying this rain rate estimate as necessary so as to eliminate inconsistencies with the observed P from the lower frequency channels.

As noted above, single channel brightness temperatures are ambiguous in that low values may imply either very light rain (and hence weak attenuation of the "cold" ocean surface emission or else heavy rain accompanied by much ice aloft. This ambiguity is again removed when one considers polarization in addition to brightness temperature: the unobscured ocean is "cold" but strongly polarized, whereas intense rainfall appears "cold" and only weakly polarized. The scattering index S for a given frequency is given by a linear combination of the vertical and horizontal polarized brightness temperatures. This index in effect compares the brightness temperature expected from a non-scattering, isothermal (T_C=273 K) cloud layer having the observed value of P with the observed brightness temperature. Thus,

$$S = P \cdot T_{V0} + (1 - P) \cdot T_C - T_V . \tag{3}$$

Fig. 3 depicts S as derived from the dual-polarization brightness temperature curves in Fig. 1.

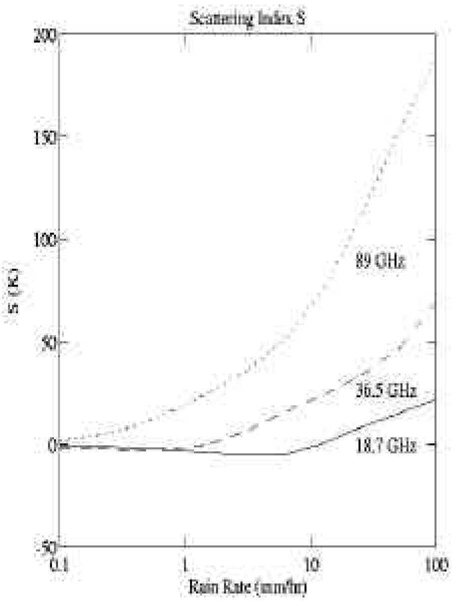

Figure 3: Idealized relationship between scattering index S and rain rate for selected AMSR frequencies.

Although all three frequencies show some scattering response to precipitation, only 89 GHz has a large enough response at modest rain rates to be routinely useful. Hence, S_{89} provides the first-guess rain rate R_0, based on the empirically determined linear relationship

$$S_{89} = C_S R_0 \tag{4}$$

A preliminary value of C_S is 2.9~K/(mm/h).

2.1.2 FORWARD MODEL

Although the relationship between P and total rain cloud transmittance τ is simple and relatively robust (for the horizontally homogeneous case), still needed is a model for the dependence of τ on rain rate R. We use the following expression

$$P_n = A_n \exp\left(-C_n Z_l R_n^B\right) \tag{4}$$

where Z_l is an effective rain layer depth (e.g. freezing level), and A_n, B_n, and C_n are frequency-dependent coefficients derived from theoretical calculations for a uniform Marshall-Palmer rain layer accompanied by an assumed 0.5 kg/m^2 of non-precipitating cloud water.

In the current version, Z_l is estimated empirically from the retrieved total column water vapor in the vicinity of the raining pixel. The justification for this method, and the actual relationship, is given by Petty (1994b). In future versions, we may instead utilize either NWP model-analyzed freezing level or else lower tropospheric temperature estimates derived from the 50-53 GHz channels of the ADEOS-2 AMSR.

Because the above model relationship for P_n is based on highly simplified assumptions, it is treated as an approximation with fairly generous uncertainties. Only pixels whose forwarded-calculated P_n differs by more than a specified tolerance ΔP_n from the observed value are considered “inconsistent,” thus requiring iterative modification of the retrieved rain rate field. However, when observed values of P from multiple channels are brought to bear, the requirement that the rain rate be consistent (to within tolerances) with all channels simultaneously constrains the retrieved rain rate rather effectively over a fairly wide range of intensities.

2.1.3 SPATIAL INVERSION

Not addressed so far is the problem of spatial inhomogeneity of rainfall within the respective fields-of-view (FOVs) of the channels used in the retrieval. Since each channel has a different resolution, one cannot assume that the same rain rate, or even that similar frequency distributions of rain rate, are present within each channel's FOV. Moreover, lower frequency channels have larger dynamic range (see Fig. 1) but lower sensitivity and also coarser spatial resolution than their higher-frequency counterparts. On the other hand, the coarser resolution FOVs overlap to a significant degree (i.e., are oversampled), suggesting the possibility of inverting the smoothed low-frequency polarization fields to obtain high-resolution rain fields. Such spatial deconvolution must be undertaken with care and with due consideration of the inherent ill-posedness of this kind of inverse problem in the presence of all forms of noise (instrument, geophysical, and that due to model errors).

The method developed by Petty (1994b) assumes that the rain rate is to be retrieved on a grid whose elements correspond to the positions of the high-resolution (89 GHz) channels' pixels. Unlike the 89 GHz FOVs, however, these grid elements, or retrieval cells, are contiguous and non-overlapping. Fig. 4 depicts the relationship between the fine-resolution rain rate retrieval grid and the effective FOVs of each relevant AMSR channel.

The observed P_{89} values are used to make an initial determination of whether rainfall is possible within a given high-resolution retrieval cell. If P_{89} is greater than a specified threshold, the pixel is deemed rain-free; otherwise it is flagged as “rain possible.” The observed S_{89} value is then used to assign a first-guess rain rate to each cell identified as “rain possible,” according to (4).

The next step is to forward-calculate the normalized polarization (P) field from the first-guess rain rate. This is accomplished by first computing local values P_i for each high resolution retrieval cell using (5), and then taking a weighted sum of these values within each FOV to derive an estimate of the low-resolution value of $\overline{P}$ corresponding to a given image pixel:

$$\overline{P_j} = \sum_i w_{i,j} P_j . \tag{6}$$

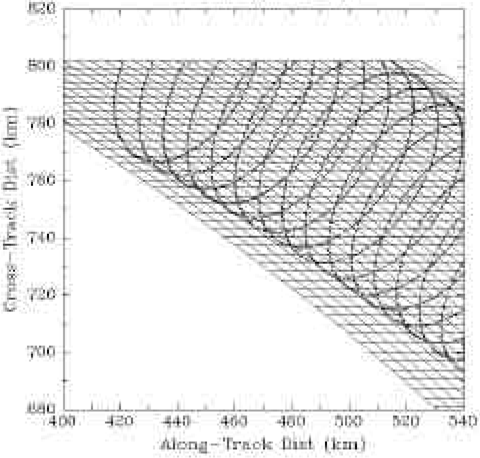
6.9 GHZ Sample Geometry

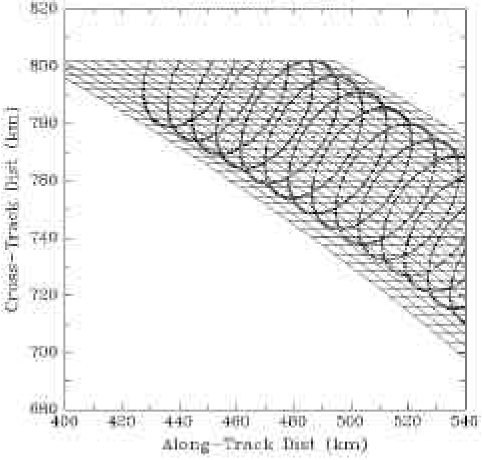
10.65 GHZ Sample Geometry

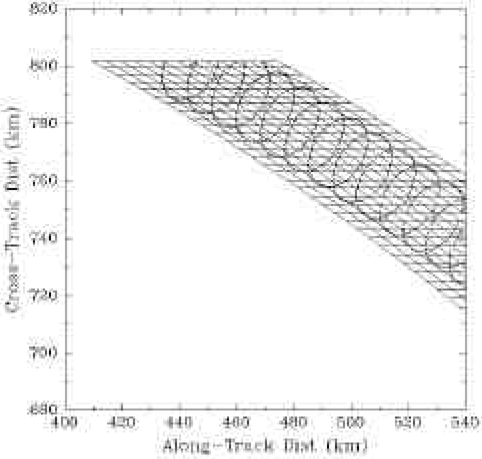
18.7 GHZ Sample Geometry

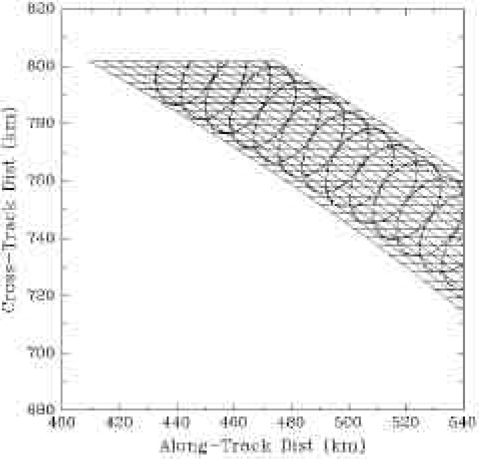
23.8 GHZ Sample Geometry

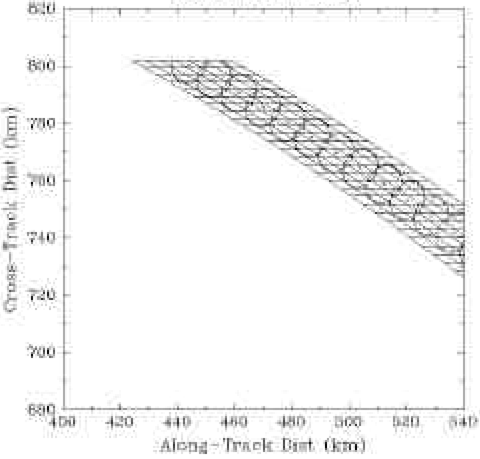
36.5 GHZ Sample Geometry

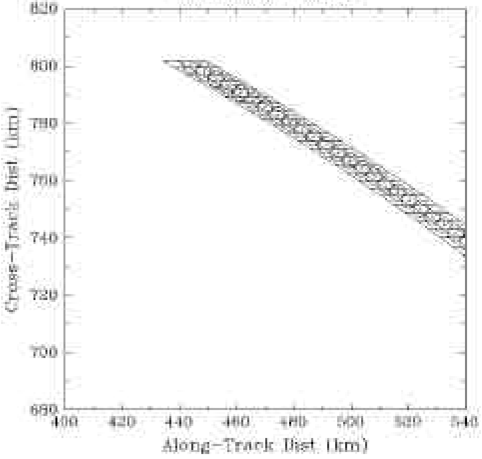
89.0 GHZ Sample Geometry

Because the spatial relationship and degree of overlap between sensor pixels and retrieval cells is fixed at any point in a scan line, the coefficients $w_{i,j}$ are pre-computed for all channels and stored in arrays which are accessed by the algorithm during both the forward and inverse calculations.

For each sensor pixel for which the forward-computed $\overline{P}$ differs from the observed $\overline{P}$ by more than the specified tolerance *DP*, an adjustment is undertaken of the rain rates in the retrieval cells covered by that sensor FOV. Only retrieval cells identified as "rain possible" are candidates for adjustment. The magnitude of the adjustment is largest for the retrieval cells having the largest potential influence on the forward-calculated polarizations. Thus, where two different FOVs overlap a given retrieval cell, the one with the greatest sensitivity to changes in the rain rate in that cell will have the greatest control over the adjustment. Low sensitivity to changes in a given rain retrieval cell can be due either to saturation at the current-guess rain rate or else the position of the cell in the FOV.

The above adjustment is performed for all pixels flagged as "inconsistent" and this adjustment is performed in turn for each frequency utilized in the inversion (currently 18.7 and 36.5 GHz). The process is repeated a fixed number *N* times, after which it is assumed that no further improvement can be expected. Because of the differing resolutions and sensitivities of the different channels, it is rare that convergence, or near convergence, is not obtained at most locations, provided only that the tolerances are not set too tight. Optimal tolerances and iteration counts are best determined empirically, using real data where possible. For the SSM/I, $DP = 0.1$ and $N = 8$ yielded good results, but we are testing new values using the synthetic swath data supplied by NASDA/EORC.

3. Testing

Previous experience with this algorithm was based on the SSM/I version of the Petty (1994b) algorithm, which has been extensively intercompared with ground validation data in AIP-1, AIP-2, AIP-3, PIP-1, PIP-2, and PIP-3, as well as several "private" intercomparison studies. In the most recent two organized intercomparisons (AIP-3 and PIP-3), the results for the SSM/I version were very satisfactory by some measures. In particular, this algorithm had by far the highest instantaneous correlation with radar at 0.5° resolution in AIP-3. In PIP-3, it was one of the very few algorithms that simultaneously yielded good rms errors against monthly atoll rainfall amounts and also a high global time-space correlation with a ship-derived climatology of fractional-time-precipitating (Adler *et al*., 2000).

Future testing plans include validation of the algorithm using data from the TRMM Microwave Imager (TMI), which is already flying and has many similar channels to AMSR. While the adaptation of the algorithm to TMI from AMSR will be much less arduous than was the adaptation from SSM/I to AMSR (since the previous adaptation was undertaken with future flexibility in mind), it is still a non-trivial task, owing to the need to derive yet another set of FOV overlap coefficients $w_{i,j}$ and other sensor-specific coefficients.

4. Known Issues and Future work

4.1 Scan geometry

A quantitative description of FOV overlap between adjacent pixels and between different channels of the AMSR was recently provided by EORC but has still not been incorporated into the algorithm. Antenna pattern overlap coefficients provided with current version are based on the assumption of Gaussian effective antenna weighting patterns.

4.2 Channel Usage

The present version utilizes only 18.7 and 36.5 GHz channels, corresponding to the original SSM/I channels of 19.35 and 37.0 GHz. Future versions may utilize 6.9 and 10.7 GHz channels as well, but the tradeoffs between computational effort, inversion stability, and retrieval performance improvement must be studied first.

4.3 Cloud free brightness temperatures

A prerequisite for the transformation of the raw polarized brightness temperatures into the *P* and *S* variables utilized in the physical inversion is a reasonably accurate estimate of the cloud-free brightness temperature in both vertical and horizontal polarization. Currently, this is achieved by first retrieving column water vapor *V* and

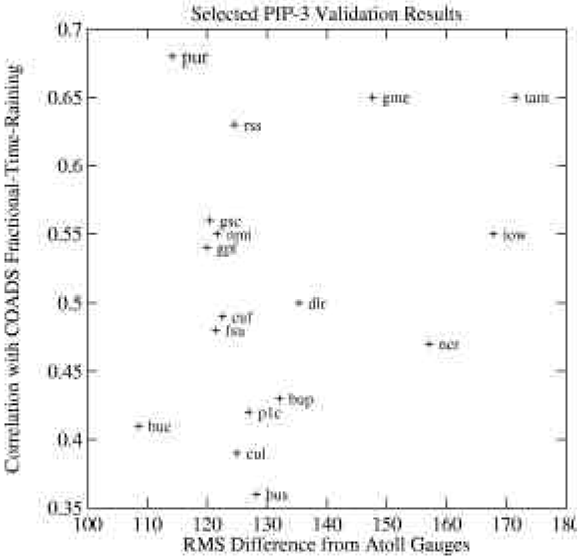

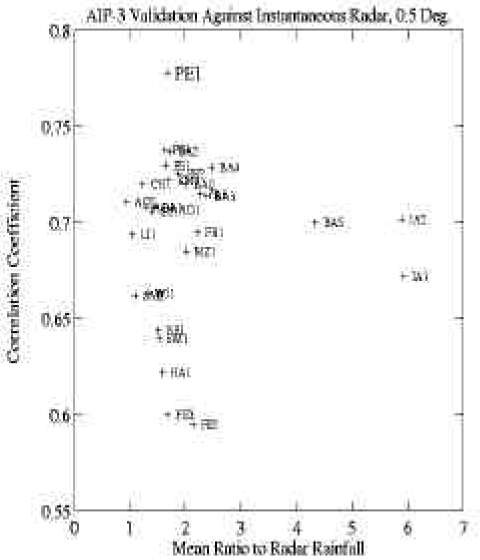

surface wind speed

Figure 5 (left): Validation results over 12 months (1992) of monthly rainfall products submitted to PIP-3. Only “pure SSM/I” algorithms are indicated in this figure. The horizontal axis indicates the RMS difference from atoll gauges. The vertical axis indicates the global correlation with ship-derived fractional-time-raining between 60S and 60N. Both sets of statistics were obtained from the PIP-3 Intercomparison Results volume. Only algorithms for which both statistics were available are included. The Petty (Purdue U.) physical algorithm is denoted “pur” in this intercomparison.

Figure 6 (right): Instantaneous validation results for SSM/I algorithms submitted to AIP-3, at 0.5 degree resolution. The horizontal axis depicts the mean ratio over the entire intercomparison period of the algorithm rainfall to the radar rainfall. The vertical axis depicts the correlation coefficient. Note that there is some uncertainty concerning the absolute calibration of the radar data – most algorithms (both SSM/I and IR) clustered around a ratio of approximately 1.5 to 2.5. The Petty physical algorithm was denoted “PE1” in this intercomparison.

U outside of areas of significant precipitation. These retrieved values are then interpolated into areas of precipitation and used to estimate cloud free brightness temperatures based on a simple empirical model which has again been adapted from the SSM/I.

For the pre-launch versions of the algorithm, it is necessary to extrapolate empirical relationship derived for the SSM/I to the slightly different frequencies and viewing angle of the AMSR. This extrapolation unavoidably depends on physical models whose absolute accuracy is imperfect. Consequently, we expect some systematic biases in the determination of cloud free radiances. This biases could in turn introduce errors or inconsistencies into the rain rate retrievals until the biases are corrected post-launch.

For the post-launch version of the algorithm, actual AMSR observations will be available in order to fine-tune both the *U* and *V* retrievals and the prediction of cloud-free T_B from *U* and *V*. Alternatively, the *U* and *V* values obtained from the Standard Algorithm for those variables may be utilized.

References

Adler, R., C. Kidd, G. Petty, M. Morrissey, and M. Goodman, 2001: Intercomparison of global precipitation products: The third precipitation intercomparison project (PIP-3). *Bull. Amer. Meteor. Soc.* (in press).

Petty, G., A. Mugnai, and E. Smith, 1994: Reverse Monte Carlo simulations of microwave radiative transfer in realistic 3-D rain clouds. In 7^{th} *Conference on Satellite Meteorology and Oceanography, Monterey, California, 6-10 June.*

Petty, G. W., 1994a: Physical retrievals of over-ocean rain rate from multichannel microwave imagery. Part I: Theoretical characteristics of normalized polarization and scattering indices. *Meteorology and Atmospheric Physics*, **54**(1-4), 79-100.

Petty, G. W., 1994b: Physical retrievals of over-ocean rain rate from multichannel microwave imagery. Part II: Algorithm implementation. *Meteorology and Atmospheric Physics*, **54**(1-4), 101-121.

Description of Precipitation Retrieval Algorithm For ADEOS II AMSR

Guosheng Liu
Florida State University

1. Basic Concepts of the Algorithm

This algorithm is based on Liu and Curry (1992, 1996), in which the rainfall rate is calculated from the combination of emission and scattering signatures. Beam-filling correction is embedded in the algorithm. Radiative transfer model tests show that it is not sensitive to the height of freezing level. This algorithm was tested in GPCP AIP-1, AIP-3, WetNet PIP-2 and PIP-3. The algorithm can retrieve rainfall over both ocean and land although slightly different formulations are used for the different surface types.

The AMSR algorithm is built on the SSM/I algorithm with conversions from AMSR brightness temperatures to SSM/I brightness temperatures.

Ocean Algorithm:

In this updated version, the combination function is defined by Liu et al. (1995) as following:

$$f = (1 - \frac{D}{D_0}) + 2(1 - \frac{PCT}{PCT_0}) \tag{1}$$

where D is the depolarization of 18.7 GHz and D_0 is D at the threshold of rain onset; PCT is the polarization corrected brightness temperature defined by (Spencer et al., 1989): $PCT = 1.818T_{B89V} - 0.818T_{B89H}$, and PCT_0 is PCT at the threshold of rain onset. PCT and D for AMSR channels are then converted to SSM/I PCT and D by the following equations:

$$\begin{aligned} PCT_{SSM/I} &= 2.2 + 0.996 PCT_{AMSR} \\ D_{SSM/I} &= -0.14 + 0.903 * D_{AMSR} \end{aligned} \tag{2}$$

These equations are derived by radiative transfer simulations for various atmospheric and surface conditions. Then rainfall rate are calculated based on the equations originally derived from SSM/I channels.

D_0 and P_0 are determined monthly for every 3° (latitude) x 6° (longitude) box based on 37 GHz depolarization and sea surface temperature, and are saved in a file as a look-up table. The relationship between f and rainfall rate is determined by radiative transfer calculation result with consideration of beam-filling effect, and can be expressed by

$$R = af^{b} \tag{3}$$

where α and β are spatial scale-dependent coefficients. The dependence of α and β on spatial scale is due to the spatial dependence of beam-filling effect. For SSM/I in which the spatial resolution of 19 GHz is ~ 50 km, α=10.6 and β=1.621. For AMSR and TMI, the spatial resolution for 19 GHz is about half of that in SSM/I. The values for α and β are determined by an empirical equation based on radiative transfer model simulation and TMI data: α=8.25, and β=1.88. Test results show that these coefficients produce satisfactory rain rates from TMI data when compared to TRMM PR rain rates and GPCP climatology. Detailed discussion is given in section 2 on the scale-dependent parameters, α and β.

Land Algorithm:

The land portion of our algorithm uses 18.7 and 89 GHz brightness temperatures. It is expressed by

$$R = a(DT_B - DT_{B0}) \tag{4}$$

where a=0.2 is a coefficient derived from radiative transfer model simulations; $DT_B=T_{B18.7}-T_{B89}$. Again, we first convert DT_B for AMSR to DT_B for SSM/I by

$$DT_{BSSM/I} = -0.6 + 0.9558DT_{BAMSR} \tag{5}$$

Then the rainfall algorithm originally developed for SSM/I is used.
DT_{B0} is DT_B at the threshold of rain onset that is determined monthly for every 3° (latitude) x 6° (longitude) box based on Liu and Curry (1992) and is saved in a file as a look-up table.

The algorithm is deterministic (non-iterative) and all threshold parameters (D_0, PCT_0, and DT_{B0}) are available as a look-up table. Therefore, the retrieval is extremely fast.

2. Determination of the Scale-Dependent Parameters

Results of earlier studies (e.g., Liu and Curry, 1992, Spencer et al., 1989) showed that the beam-filling effect tends to make the R-T_B relation closer to "linear" than that indicated by radiative transfer models assuming a plane-parallel rain layer. Liu and Curry (1992) tried to explain this behavior of R-T_B relation. The determination of α and β in this algorithm is based on this consideration. First, we assume the parameter β in (3) varies with spatial scale, x (in km), as

$$\beta = \beta_\infty - A[1-\exp(-Bx^\kappa)], \tag{6}$$

where β_∞=2.792 is β for plain parallel rain layer determined by our radiative transfer simulations. κ is an adjustable parameter used to vary the strength of scale dependence. For now we use κ=0.7 which seems to work well for our algorithm for TMI and SSM/I data. A and B are determined as following. First, when scale, x, becomes infinite large, β is 1, implying that for infinitely large spatial resolution the R-T_B relation is linear (note the argument mentioned earlier). Then, it is determined that $A = \beta_\infty - 1$. The constant B is then determined by applying (6) to our SSM/I algorithm used in Liu and Curry (1996), which gives β_{SSMI}=10.6 for a scale of 50 km.

In the studies of Liu and Curry (1992), it is also found that when rainfall rate is as high as 50 mm/hr, the ratio between observed T_B and plane-parallel model generated T_B should be close to 1. Based on this argument, we determine α by letting

$$\left(\frac{R_{50}}{\alpha_{AMSR}}\right)^{\frac{1}{\beta_{AMSR}}} = \left(\frac{R_{50}}{\alpha_{SSMI}}\right)^{\frac{1}{\beta_{SSMI}}} \tag{7}$$

where R_{50}=50 mm/h.

It is noted that the development of the parameters of α and β are based on the algorithm we developed for SSM/I. Figure 1 shows the f-R relations derived from the aforementioned approach for different spatial resolutions. For very high resolution, we may believe the rainfall within the FOV is homogenous. For very low resolution, the f-R relation is assumed to be linear. Actual satellite measurements (AMSR, TMI, SSM/I) will have an f-R relation curve between the two extremes.

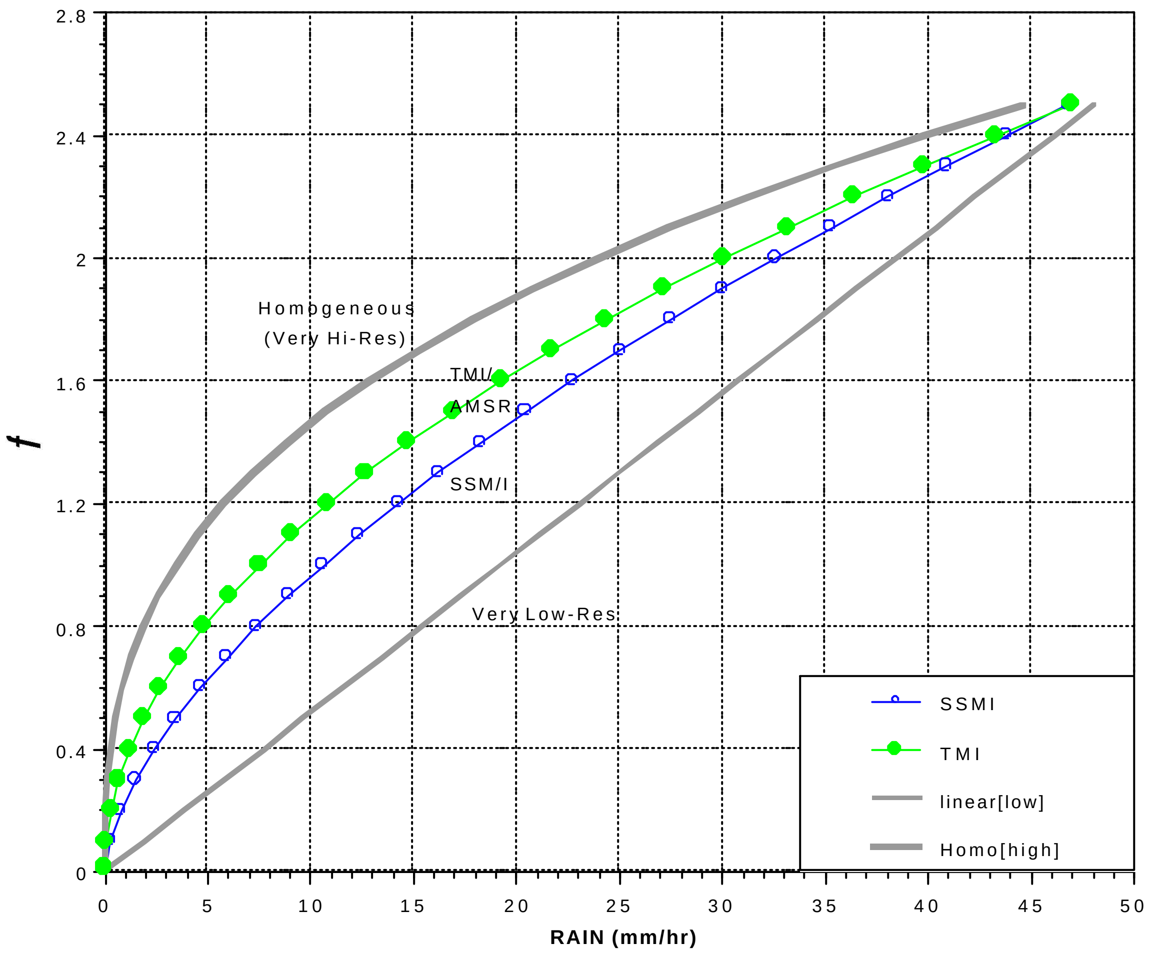

Fig. 1 Relations between f and rainfall rate for different spatial resolutions.

3. Validation -- Comparison with Other Datasets

Figure 2 shows the comparison of this algorithm using SSM/I data with GPCP satellite-raingauge combined monthly rainfall product (Huffman, et al., 1997) for the year of 1992. The two retrievals are generally agreed with each other although some discrepancies can also be found; such our retrievals are general lower, particularly for latitudes where precipitation peaks. This disagreement can partially be attributed to the low temporal coverage of SSM/I data.

Figure 3 shows the comparison with TRMM TMI-PR combined (3B31) product and GPCP satellite-raingauge combined product for 1998. Our retrievals seem to compare well with these products. We are still working on this comparison for other years to investigate whether there are discrepancies for those years. Further investigation may lead modification of the tuning parameter, κ, given in (6). Figure 4 shows the comparison with product derived from TRMM PR alone. The latitudinal variation of the two estimates agrees well although our estimates are slightly larger than the PR estimates. It is noted that PR estimates are also smaller than TRMM TMI and TRMM Combined products.

The following table lists the bias, correlation coefficient and rms difference when of our algorithm when compared to TRMM combined and GPCP products. The statistics are calculated using 1998 monthly 5° x 5° datasets.

Statistics When Compared to TRMM Combined and GPCP Data

	Bias in %	Correlation	rms Diff in %
GPCP	1%	0.78	69%
TRMM Combined	6%	0.82	61%

4. References

Huffman, G. J., R. F. Adler, P.A. Arkin, A. Chang, R. Ferraro, A. Gruber, J. Janowiak, R.J. Joyce, A. McNab, B. Rudolf, U. Schneider, and P. Xie, 1997: The Global Precipitation Climatology Project (GPCP) Combined Precipitation Data Set. Bull. Amer. Meteor. Soc., 78, 5-20.

Liu, G., and J. A. Curry, 1992: Retrieval of precipitation from satellite microwave measurements using both emission and scattering. *J. Geophys. Res.*, **97**, 9959-9974.

Liu, G., and J. A. Curry, 1996: Large-scale cloud features during January 1993 in the North Atlantic Ocean as determined from SSM/I and SSM/T-2 observations. *J. Geophys. Res.*, **101**,7019-7032.

Liu, G., J. A. Curry and R.-S. Sheu, 1995: Classification of clouds over the western equatorial Pacific Ocean using combined infrared and microwave satellite data. *J. Geophys. Res.*, **100**, 13,811-13,826.

Spencer, R. W., H M. Goodman, and R. E. Hood, 1989: Precipitation retrieval over land and ocean with SSM/I: Identification and characteristics of the scattering signal. J. Atmos. Oceanic Technol., 6, 254-273

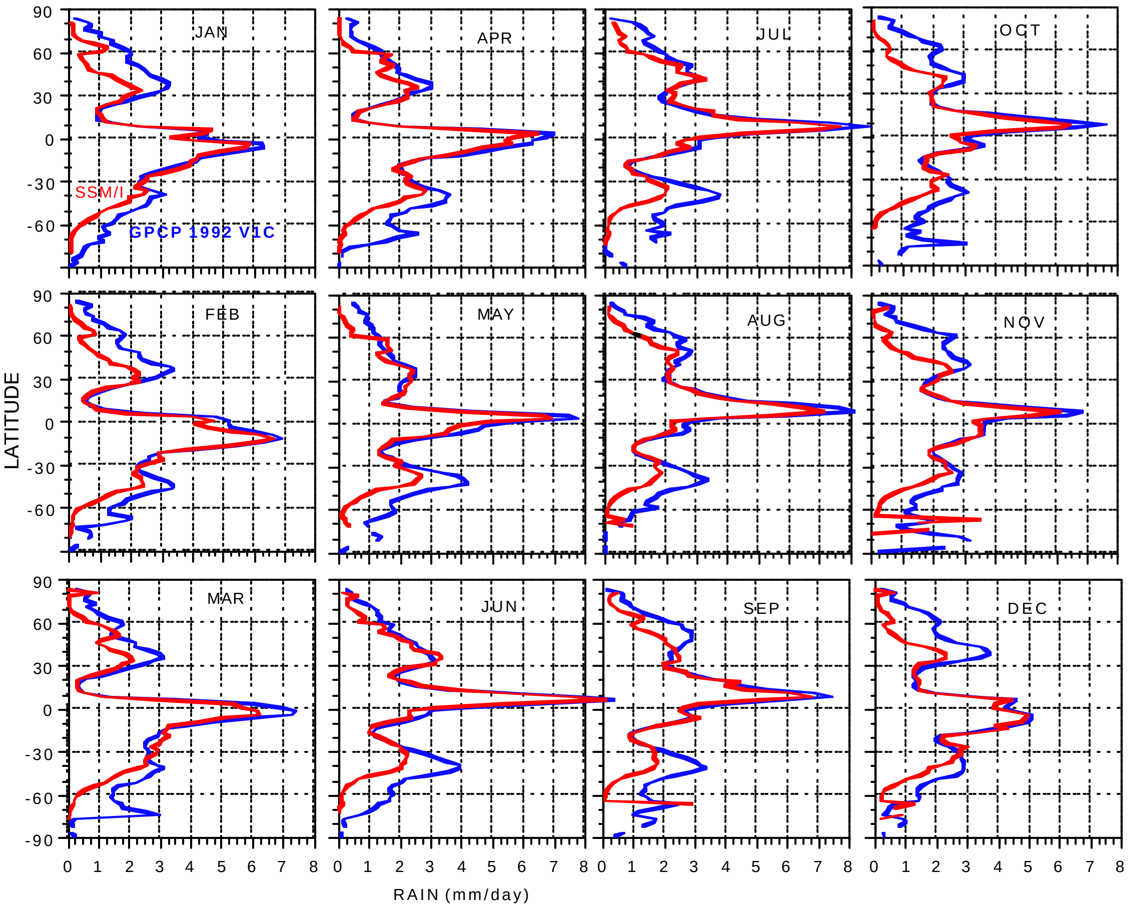

Fig. 2 Comparison with GPCP satellite-raingauge combined rainfall(blue).

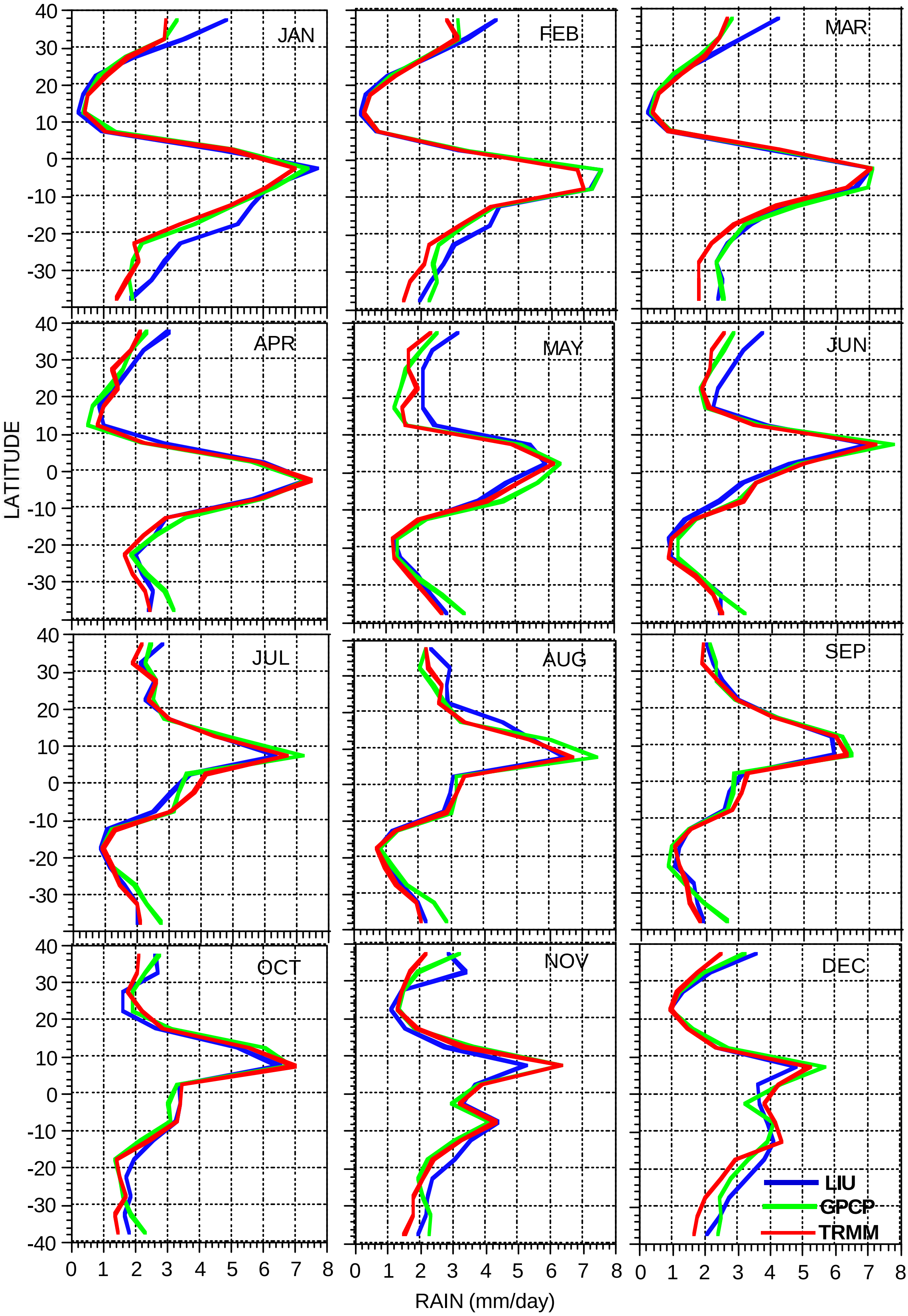

Fig.3 Comparison with TRMM combined (red) and GPCP (green) products for 1998.

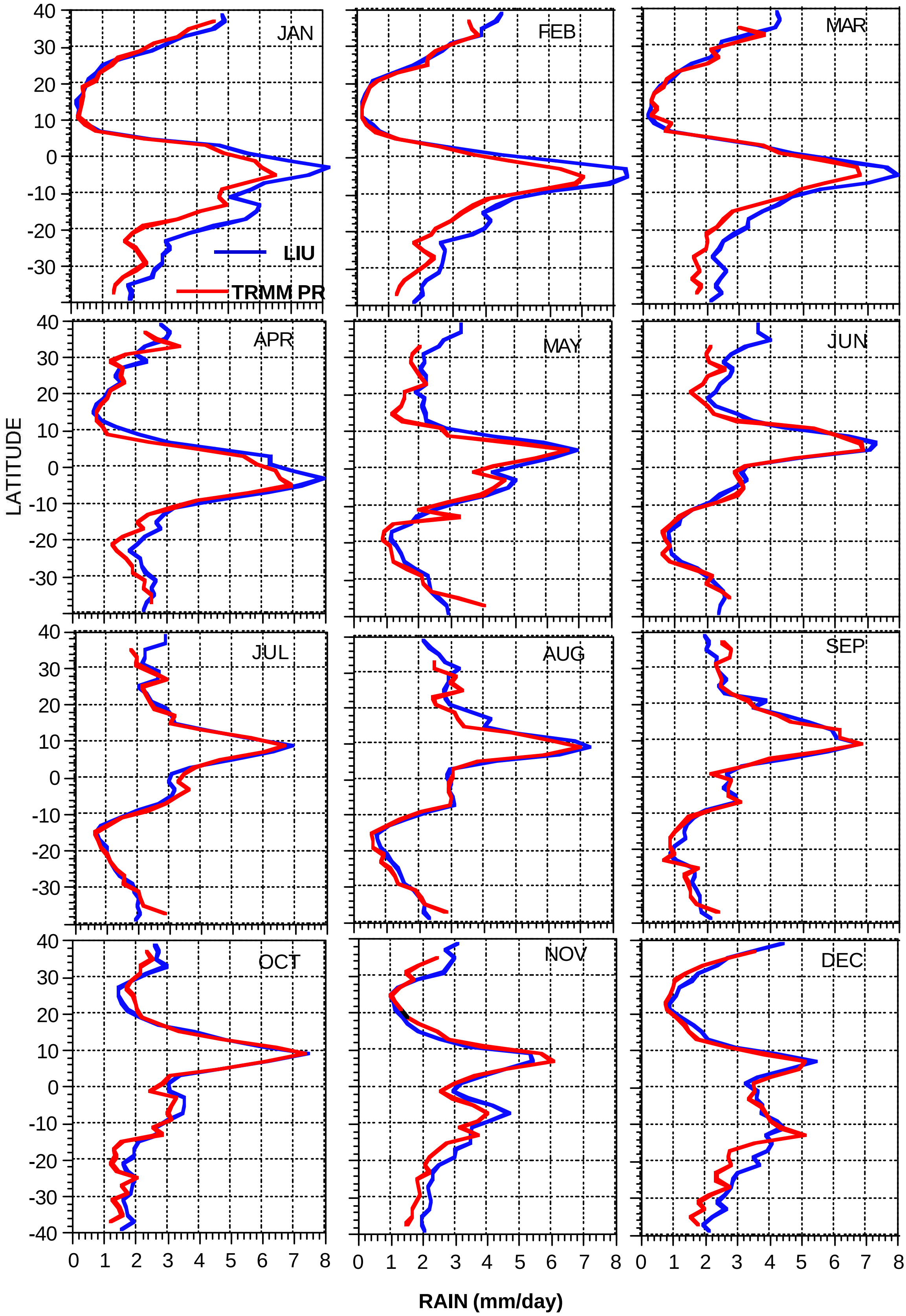

Fig. 4 Comparison with TRMM Precipitation Radar (red) product for 1998.

AMSR/AMSR-E Sea Surface Wind Speed Algorithm

Akira SHIBATA
Meteorological Research Institute

1. Abstract

Sea surface wind speed (SSW) is retrieved mainly from 37 GHz vertical (V) and horizontal (H) brightness temperature of AMSR/AMSR-E by a graphical method. The retrieval is restricted to no rain condition, since the brightness temperature of 37 GHz is saturated under rainy condition, SSW obtained from 37 GHz has a large anisotropic feature depending on an angle difference between antenna direction and wind direction. Its anisotropic feature is corrected by using two data from 37 and 10 GHz, since 10 GHz data are less anisotropic. Even under rainy condition, 10 and 6 GHz data are not saturated, so wind speed will be able to be retrieved by using those horizontal data. Retrieval accuracy of wind speed using 10 and 6 GHz will become worse than using 37 GHz, since a sensitivity of 10 and 6 GHz to wind speed is not so strong.

2. Wind speed from 37 GHz

The brightness temperature of vertical (V) polarization does not change under condition of sea surface wind speed less than 7 - 8 m/s. But, the one of horizontal (H) polarization increases monotonically with wind speed. At 37 GHz, the sensitivity is about 1K/(m/s). Above 7- 8 m/s of wind speed, both V and H temperature increase. Fig. 1 shows a thematic method of calculating wind speed. A line shown by “A” represents a calm sea state, and line “B” represents a roughened sea state. SSW is calculated from a horizontal length of “C” shown in Fig. 1. When atmospheric opaque due to water vapor and cloud liquid water increase, both V and H temperature increase. The atmospheric opaque is corrected by a convergence made by two lines of A and B. A position of the line A is changed in accordance with SST change, and coefficients of slope and intercept defining the line A are also changed. Those coefficients given at 5 °C interval of SST from 0 to 35 °C.

The brightness temperature of 37 GHz is saturated under rainy condition, i.e., the ocean surface can not be seen by 37 GHz data. A judge whether 37 GHz data can be used is made by using the value defined in Fig.1 in the AMSR/AMSR-E SST algorithm.

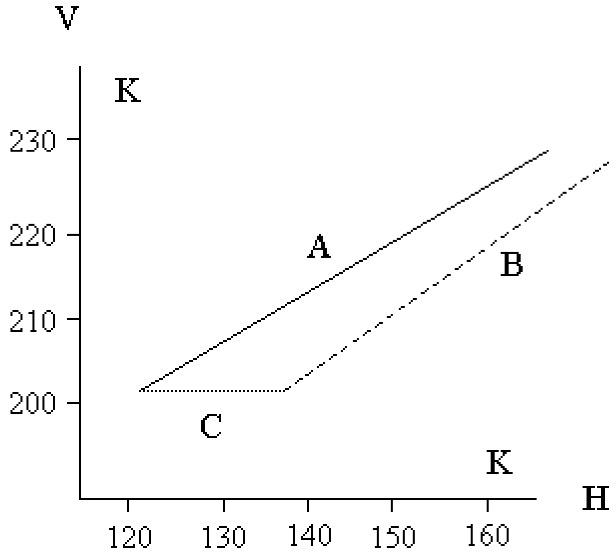

Fig. 1 Retrieval of wind speed from the vertical and horizontal polarization data

3. Correction of anisotropic wind speed

SSW obtained by the method described in § 2 has a large anisotropic feature depending on an angle between the antenna direction and wind direction. Airborne Microwave Radiometer (AMR) experiments of NASDA suggest that at about 9 m/s of wind speed, a difference of the length C defined in Fig. 1 reaches about 4K between the downwind and upwind case. In such a condition of wind speed, the brightness temperature of V polarization of the upwind direction is larger by about 2K than one of the downwind direction, and the difference of H polarization is about 1K. At lower frequencies such as 10 or 6 GHz, the anisotropic features become weaker. Even at 13 - 14 m/s of wind speed, the difference is less than 1 K at 10 GHz.

In the current algorithm, the anisotropic feature is corrected by a combination of two lengths C from 37 and 10 GHz. Fig. 2 shows a thematic method to correct the anisotropic feature. C from 37 GHz has the larger anisotropic feature than one from 10 GHz. Above 7 - 8 m/s of wind speed, two lengths C calculated from 37 and 10 GHz take different values between the downwind and upwind cases as shown in Fig. 2. The anistropic feature is corrected by taking a middle position.

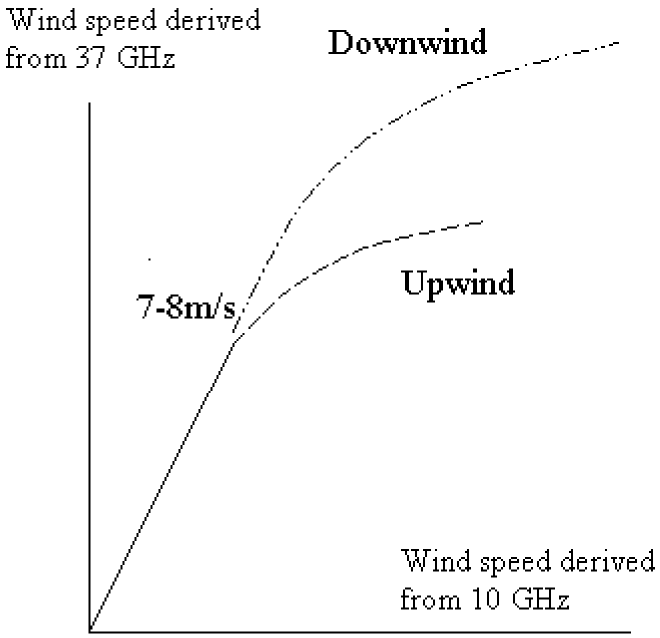

Fig. 2 Correction of anisotropic feature by using 37 and 10 GHz data

4. Wind speed from 6 and 10 GHz under rainy condition

The brightness temperature of 37 GHz is saturated under rainy condition, but ones of 10 or 6 GHz are not saturated in almost cases. The sensitivity of H polarization at 37 GHz to wind speed is about 1K/(m/s) as mentioned above, and ones of 10 and 6 GHz H are about 0.6K/(m/s). A retrieval accuracy using the former data is much better than the latter data, but 10 and 6 GHz H data can be used in retrieval of wind speed under rainy condition. The brightness temperature due to water vapor, liquid water (totally they are called as atmospheric opaque) increases as different behavior between 6 and 10 GHz. The brightness temperature change due to wind effect is almost same between 6 and 10 GHz. So, wind speed will be separated from the atmospheric opaque from two data of 6 and 10 GHz H.

5. Reference

Shibata A. (1996) :Remote sensing on ocean surface by passive microwave radiometer , Kishou Kenkyu Note, no. 187, pp. 53-63.

AMSR/AMSR-E Sea Surface Temperature Algorithm

Akira SHIBATA
Meteorological Research Institute

1. Abstract

Sea Surface Temperature (SST) is retrieved mainly from AMSR/AMSR-E 6GHz and 10 GHz vertical polarization (V) data, by using 37 GHz V and H (horizontal), 23 V, 6H, and 10H data as supplements. The current SST algorithm includes following nine procedures.
(a) Incident angle correction
(b) Atmospheric (water vapor, cloud liquid water) correction
(c) Surface wind correction
(d) Land contamination correction
(e) Removal of sunglitter area
(f) Salinity correction
(g) Removal of sea ice area
(h) Conversion to SST
(i) Spatial running mean
A target of retrieved SST accuracy is within 0.5 - 0.7℃ when compared with buoy SST.

2. Detailed data processing procedures

(a) Incident angle correction

Correction of the brightness temperature, dA, due to incident angle variation is given by the following equations;

$dA = -2.9*(A - 55.0)$ 6 GHz V
$dA = -2.7*(A - 55.0)$ 10 GHz V,

where A is the incident angle. The horizontal polarization data are also corrected by similar equations.

(b) Atmospheric correction

Correction for atmospheric opaque is obtained from a pair of two temperatures of 23 GHz V and 37 GHz V. Fig. 1 shows an example of getting the correction value for TMI 10 GHz which reads 37V and 21V to give the correction value for 10V. Because brightness temperatures of 23V and 37V are changed with SST, the table is made with 5°C interval of SST from 0 to 35 ℃. It is necessary to omit data contaminated by rain, since SST accuracy becomes worse in rainy areas. Its judge is made by counting the number of pixels within 6 GHz or 10 GHz spatial resolution, in which the correction value shown in Fig. 1 is out of specified range. If the number of pixels with out of range is larger than a threshold, SST is missing.

(c) Surface wind correction

Correction for sea surface wind is made independently from two frequencies ;6V and 6H, and 10V and 10H, which are already corrected for atmospheric opaque. Fig. 2 shows a thematic map to make the wind correction. Brightness temperature of V polarization is almost constant under a condition of sea surface wind speed less than 7 - 8 m/s. But, the one of H polarization increases uniformly. Above 7 - 8 m/s, both brightness temperature of V and H polarization increase with wind speed, whose ratio is about 1 /1.7. This ratio may depend on a relative angle between the wind direction and antenna direction, and also on a difference between SST and air temperature.

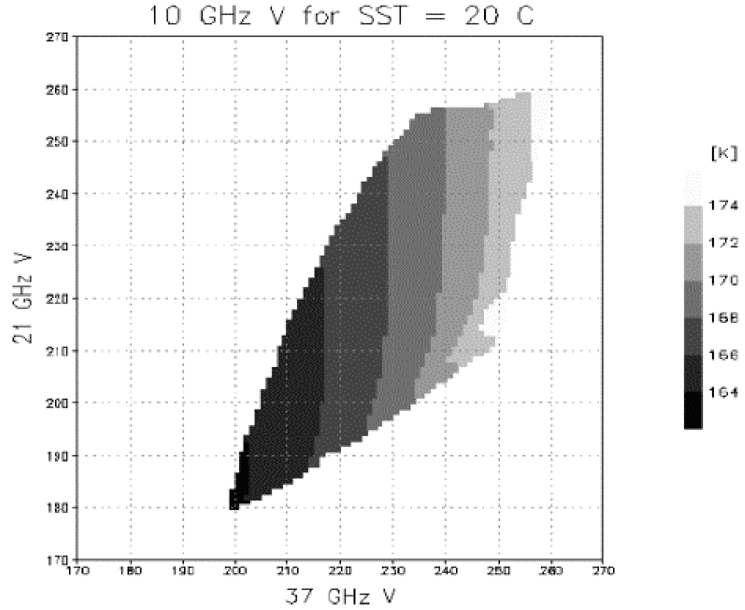

Fig. 1 Effect of atmospheric opaque for 10 GHz V

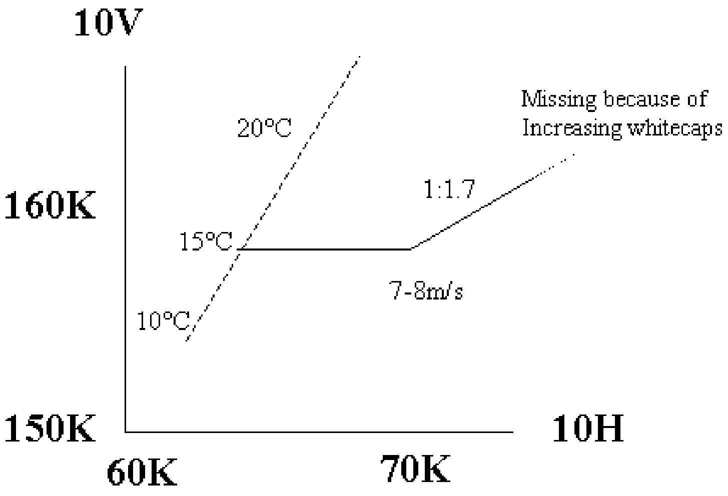

Fig. 2 Effects of surface wind for 10 GHz V and H

(d) Land contamination correction

Contamination by land emission increases drastically when the pixel approaches a shoreline, or the pixel includes an island. Here, land contamination is corrected for pixels that the increment is less than 2 K. For pixels of contamination larger than 2 K, SST is missing.

(e) Removal of sunglitter area

Sunglitter is checked by using a relative angle between the antenna beam direction and sun direction, which is given by L1B. SST is missing for pixels of the relative angle larger than 30°.

(f) Salinity correction

Salinity effect can not be neglected when SST is high as 30 °C, and the correction value is an order of 0.1 or 0.3 K. Its effect is calculated in advance by using the climate salinity, and a data set of correcting salinity effect is prepared with spatial resolution of 1 degree. This data set is not modified even after the launch.

(g) Removal of sea ice area

Sea ice will be detected by checking the value obtained from the atmospheric correction. If its value exceeds 5.5 K in the latitude larger than 65°, it is judged that the pixel is contaminated by sea ice. SST is missing when the number of pixels with sea ice contamination exceeds a specified value.

(h) Conversion to SST

The relationship between 6V (or 10V) and SST is calculated by using the complex relative dielectric constant given by Klein and Swift (1977). Fig. 3 shows its the relationship.

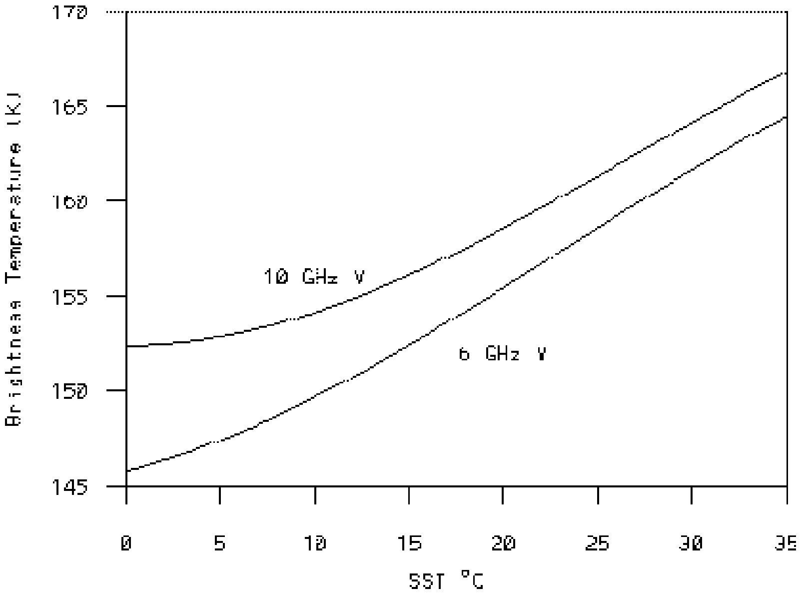

Fig. 3 Relation between SST and 6 V (or 10V)

(i) Spatial running mean

The temperature resolution at 6 GHz is about 0.3 K for one pixel, which is corresponding to about 0.6°C of SST. It is necessary to reduce its noise. A current method is a spatial running mean with 5 pixels by 5 pixels (50 km by 50 km area). The simulation indicates the reduced noise becomes less than 0.1 K after applying 5 by 5 running mean.

3. References

Shibata A., K. Imaoka, M. Kachi, and H. Murakami (1999) :SST Observation by TRMM Microwave Imager aboard Tropical Rainfall Measuring Mission, Umi no Kenkyu, vol.8, no.2, pp. 135 to 139 (in Japanese)

ALGORITHM THEORETICAL BASIS DOCUMENT (ATBD)
FOR THE
ADEOS/AMSR SEA ICE ALGORITHM

Josefino C. Comiso
Laboratory for Hydrospheric Processes
NASA Goddard Space Flight Center

1. Introduction

During the last century, the average global temperature has been increasing at the rate of 0.05K per decade (Jones, 1999). Because of feedback effects associated with the high albedo of ice and snow, such increases in temperature are expected to be amplified in polar regions (Budyko, 1966). Recent observations suggest that the Arctic environment may indeed be changing. Limited submarine sonar data indicate that the Arctic sea ice cover has been thinning by more than one meter in the last few decades (Rothrock et al., 1999; Wadhams and Davis, 2000, and Tucker et al., 2001) while sea ice extent in the same region has declined by about 5 to 6% in the last two decades (Bjorgo et al., 1997; Parkinson et al, 1999). Even more intriguing is the observation that the perennial sea ice cover is retreating at the much faster rate of 7-8% per decade (Johannessen et al., 1999; Comiso, 2001). The implication of the latter if the rate persists is that in a matter of a little more than a century, the perennial sea ice cover may disappear completely, causing profound changes in the characteristics, climate, and ecology of the Arctic system. To get this phenomena in proper perspective, more in depth studies of the changes in the global sea ice cover and associated changes in the environment are needed.

Sea ice covers a significant fraction of the global oceans (about 5 to 8%) and is one of the most seasonal parameter on the Earth's surface. Its high albedo, which ranges from about 80% (Grenfell, 1983) to 98% (Vowinckel and Orvig, 1970), compared to that of the open ocean (10% to 15%) minimizes heat absorbed by the surface and results in a sharp contrast in energy flux between ice free and ice covered oceans. This abrupt change in energy exchange can, under appropriate conditions, affect atmospheric circulation and give rise to violent weather systems known as polar lows (Carleton, 1985; Businger and Reed, 1989; Gloersen et al., 1989). Sea ice with its snow cover is also an effective insulator that limits the exchange of energy and momentum between the ocean and atmosphere. For example, in winter, the heat flux in an open lead exceeds by two orders of magnitude the heat flux through an adjacent thick ice cover (Badgley, 1966; Maykut, 1978). A large fraction of world's deep and bottom water is believed to be formed at polar latitudes (Stommel, 1962; Gordon, 1978; Killworth, 1983). Coastal polynyas near shelves around the Antarctic continent have been noted as ice factories and principal sources of bottom water (Zwally et al., 1985; Comiso and Gordon, 1998). The cold, dense water formed from sea ice growth in Arctic coastal polynyas helps maintain the Arctic Ocean halocline (Aagaard et al., 1981; Cavalieri and Martin, 1994). This dense water can also induce convection and deepen the mixed layer. Similar phenomenon is observed in the Odden, which is an ice tongue formation in Greenland Sea (Shuchman et al., 1996; Comiso et al., 2001) regarded as one of only four regions where open ocean convection occurs with the direct generation of deep water.

Because of its vast extent, large scale studies of the sea ice cover can be done most effectively through the use of satellite data. The later is available through various frequency channels from visible through infrared to microwave frequencies. Visible and infrared satellite data (e.g., AVHRR) have been used for mesoscale studies but the coverage of sea ice provided by the data is limited because of the persistence of cloud cover in polar regions. Detailed characterization of sea ice under all weather conditions has recently been provided by synthetic aperture radar (SAR) data (e.g., ERS-1, JERS-1, and Radarsat) but only a small fraction of the entire ice cover can be monitored at a time because of operational and data acquisition constraints and a narrow swath width (100 km to 500 km) that limits spatial and temporal resolution. These data sets have nonetheless been useful for regional studies and provide information that have been used to improve the interpretation of other satellite data.

The most comprehensive and consistent source of global sea ice data has been satellite passive microwave sensors (Zwally et al., 1983; Parkinson et al., 1987; Gloersen et al., 1992). Microwave sensors, not limited by weather conditions or light levels, are particularly well suited for monitoring sea ice, because of the strong contrast in thermal microwave emission between areas of ice-free ocean and ice-covered waters. The first passive microwave sensor used extensively for studying the global distribution of sea ice was the Electrically Scanning Microwave Radiometer (ESMR) on board the NASA Nimbus 5 satellite (Gloersen et al., 1974; Zwally et al., 1983). The single channel ESMR, operating at 19.35 GHz, provided daily coverage of the polar regions and allowed for the first time synoptic observations of sea ice concentration needed for undertaking a detailed study of global sea ice variability. The ESMR sea ice algorithm was based on a linear relationship between the radiometric brightness temperatures of ice-free water and consolidated sea ice. Temperature variability effects were reduced using climatological data. At the ESMR frequency the contrast between ice and water is ~100 K. Although the estimated accuracy was only 15% (Comiso and Zwally, 1982), these data were used successfully to document sea ice changes in both hemispheres (Zwally et al.,1983; Parkinson et al., 1987).

The Scanning Multichannel Microwave Radiometer (SMMR) was launched on the SeaSat and Nimbus-7 research satellites in July 1978 and October 1978, respectively (Gloersen and Barath, 1977). With its multichannel capability, SMMR provided more information about the ice cover than ESMR. Multichannel SMMR algorithms extended the calculation of ice concentration to include the discrimination of two ice types, first-year and multiyear in the Arctic (Svendsen et al., 1983; Cavalieri et al., 1984; Swift et al., 1985) and sea ice temperature (Gloersen et al., 1992). Errors in the retrieval of multiyear ice concentration are, however, reported to be large (Kwok et al., 1996) because of the large variability in the emissivity of multiyear ice. A multichannel SMMR algorithm to obtain sea ice concentration only was also developed (Comiso and Sullivan, 1986; Comiso, 1986). The various algorithms take advantage of two or more channels to reduce errors associated with physical temperature variability, emissivity anomalies, and weather effects. In 1987, the first in a new series of passive microwave radiometers was launched as part of the Defense Meteorological Satellite Program (DMSP). This sensor, called the Special Sensor Microwave/Imager (SSM/I), operates at frequencies ranging from 19.4 GHz to 85.5 GHz. The SSM/I measures both horizontally and vertically polarized components at all frequencies except at 22.2 GHz for which only a vertically polarized component is obtained.

The advent of the Advanced Microwave Scanning Radiometer (AMSR) sensor, will mark a significant improvement in the capability for monitoring the sea ice cover. The new sensor will be basically a combination of both SMMR and SSM/I systems but with much better resolution. This means improvements in the ability to remove ambiguities in sea ice concentration through the use of the 6 and 10 GHz channels which have much better contrast in the signature of sea ice and open water than SSM/I channels. These channels also allow for the determination of ice temperature, which is an important polar parameter, and can be used to minimize uncertainties in the derived ice parameters that are associated with the spatial variability of ice temperatures. The high resolution data provided by the 85 GHz will also be useful in discriminating different surface types that may be associated with different emissivities.

2. Scientific Objectives

The specific objectives of this document are (a) to provide the theoretical basis of the algorithm that will be used to generate sea ice data sets from AMSR brightness temperatures; (b) to assess the accuracy of these products; and (c) to evaluate the range of applicability and the limitations of the derived data. Although passive microwave satellite data have been around for a while, AMSR will be a new high performing instrument that requires algorithms designed to take advantage of its added capabilities. AMSR data are expected to provide the baseline for new polar climate data sets and the means to evaluate the quality and consistency of historical satellite data. High quality and consistently derived sea ice parameters are needed to ensure that the time series data are suitable for climate change research (e.g., trend and mass balance studies).

Accurate and consistent data on sea ice cover are needed to fulfill some of the scientific goals of NASDA's ADEOS-II project. Among the objectives is to acquire data sets needed for climate change studies and meteorology research. More specifically for the polar regions is to study processes associated with sea ice, to improve and verify global circulation models (GCM), and to gain insights into the changing global climate as reflected in the polar regions. For process studies, it is important to detect and quantify the small but physically significant changes in the physical characteristics of the ice cover, especially in polynya and divergence areas and in the marginal ice zones. Accurate quantification of these polynyas and divergence areas are important in that they are the primary source of global bottom water (Gordon and Comiso, 1988; Martin et al., 1992). There should also be a good match of the sea ice cover as observed by satellites with those derived from GCMs. This will ensure that the physical and mathematical formulation of these models as well as the assumptions made are based on solid foundations. Furthermore, studies of the changing ice cover and its future requires high standards in the quality and accuracy of retrieved satellite data (Bjorgo et al., 1997; Cavalieri et al., 1999; Comiso and Steffen, 2001). A fully validated algorithm for generating such a data set will go a long way towards fulfilling this goal.

3. AMSR Instrument Characteristics

The AMSR is a fourteen channel, eight-frequency total power passive microwave radiometer system that will be launched aboard the ADEOS-II satellite in 2002. It measures vertically and horizontally polarized radiances at 6.925, 10.65, 18.7, 23.8, 36.5, 50.3, 52.8, and 89.0 GHz. A second instrument, called AMSR-E, is a slightly modified version which will be launched on board EOS-Aqua satellite also in 2000. The ADEOS-II is a morning satellite while the EOS-Aqua is an afternoon satellite. Data from the two systems thus complement each other and will all be acquired and processed by NASDA's Earth Observation Center. AMSR consists of an offset parabolic reflector 2 m in diameter, fed by an array of seven feedhorns. The AMSR rotates continuously at 40 rpm about an axis parallel to the local spacecraft vertical. At an altitude of 802.9 km, it measures the upwelling scene brightness temperatures over an angular sector of + 61° about the sub-satellite track, resulting in a swath width of 1600 km. During a period of 1.5 seconds the spacecraft sub-satellite point travels 10 km. Even though the instantaneous field-of-view (IFOV) for each channel is different, active scene measurements are recorded at equal intervals of 10 km (5 km for the 89 GHz channels) along the scan. The half-cone angle at which the reflector is fixed is 47.4° which results in an Earth incidence angle of 55.0°. Table 1 lists the pertinent performance characteristics

The radiometer calibration error, exclusive of antenna pattern correction effects, is composed of three major contributors: warm load reference error, cold load reference error, radiometer electronics nonlinearities and errors. An estimate of the warm load reference error is ~0.5 K, based on the RSS of the various components. The error in the cold reference measurement is mainly produced by the error in coupling between the cold sky reflector and the feedhorn. This is estimated to be ~0.5 K. The radiometer electronics nonlinearity results in an error that can be estimated during the thermal vacuum calibration testing (on SSM/I this error is ~0.4 K). A source of error in the receiver electronics is the gain drift resulting from temperature variations over one orbit. This error depends on the design of the receiver and overall design of the sensor. The gain drift can be as much as ~0.24 K for a temperature variation of less than 10 K over one orbit. Accounting for all errors, the total sensor bias error is 0.66 K at 100 K increasing with temperature to 0.68 K at 250 K.

Table 1. ADEOS AMSR SENSOR PERFORMANCE CHARACTERISTICS

CHARACTERISTICS	CENTER FREQUENCIES (GHz)							
	6.9	10.7	18.7	23.8	36.5	89.0	50.3	52.8
BANDWIDTH (MHz)	350	100	200	400	1000	3000	200	400
SENSITIVITY (K)	0.3	0.6	0.6	0.6	0.6	1.1		
IFOV (km x km)	76x44	49x28	28x16	31x18	14x8	6x4	12x8	12x8
SAMPLING RATE (km x km)	10x10	10x10	10x10	10x10	10x10	5x5		
INTEGRATION TIME (ms)	2.6	2.6	2.6	2.6	2.6	1.3		
BEAM EFFICIENCY (%)	95.3	95.0	96.3	96.4	95.3	96.0		
BEAMWIDTH (degrees)	2.2	1.4	0.8	0.9	0.4	0.18		

4. Standard and Research Products

The standard product for sea ice is sea ice concentration which is deemed essential to meet the overall scientific objectives of the ADEOS program. Ice temperature is also derived by the same algorithm and will be generated as a research product (Table 2). These products will be mapped to a standard polar grid currently used for the SSM/I (NSIDC, 1992). The grid resolutions for the AMSR brightness temperatures and sea ice concentrations were selected to take advantage of the full spatial resolution of the AMSR, while still providing continuity with similar data from SMMR and SSM/I. Accuracies of the derived sea ice data will be determined with the aid of a comprehensive validation program described in section 5. In addition to the sea ice parameters, gridded brightness temperatures will also be provided at grid resolutions commensurate with the Level 2A spatially-averaged data (Table 2). Note that the 6.9 and 10.7 GHz data are gridded at a finer resolution than actual resolutions of about 58 and 37 km, respectively. The reason is to be able to use these channels in combination with higher frequency channels without losing too much on the resolution in the latter which are the primary channels for the algorithm. Further justification for using this gridding procedure will be presented later. It should be pointed out the sampling rate is 10x10 km for the 6.9GHz to 36.5 GHz channels and is 5x5 km for the 89 GHz channels. Also, observations at 6.9 and 10.7 GHz are produced at a spatial interval of approximately 20-km and at the sensor sampling rate for the other frequencies. Level 2A brightness temperature data will be convolved using the Backus-Gilbert method to provide the spatial averaging that is especially useful in the gridding the 6.9 and 10.7 GHz data at a finer resolution than actual resolution.

Table 2. AMSR Level 3 Tb and Sea Ice Data Sets

PARAMETER	APPROX. RESOL.	GRID RESOL. SIZE	TEMPORAL FOOTPRINT
6.9	58 km	25.0 km	
10.7	37 km	25.0 km	Daily Ascend., Decend., & Combined
18.7	21 km	25.0, 12.5 km	Daily Ascend., Decend., & Combined
23.8	21 km	25.0, 12.5 km	Daily Ascend., Decend., & Combined
36.5	11 km	25.0, 12.5 km	Daily Ascend., Decend., & Combined
89.0	5 km	25.0, 12.5, 6.25 km	Daily Ascend., Decend., & Combined
Sea Ice Conc.		25.0, 12.5 km	Daily Ascend., Decend., & Combined
Sea Ice Temp.		25.0 km	Daily Ascend., Decend., & Combined

Sea ice concentration has been the parameter that is produced routinely from satellite passive microwave data for both global change research and operational requirements. It is the parameter that is used to quantify the extent of sea ice cover, the location of ice edges, the area of open water within leads and polynyas in the ice pack, and the amount of ice that survives the melt season. It is, however, a quantity that is difficult to define because of the ever changing nature, and therefore signature, of the ice cover. For example, as ice evolves from open water through grease ice, nilas, young ice and then thick first year ice with snow cover, the emissivity of the surface also changes constantly from that of open water to that of thick first year ice cover. Thus, in areas of predominantly new ice cover, the retrieved ice concentration can be less that those of thick ice cover, even if the fraction of true open water in both regions are the same. The change is similar to that of the reflectivity of the surface as observed in visible channel data and provide the means to identify areas of interest such as those of polynyas and divergence regions.

Ice temperature, which is a research product, is of great importance for polar studies especially in energy balance calculations. Direct measurement of ice surface temperature is particularly valuable for sea ice cover prediction models (Preller et al., 1992). When combined with ice concentration measurements, ice temperature data would considerably reduce current uncertainties in the estimates of polar energy budgets. The monitoring of long-term changes in ice temperature may also provide valuable information about changes in the thickness of the ice and its snow cover. While AVHRR ice surface temperature algorithms have been developed (e.g., Schluessel and Grassl, 1990; Yamanouchi and Seko, 1992; Comiso, 2000), spatial and temporal coverage is limited by the presence of clouds as noted earlier. On the other hand, passive microwave would provide continuous coverage at good spatial and temporal resolution. It should be pointed out that the parameter retrieved from AMSR represents the snow/ice interface temperature in the seasonal regions and the average temperature of the freeboard layer of the ice in the perennial ice regions.

5.0 Algorithm Description and Theoretical Basis

The basic radiative transfer equation that applies to the brightness temperature, (T_B) observed by satellites at a given wavelength is

$$T_B = \varepsilon T_S e^{-\tau} + \int_0^{\tau} T(z)\, \zeta(z)\, e^{-\tau+\tau'(z)}\, d\tau'(z) + (1-\varepsilon)\kappa e^{-\tau} \int_0^{\tau} T(z)\, \zeta(z)\, e^{-\tau'(z)}\, d\tau'(z) \qquad (1)$$

where ε is the emissivity of the surface, T_S is the physical temperature of the surface, $\tau'(z)$ and τ are the atmospheric opacities from the surface to a height z and from the surface to the satellite height, respectively, κ is an estimate of the diffusiveness of the surface reflection, and $\zeta(z)$ is the emittance at z. In equation (1), the first term represents radiation directly from the earth's surface which is the dominant contribution. The second term represents satellite observed radiation directly from the atmosphere, while the third term represents downwelling radiation from the atmosphere but reflected from the surface of the earth. A fourth term that takes into account the reflected contribution of radiation from free space, which is a negligible additive contribution, is not included in equation (1).

Within the ice pack, the radiation observed by the passive microwave satellite sensor comes from ice covered surface, open water, or a combination of both. The observed brightness temperature, T_B, is expressed in terms of the relative contribution from each surface by a linear mixing formulation given by

$$T_B = T_O C_O + T_I C_I \qquad (2)$$

where T_O and T_I are the brightness temperatures of ice-free ocean and sea ice, respectively. C_O and C_I are the corresponding fractions of each of the two ocean surface components within the field-of-view of the instrument and add to unity (e.g., $C_O = 1-C_I$). Equation (2) forms the basis for sea ice concentration algorithms. The challenge is how to take into account temporal and spatial changes in T_O and T_I which are both functions of emissivity (ε), temperature (T_S), and atmospheric opacities (τ, and τ'), as indicated in equation (1). Such changes can be taken into account or at least minimized through the utilization of several AMSR channels as will be described below.

5.1 Basic Bootstrap Algorithm

Passive microwave data have been especially useful for sea ice studies because of the relatively high contrast in the emissivity of open water and sea ice (Zwally et al., 1983). The contrast is frequency dependent and is higher with the low frequency channels than with the high frequency channels. Thus, if resolution is not an issue, the 6.9 GHz data from AMSR would be best suited for ice retrievals since it provides the best contrast between ice and open water. The radiation at this frequency is also less vulnerable to atmospheric and surface effects than that of the other channels making the frequency channel especially useful for retrieving ice temperatures. The additional use of the 10.7 GHz data is also promising because of better resolution than the 6.9 GHz data and may be utilized to improve the accuracy of the ice concentration retrievals.

Assuming a linear relationship between the brightness temperature and the fraction of ice cover, as in equation (2), the ice concentration, C_I, corresponding to an observed brightness temperature, T_B, over a sea ice covered region can be derived from the equation

$$C_I = (T_B - T_O)/(T_I - T_O). \qquad (3)$$

T_O, T_I, and T_B all include contributions from the intervening atmosphere, as described in Zwally et al. (1983). T_I varies spatially mainly because of spatial changes in the emissivity and temperature of the ice, while T_O is approximately constant for open water surfaces within the ice pack. Thus, the success of an ice concentration algorithm depends on how accurately the value of T_I is determined. Equation (3) can be used without correcting each data element for atmospheric effects as long as the atmospheric opacity is relatively uniform spatially for the set of frequency channels that are used in the algorithm. At the frequencies utilized, any advantage provided by an atmospheric correction through a radiative transfer model is usually negated by errors in the model due to the paucity of radiosonde atmospheric data. As will be shown later, the impact of the variability of atmospheric effects on the accuracy of derived sea ice parameters appears to be negligible.

The Basic Bootstrap Algorithm (BBA) is based on the original Bootstrap Algorithm that is currently used for processing SMMR and SSM/I data (Comiso, 1986; Comiso, 1995; Comiso et al., 1997) in which T_I and T_O in equation (3) are determined through the use of multichannel data. Data from three sets of channels have been found to be especially useful: (a) 19 GHz and 37 GHz brightness temperatures, both vertically polarized (called V1937); (b) vertically and horizontally polarized 37 GHz brightness temperatures (called HV37); and (c) 19 GHz and 37 GHz brightness temperatures, both horizontally polarized (called H1937). Scatter plots in 2-dimensional space using the HV37 and V1937 combinations are shown in Figures 1a and 1b, respectively. The data points were collected by a set of P3a aircraft radiometers flown over nearly 100% ice cover in the Arctic in May 1987 (Comiso et al., 1991). In both plots, the data points are mostly along the line AD and form a compact and elongated cluster of points similar in characteristics to those of satellite data (Comiso, 1986). The linearity of the data points along AD is the key information that is utilized by the Bootstrap Algorithm to identify the proper value of T_I in equation (3). In the scatter plot shown in Figure 1a, data points of open water within the pack would fall near the location labeled O. Thus, for an observation corresponding to any data point, B, in this 2-D space, T_I is a data point along the line AD and its value is inferred from the intercept of the lines AD and OB. Ice concentration is determined basically from an equivalent form of equation (3), which in this case is the ratio of OB to OI, as described in Comiso (1995). The complete formulation is given in Comiso (1995) and explicitly in the next section but with brightness temperature data replaced by emissivity data. The existence of consolidated ice clusters such as those along AD in Figure 1 have been confirmed by ship radiometer data over the Antarctic (Comiso et al., 1989; Grenfell et al., 1994) and over locally grown sea ice at CRREL (Grenfell and Comiso, 1986). The variability of the data points across the consolidated ice cluster defined by the line AD in the similar scatter plots that make use of satellite data is a measure of the variability of T_I and includes temperature, emissivity, and atmospheric effects.

In the Arctic, a combined used of the HV37 and V1937 sets is desirable because of spatial inhomogeneity and complexity in the physical characteristics of the ice cover (Comiso, 1986). The use of the HV37 set is especially advantageous in the perennial ice region in winter, because the slope of data points in this set is close to unity and hence the temperature effects are minimal. Also, the standard deviation of data points about the line AD is close to 2K which is equivalent to 2.5% error in the estimates of ice concentration. This reflects how well sea ice concentration can be derived in the region. The V1937 set is a good complement of the HV37 set and has the advantage that it uses vertical channel data only which are observed to be less affected by layering and inhomogeneities in the ice (Matzler, 1984; Grenfell et al., 1994) than the horizontal channels. This set has been found to be especially suitable in seasonal sea ice regions as in the peripheral seas of the Arctic and most part of the Antarctic (Comiso et al., 1984; Comiso and Sullivan, 1986) where snow cover is known to have layering and a very complex texture (Massom et al., 1998; Worby and Massom 1995).

Although the V1937 set is more sensitive to fluctuations in ice temperature than the HV37 set (Comiso, 1995), the spatial variations in surface ice temperature (i.e., snow ice interface temperature), as observed from limited data in the Antarctic, has been observed to be relatively small and have a standard deviation of about 2K. Sensitivity studies and analysis of the distribution of the consolidated ice cluster indicate that the error from temperature effects is indeed small compared to other sources of error. In the Antarctic, the HV37 set is not as useful as in the Arctic because consolidated ice data in this set are close to or almost along the line OA. The use of this set would lead to the retrieval of erroneously large fraction of open water in some consolidated ice regions. The V1937 set has thus been the primary set used to retrieve ice concentrations from SMMR and SSM/I data. Recent studies, however, indicate that the accuracy of the retrieved product in the Antarctic can be further improved with the use of a formulation similar to that of the Arctic but with the H1937 set used instead of the HV37 set. The additional use of the H1937 set has been observed to be especially useful in young ice regions and enables a better characterization of the sea ice cover near coastal and polynya areas. The use of the latter is a new and is currently part of the Basic Bootstrap Algorithm.

Typical monthly sea ice concentration maps derived using BBA for the Northern and Southern Hemispheres during summer and winter are shown in Figure 2. The large seasonal change in the extent of the ice cover in both hemispheres are apparent. Also apparent are relatively lower concentrations than average along coastlines, which are sites of coastal polynyas, near islands and big icebergs, and along the ice edges. These regions are sites of open water and new ice. The maps thus represent what is generally expected as ice distributions in both hemispheres.

5.2 The AMSR Bootstrap Algorithm

The AMSR algorithm for sea ice is a modified version of the Basic Bootstrap Algorithm and is called the AMSR Bootstrap Algorithm (ABA). The modified version will provide the means to estimate surface ice temperature and at the same time use the latter to further reduce errors in the determination of ice concentration. In particular, it makes use of 6.9 GHz data to reduce if not eliminate temperature effects when the V1937 and H1937 data sets are utilized. The algorithm has been successfully tested using SMMR data which have the basic channels required. However, some adjustments would be needed after launch when real AMSR data becomes available since SMMR is known to have problems with calibration and the resolution of the 6 GHz channels is coarse at 150 km, compared to 58 km for AMSR.

The schematic of the procedure for estimating of ice concentration and ice temperature, is shown in Figure 3. The technique which was reported in Comiso and Zwally (1997) is similar to that of the Basic Bootstrap Algorithm, as described in Comiso (1995), with T_B replaced by ε, the latter basically independent of temperature fluctuations. The effective emissivity of the surface within each data element can be estimated from

$$\varepsilon_B = \varepsilon_I C_I + \varepsilon_O (1-C_I) \qquad (4)$$

where C_I is initially obtained from equation (3) through the use of a combination of 6 and 37 GHz channels at vertical polarization, while ε_I and ε_0 are emissivities of ice and open water, respectively, which can be derived from histograms of data within the pack and assumed constant. Unlike equation (2), equation (4) is not the exact formulation for the observed satellite data but sensitivity studies indicate that the associated error is very small (<1%) and is highest when the concentration is 50%. The physical temperature of the ice surface within each data element is then given by

$$Tp = T_B(6V)/\varepsilon_B(6V) \qquad (5)$$

where $T_B(6V)$ is the observed brightness temperature of the surface at 6 GHz (vertical polarization). The emissivity of the surface at 19 and 37 GHz can then be derived from

$$\varepsilon_B(19V) = T_B(19V)/Tp \qquad (6)$$

$$\varepsilon_B(19H) = T_B(19H)/Tp \qquad (7)$$

$$\varepsilon_B(37V) = T_B(37V)/Tp \qquad (8)$$

and

$$\varepsilon_B(37H) = T_B(37H)/Tp \qquad (9)$$

with the assumption that the temperature of the layer of ice from which radiation emanates is approximately frequency independent between 6 and 37 GHz and is equal to Tp. The use of emissivity instead of brightness temperature for estimating ice concentration is justified by the matching of reference data points of both consolidated ice (100% IC) and open water (0% IC) as discussed in Comiso and Zwally (1997). As in Comiso (1995) which makes use of brightness temperatures, the tie points for a datapoint at B are represented by the intercept points ($\varepsilon_{1I},\varepsilon_{2I}$) along the 100% ice line AD which are calculated using the equations

$$\varepsilon_{1I} = (\varepsilon_{1A} - \varepsilon_{1O} - \varepsilon_{A2} S_{AD} + \varepsilon_{2O} S_{OB})S_{OB}/(S_{OB} - S_{AD}) + \varepsilon_{1O} - S_{OB}\varepsilon_{2O} \qquad (10)$$

$$\varepsilon_{2I} = (\varepsilon_{1A} - \varepsilon_{1O} - \varepsilon_{2A} S_{AD} + \varepsilon_{2O} S_{OB})/(S_{OB} - S_{AD}) \qquad (11)$$

where S_{AD} and S_{OB} are slopes of the lines AD and OB, respectively, (ε_{1A}, ε_{2A}) represents any point along the line AD, and (ε_{1O}, ε_{2O}) represents the open water reference emissivity. The ice concentration for the data point at B is derived from the ratio of the distances OB and OI (see Figure 1) and given by the equation

$$C = [\{(\varepsilon_{1B} - \varepsilon_{1O})^2 + (\varepsilon_{2B} - \varepsilon_{2O})^2\}/\{(\varepsilon_{2I} - \varepsilon_{2O})^2 + (\varepsilon_{1I} - \varepsilon_{1O})^2\}]^{1/2} \qquad (12)$$

In the formulation, it is convenient to choose $\varepsilon_{2A} = 0$ at point A along AD with ε_{1A} the resulting offset. Additional details, including the assumptions in the determination of the line AD and the point O, are discussed in Comiso (1995). Since the initial calculation of the emissivity at 6.9 GHz makes use of ice concentration that has not been temperature corrected, the emissivity is recalculated using the more accurate result from equation (12) and a second iteration follows, starting with equation (4) as indicated in Figure 2, to obtain the final ice concentration estimate. Also, the final value of Tp is then used to calculate the average physical temperature of ice surfaces in each data element, T_S, using the equation

$$T_S = [T_P - T_O(1-C_I)]/C_I. \qquad (13)$$

To illustrate the effectiveness of ABA, we make use of SSM/I data in conjunction with skin surface temperatures derived from AVHRR data (Comiso, 2000) since the former do not have a 6.9 GHz channel. Figures 4a-4d show examples of skin surface temperature maps for a summer (March) and a winter (September) month in 1992 in both hemispheres. The images show temperature distributions over the open water, sea ice, and the continent and illustrate how surface temperature changes spatially at various latitudes. As expected, the coldest temperatures are located in the continent while intermediate but still subfreezing temperatures are over sea ice with the temperatures increasing progressively towards the north. Areas of polynya formation are usually warmer than adjacent regions. These temperature data are then converted to snow/ice temperature data, that would represent T_P in the above formulation, using regression parameters derived by Comiso et al. (1989) using data in the Antarctic region.

To illustrate the difference between the use of brightness temperatures alone compared with the use of emissivity, Figures 5 show scatter plots using the HV37 and V1937 sets for both variables in the Arctic region during winter. The distributions for brightness temperatures are shown to be very similar to those of emissivities. The cluster along the consolidated ice (AD) are also shown tobe equally compact. Although there are large spatial variations in surface temperature as indicated in Figure 4, the net effect on the distribution of the data points in the HV37 and V1937 sets appears to be small.

In the consolidated ice regions, the data points are apparently redistributed such that the net variability about the cluster AD in the emissivity plots is essentially the same as in the brightness temperature plots. This implies very similar errors for both systems. Similar plots are shown in Figure 6 for the Antarctic. Again the brightness temperature plots are very similar to those of the emissivity plots.

Ice concentrations were derived using T_P from AVHRR and ABA for the same summer and winter months of 1992 (as in Figure 2) and the results are presented in Figures 7a-7d. The maps for each season look very similar with the areas of high ice concentrations and reduced concentrations confined in the same general locations. The ice concentration maps for September 1992 in the Antarctic have been shown to be consistent with Landsat and OLS satellite observations (Comiso and Steffen, 2001), and with the expected behavior of the ice cover in coastal and some deep ocean regions (e.g., near the Maud Rise and the Cosmonaut Sea) where polynyas have been observed. Difference maps between the BBA and ABA ice concentrations for each season are shown in Figures 8a-8d. Generally, the two maps are basically identical within errors. Relatively higher concentrations (by less than 4%) are observed with the ABA in the Central Arctic and near the continent in the Antarctic region where the difference are likely due to much colder temperatures than average. It is interesting to note, however, that alternating positive and negative differences are observed around the periphery of the Antarctic ice cover. This is coherent with the effect of the Antarctic Circumpolar Wave (ACW) as described by White and Peterson (1996) in which alternating high and low temperature anomalies are observed. The advantage with ABA, is that it enables the retrieval of surface ice temperatures, and has the potential of obtaining more accurate retrievals in coastal polynyas and in regions where the surface ice temperatures are abnormally cold. The difference from the two retrievals may be small but for some regions, like polynya regions, the impact may be significant.

Since low frequency channels are not available in the SSM/I system, ABA was also developed and tested using Nimbus-7 SMMR data. The SMMR system, which has a 6.6 GHz channel, provided the means to put together a working version of ABA that has the right input parameters. However, the effectiveness of ABA, especially in retrieving ice temperatures, could not be fully tested because of very large footprints for SMMR and instrumental problems associated with polarization mixing. This made it difficult to evaluate discrepancies between BBA and

ABA results. The advent of AMSR data and the validation program will provide the means to test and refine the program and validate the results.

5.3 Masking Algorithms

Since the polar maps include land areas, a land mask is used to ensure that the algorithm is applied on data in the ocean regions only. Previous versions of such land mask have been based on existing maps put together through collaborative efforts of many agencies and foreign countries but the accuracy in some areas have been questionable because of the lack of direct measurements in these areas. Such mask has been updated using data from a dedicated RADARSAT mission in the Antarctic in 1998. Significant differences between the old and the new maps are apparent, reflecting some errors in the previous data and a constantly changing continental boundary due to surges and iceberg calving. The comparison indicates that surges at the Ross Ice Shelf and Ronne Ice Shelf have been going on in the last few decades. If the previous land mask currently used for SSM/I data is used on recent data, it would produce erroneous coastal polynyas of about 50 km wide. It is apparent that the location of the continental margin is not constant and that regular updates in the land mask for sea ice retrievals is needed.

At the ice-free land/ocean boundaries, there are also erroneous ice concentrations in the ocean part adjacent to land because the brightness temperatures are similar to those of ice covered regions. To illustrate this problem, an ice concentration map in the Ross Sea region is shown in Figure 9a during the summer when the Ross Sea Ice Shelf boundary has a minimum of sea ice. Along the continental boundary, significant ice cover is retrieved by the algorithm. The result for applying an algorithm developed by Cho et al. (1996) is shown in Figure 9b. The technique uses a running 3 by 3 matrix with the middle pixel in consideration. If there is a land pixel in the matrix, the middle pixel value is replaced by the minimum value within the 3 by 3 matrix. The technique is effective in removing some of the pixels with non-zero ice concentration in the north and western side but overall, improvements appeared to be needed. An improved version of this technique is currently used for the Bootstrap algorithm and when applied, the result is shown in Figure 9c. This later technique which searches one or two pixels further to find open water generally better results than the Cho et al. technique, as indicated, but at the front of the ice shelf, there is still significant ice. Generally, it works better in other regions but for this particular case, it did not work very well because of aforementioned problem with the land/ocean mask. The ice covered area in front of the shelf is more than should be the case because the actual front of the shelf is further north than indicated by the land mask (white). The latter technique is more effective when there is less contamination along the coastline, as is usually the case, and also when AVHRR climatological temperature data are used to mask out areas in relatively warmer oceans.

The retrieved ice concentrations also show erroneous data in areas of open ocean where the signature is similar to those of ice covered ocean. This usually happen in areas of abnormal weather and/or wind conditions. A masking technique to automatically eliminate such bad data in the open ocean has been developed,as described in Comiso (1995), but such technique is not 100% efficient, especially with SSM/I because the lowest channel is close to the water vapor line. The use of the AVHRR climatological data in conjunction with the ocean masking technique provide significant improvements but not near the sea ice margin. The use of low frequency AMSR data, which are less sensitive to weather effects (e.g., 6.9 and 10.7 GHz) and show better contrast between sea ice and open water are expected to significantly reduce errors in the marginal ice region.

5.4 Error Analysis and Sensitivity Studies

The physical basis of and assumptions in the Bootstrap algorithm have been confirmed using ship based radiometer experiments in the Antarctic (Comiso et al., 1989; Grenfell et al., 1994), an aircraft experiment in the Arctic (Comiso et al., 1991) and a controlled sea ice experiments at the Cold Regions Research Laboratory (Grenfell and Comiso 1986). Comparative studies of ice concentrations derived from SSM/I using the Bootstrap Algorithm with those derived from aircraft, SAR, Landsat, and helicopter data have indicated consistencies within an average of 5 to 15% in winter and 10 to 20% in the summer (Comiso et al., 1984; Comiso, 1986; Comiso et al., 1991; Comiso and Kwok, 1996; Comiso and Steffens, 2001). Good validation data sets for much of the Antarctic region, however, have been difficult to come by and hence the need for a coordinated aircraft and in situ validation program in the region, especially for a new and more versatile system like AMSR.

Errors associated with the estimate of ice concentration are caused primarily by spatial and temporal changes in surface temperatures, emissivity, and atmospheric opacity. Other sources of errors include the retrieval of erroneous ice concentrations in the open ocean and at the land/ocean boundaries as discussed in the previous section. The impact of surface temperature has been examined and discussed previously. It is apparent that the maps generated with BBA and with ABA, provide results that are almost identical within errors. Sensitivity studies for errors due to variations in temperature has also been reported previously (Comiso, 1995; Comiso et al., 1997). Because the snow cover is such a good insulating material, the spatial fluctuation of the snow/ice temperature has been found to be relatively small (with σ being about 2.5 K). The Antarctic sea ice cover is very seldom without a snow cover not only because of frequent snow precipitation but also because of drifting snow. However, katabatic and geostropic wind can be persistent in some areas, depleting the snow cover and causing the temperature of the emitting sea ice surface to be abnormally low in some regions of Antarctica. The difference maps in Figure 4 show that in these regions, the average bias due to temperature is about 2 to 4%. This discrepancy is small but if verified to be indeed a bias associated with temperature, the use of ABA provides enhanced ability to characterize more accurately small features of scientific interest, such as coastal polynyas, the sizes of which are sometimes comparatively small.

The large variability in the emissivity of the sea ice cover (Grenfell et al., 1994) is likely the main source of error in the determination of sea ice concentration. The success of the algorithm depends on the ability to establish the right tie-point (T_I) for each data element. Cluster analysis results indicate that most of the data points representing 100% ice cover tend to cluster along the line AD in Figure 1. This information enables the algorithm to account for the large variability in emissivity (and also in temperature and atmospheric opacity). The algorithm assumes that the cluster is approximately linear. Any significant deviation of an ice data point from this linearity and the location of the AD line produces an error. Also, the accuracy in the retrieval depends on the compactness of this cluster along the line AD.

In the Arctic, the distribution of the data points in the HV37 and V1937 sets are shown in Figure 5a and 5b for brightness temperatures and Figures 5c and 5d for emissivities. In the Central Arctic, the data points have a standard deviation of about 2 K about this line for the HV37 set which is the main set used in the region. In the Antarctic, the scatter plots for H1937 and V1937 are shown in Figure 6 and indicate less defined distributions along AD than those in the Arctic. The standard deviation about the cluster line is higher at about 5K for the V1937 set which is previously the only set used in the region. The error in the determination of ice concentration is thus higher in the Antarctic than in the Arctic.

Polarization and gradient ratios have been used in the NASA Team Algorithm to overcome spatial variations in surface ice temperature. The use of this technique, is apparently not so effective in the seasonal ice region, especially in the Antarctic, because of possible differences in the response of the vertically and horizontally polarized radiation to different surface and subsurface conditions within the ice pack can be very different (Markus and Cavalieri, 2000; Comiso and Steffen, 2001). The results is also an indication that variability in emissivity is indeed a much bigger source of error than variability in ice temperatue.

Depending on frequency, the emissivity of first year sea ice can be very different from that of multiyear ice. This is especially the case in the Arctic because of the presence of an extensive perennial ice cover. In the Antarctic, the signature of multiyear ice is more difficult to establish. At the end of the summer, the region with the largest area of sea ice cover is located in the Western Weddell Sea. However, the signature of ice in this perennial ice region is similar to that of most other Antarctic regions (Zwally et al., 1983). The reason for this is that the summer ice is actually advected to the northeast during the subsequent winter following the direction of the Weddell Gyre and causing the ice cover in the Western Weddell region to be eventually replaced by seasonal sea ice during the year. However, in other areas like the Bellingshausen/ Amundsen (B/A) Seas, the signature of ice in the winter is different from those of other regions. This was most apparent in the 1980s when the region was consistently covered by perennial ice during the summer. Unlike the ice cover in the Western Weddell region, the perennial sea ice at B/A are more confined and could remain basically in the same general location for several years and therefore acquires a multiyear ice signature as in the Arctic. To minimize the error in the retrieval of ice concentration in the region, a different tie point for consolidated ice (i.e., different slope and offset for AD) is used to better match the different distribution of ice clusters in the region. Such correction is necessary since otherwise, large areas of the region would be mistaken as a divergence or polynya regions. Since 1989, however, drastic retreats in the summer ice cover was observed (Jacobs and Comiso, 1994), due to a possible change in the climate of the region (King and Harangozo, 1998). In 1989 and later dates, it became evident that the signature of ice in the B/A region is more and more similar to those of the rest of the Antarctic region likely because of gradual disappearance of thick multiyear ice cover. While not a serious problem at present, AMSR data will be examined for changes in the ice distribution patterns that may cause multiyear ice signatures in some areas to reappear again.

The signature of sea ice in the spring and summer also becomes very different from that of autumn and winter. This happens as a result of wetness in the snow cover due to above freezing temperatures during the period. When the snow cover has about 3% liquid water, as in early spring, the dielectric property of the surface becomes very high and the snow surface becomes opaque. The resulting emissivity of the surface approaches that of a blackbody and the observed brightness temperature of sea ice at all frequencies increases considerably. As spring progresses, the snow gets melted and the surface of the ice is covered by slush or liquid causing an effect that is opposite to that of early spring. The emissivity of ice during this period is thus not as well defined as during the winter period. Errors in the retrieval of ice concentration are therefore larger and adjustments in the tie points are desired to account for the changing character of the surface and to optimize accuracy.

The ocean mask can also be a source of error if it does not provide consistent lower threshold for ice concentration. This threshold is established for some average conditions but algorithms for the ocean mask may not be able to adjust to big fluctuations in weather and wind conditions. At some low concentration levels, it is difficult to discriminate between sea ice covered area and open water because the brightness temperatures for these two types of surfaces are almost identical. The lowest (threshold) ice concentration in which discrimination is possible is what normally defines the ice edge location. For SSM/I, the discrimination is done through the use of a cut-off in the V1937 and V1922 sets, as described in Comiso (1995). While this may improve with AMSR data, the threshold concentration currently used is approximately 10% but for better consistency, a 15% cutoff is usually used for long term ice extent studies. The cut-off technique is basically effective, as illustrated in the comparison of an ice concentration map derived using the Bootstrap algorithm and a SAR image for the region indicated by a rectangular box in the ice concentration map (Figure 10a). Features at the ice edge shown by the high-resolution SAR image are basically reproduced in the passive microwave image. The open water features within the ice pack are also coherent in the two images if the changing SAR backscatter for open water within the ice pack is taken into account. It is also apparent in Figure 10b that the character of the ice cover changes significantly from the marginal ice zone, where loosely connected pancakes, new ice, and ice bands are located, to the inner zone, where thicker and more consolidated ice are found.

A more quantitative characterization of the ice edge by satellite data is depicted in the plots in Figure 11. The plots in Figures 11a and 11b represent brightness temperatures at 6 SSM/I channels along a transect at approximately 148 ^{o}E longitude from open water through the marginal ice zone and into the pack. As indicated, the brightness temperature increases with latitude at all frequencies except at 85 GHz (vertical polarization) in the marginal ice zone. The approximate location of the ice edge along this particular transect has been provided through direct observations from the Australian ship, R.V. Aurora Borealis, and is represented by the vertical dash line. The ice concentrations derived from the Bootstrap and Team algorithms are indicated in Figure 11c and shown to increase with brightness temperatures and have values of about 25% at the ship observed ice edge. Ship observations are usually dependable but difficult to interpret in terms of large scale characteristics in the ice cover because of limited field of view. Complications in the observation of the ice edge can be seen in the SAR image (Figure 10b) in which ice bands form and grease ice can form several kilometers beyond (to the north of) the ice bands.

While the specific case shown in Figure 11 indicates good agreement, some other cases, reported in Worby and Comiso (2001), show large discrepancies. Sometimes, the ice edge identified from ship is several km to the north of the SSM/I ice edge. This is especially the case in spring and summer, when ice floes breaks up and the surface of the ice is covered by liquid. Also, sometimes the opposite is true, and this is usually the case when the ship misses some ice fronts to the north, as in the SAR image. Furthermore, the ice edge location, as identified by the Bootstrap algorithm, is sometimes several km to the north of that identified by the Team algorithm. For long term time series studies, consistency in the determination of ice extent is important and this can happen only if the ice edge is identified in a consistent manner for each season and independent of weather, and satellite sensor.

Errors associated with the spatial and temporal variability in the opacity of the atmosphere are expected to be small at microwave frequencies used by the algorithm and are often neglected [*Comiso and Zwally,* 1982; *Massom,* 1991]. However, some sensitivity studies using a radiative transfer model have indicated that such errors can be as large as 10% when the Team Algorithm is used [*Oelke,* 1997]. Not knowing how accurately the models represent actual conditions and what the effect is on the Bootstrap algorithm, actual data are used to investigate the impact of the passage of a low pressure system in the Ross Sea region on derived daily ice concentrations. Figures 12a and 12b show ECMWF mean surface pressure maps and synoptic winds during two periods (June 13 and June 20) when there were large changes in the pressure fields. Figures 12c and 12d are scatter plots of 19 GHz(V) versus 37 GHz(V) data in the region shown in the other images while Figures 12e and 12f show corresponding ice concentration maps. Comparing ice concentrations in the rectangular box shown in the images, which includes the low pressure field in June 20th, the Bootstrap algorithm yielded an average ice concentration of 97% with a standard deviation of 2.7% on June 13 and an average ice concentration of 98% with a standard deviation of 2.1% on June 20. For comparison, the Team algorithm yielded an average ice concentration of 90% with a standard deviation of 5.5% on June 13 and an average ice concentration of 86% with a standard deviation of 3.4% on June 20. These results indicate that the impact of the passage of a low pressure system on the daily ice concentration in relatively consolidated ice regions was relatively minor, especially for the Bootstrap algorithm. In the scatter plots, data points within the rectangular study area are shown as red and it is apparent that the occurrence of the low pressure system caused the brightness temperatures to increase slightly (suggesting enhanced emission in the atmosphere) but proportionately at the 19 and 37 GHz channels. The ice concentrations did not change much because the increases caused the data points to shift along the line AD, which correspond to the tie points for consolidated ice in the Bootstrap Algorithm. It should be noted that winds were relatively steady during the two periods in the study area but a much stronger change occurred at the Ross Sea shelf region (at about 77^o S, 180^o E) likely causing the observed reductions in concentrations in the region from June 13 to June 20. A seven-day separation was chosen to ensure that atmospheric conditions over the pack ice were different. A similar study with 3-day separation (June 17 and 20) yielded very similar results.

5.5. Validation Issues and Validation Program

The validation criterion is that the derived AMSR-E sea ice products agree on average with the corresponding validation data set to within the estimated accuracy of the validation data set. The validation data sets will be derived from any or a combination of field, aircraft, submarine and high-resolution visible and infrared satellite data and are expected to provide a more accurate measure of the standard sea ice products than the AMSR retrieved products. The underlying philosophy of this approach is that confidence in the sea ice products derived from the AMSR will be achieved by showing consistency of such products with independently derived data that are spatially and almost temporally coincident (Comiso and Sullivan, 1986; Cavalieri, 1991; Cavalieri et al., 1991; Steffen and Schweiger, 1991; Grenfell et al., 1994). Operating within this paradigm, the following is a summary of validation methods for each of the AMSR standard products.

The cornerstone of the validation program is the acquisition of a comprehensive data set after the launch of ADEOS-II and EOS-Aqua satellites. The data set will consist primarily of concurrent aircraft, in situ, and satellite data to be collected during the winter 2003 and spring 2004 periods in both hemispheres. One such dedicated program is the Antarctic AMSR Validation Program sponsored by NASA. A P-3 aircraft equipped with a scanning microwave radiometer which has all AMSR frequencies, an infrared radiometer, a laser altimeter and a snow radar will be used on a mission based in Punta Arenas, Chile in August 2003. A sample track for the aircraft over ice covered ocean is shown in Figure 13. Cruises that are expected to provide in situ data during the validation period include those for the US/Nathaniel Palmer, the UK/HMS Endurance, the German/RV Polarstern and other international vessels. Among the polar scientists who had expressed interests in this validation endeavor are Dr. F. Nishio of Japan, Dr. Doug Martinson and Stan Jacob of Lamont Earth Science Observatory, Prof. Koni Steffen of the University of Colorado, Dr. Miles McPhee of the University of Washington, Prof. Ray Smith of the University of California at Santa Barbara, Dr. Peter Wadhams of the University of Cambridge and Dr. Martin Jeffries of the University of Alaska. The validation program will be coordinated with related projects, especially activities of other scientists whose proposals were approved under a general validation program for the ADEOS-II and EOS/AGUA project and under various Announcements of Opportunities in the Earth Science Enterprise Program. The strategy is to take advantage of in situ and other data sets that will be available for this time period. Similar projects will be undertaken with ships of opportunities that will be in the Arctic and Antarctic region during the validation period. Issues and strategies for validating sea ice concentration and ice temperature are discussed below.

Sea Ice Concentration: Sea ice concentration is defined as the areal percentage of sea ice observed within the field of view of the satellite sensor. The primary approach for the validation of retrieved AMSR ice concentrations is to utilized data from the dedicated aircraft campaigns in conjunction with high resolution satellite data, including those from Landsat 7, Terra and Aqua MODIS, NOAA-AVHRR, DMSP-OLS, RADARSAT. The aircraft data will provide the means to assess the absolute accuracy of the retrieval at some places and some seasons while the satellite data provides better spatial and temporal coverage. High-resolution active microwave satellite data such as the Radarsat SAR, are most useful during persistent cloud cover conditions and during darkness. Data from microwave scatterometers, such as those from QuickSCAT, will be utilized for identifying areas of divergence and where significant reductions of ice concentration is expected. However, data from active systems are more difficult to interpret than those from passive and visible systems, because of unpredictable backscatter from different ice types, from open water within the ice pack, and from wind-roughened seas. Such data are valuable but require validation.

Aircraft campaigns are planned for both Arctic and the Antarctic regions and for dry and wet seasons. Such program will provide multi-channel passive microwave data similar to AMSR but at a much better resolution. The high resolution will provide the means to test the effectiveness of the mixing formulation in different ice regimes and conditions. The aircraft will also be equipped with digital and film camera system for the characterization of small features of the ice cover, a laser ranging system for surface topography studies and ice thickness estimates, and a multi-frequency radar for snow cover studies. The strategy is to apply the algorithm on co-registered and coincident aircraft and spacecraft data and evaluate how the results matches each other quantitatively and how they compare with similar analysis from high resolution visible and infrared data. Discrepancies will be analyzed and explained through the use of ancillary data and further examination of the high resolution data. Data at the ice edge, open ocean, and land/ocean boundaries will also be analyzed to validate the effectiveness and consistency of the masking algorithms.

The validation program will take into consideration the large changes in physical and radiative characteristics of sea ice during an ice season. During early ice growth period, the ice cover consists mainly of new ice, pancakes, young ice, and relatively undeformed first year ice. On the other hand, during late winter, the ice cover consists of predominantly thick and vast ice floes with relatively thick snow cover. During the melt season, the vast ice floes get broken up to smaller units and the surface gets covered by slush or liquid. For at least two periods (dry and wet periods) the changes in the radiative signature will be quantified as accurately as possible and relationships with the accuracy of the retrieved sea ice parameters will be evaluated.

As a complementary approach, time series of images will be analyzed to check AMSR retrievals for temporal consistency. The growth and decay of sea ice are limited by physical laws and environmental conditions and such time series data can provide the means to establish how well the expected time development of the ice cover is reproduced by the satellite data. This effort will help identify weaknesses in the technique that are not obvious from examination of individual images.

Atmospheric effects can be estimated using radiative transfer modeling to account for the effects indicated by equation (1). The results from the latter can be used to correct the brightness temperatures observed by the aircraft and satellite and results are used to derive the geophysical parameters that are used in the validation. As indicated earlier, the choice of channel is important and with the set of channels used in the ABA algorithm, the effect appears to be negligible. Further confirmation that this is indeed the case will be done through radiative transfer modeling studies of atmospheric effects using actual atmospheric profile measurements during the validation period.

Radiative transfer modeling of the microwave radiation emanating from the sea ice cover will also be undertaken because it allows for a better understanding of the emission characteristics of different sea ice surfaces at the different AMSR frequencies and polarizations. Such procedure has been conducted previously (e.g., Tjuatja et al., 1993; Grenfell et al., 1994; Tjuatja et al., 1995) but results were of limited value because of the lack of needed atmospheric and surface data. Some refinements will be implemented and data acquired during the validation program will be used to obtain improved results that will be used to better interpret spatial and temporal changes in the microwave signatures as observed in the aircraft, field, and satellite data sets.

Sea Ice Temperature: The ice temperature derived from the vertically polarized 6.9 GHz channel represents the temperature of the sea ice layer that emits much of the signal observed by the radiometer. For first year ice, it is the temperature of the snow/ice interface because at this frequency the snow cover is transparent to the radiation and the surface is opaque due to relatively high salinity. For multiyear ice, the derived sea ice temperature represents a weighted-average of the freeboard portion of the ice. During previous Antarctic cruises, the physical characterization of the ice cover made on a regular basis included quantitative measurements of temperature profiles through the snow and ice. Such data were taken during the Weddell Sea winter and spring cruises of 1982, 1983, 1986, and 1989. These data were used to obtain empirical relationships between the snow skin-depth temperatures and the snow/ice surface temperature. The snow skin-depth temperature is routinely measured by infrared (IR) satellite instruments (e.g., AVHRR, ATSR, and MODIS). The primary technique for the validation of AMSR ice temperature data is to make use of this empirical relationship that converts IR satellite data to ice temperature data and use the latter for comparative analysis with AMSR data. The aircraft IR data will be converted to surface ice temperatures that in turn will be compared with ship measurements to assess errors associated with the use of empirical parameters. Further refinements of the empirical parameters will be made through the use of more field data and a thermodynamic model of sea ice and snow.

The retrieved ice temperatures will be further validated using surface temperature data from buoys, ships, ice camps, and other platforms. While these are only point measurements, the horizontal variability of the snow/ice interface temperature is not expected to be large over a few km. Also, there exist some arrays of buoys that provide continuous measurements and could be used to check the temporal consistency of the derived AMSR temperature data.

6. Computer Requirements and Coordination

6.1 Software and Data Storage Requirements

The Basic Bootstrap algorithm (BBA) has been tested without problems at the NASDA Earth Observation Center data facility and is ready for routine processing. An enhanced version of this algorithm has been enhanced to better account for spatial variations in surface ice temperature as described in this document. The new algorithm is called AMSR Bootstrap Algorithm (ABA). This algorithm has been tested using SMMR data but AMSR data is expected to be much better calibrated and has much higher resolution than SMMR. Further testing is thus necessary once AMSR data becomes available. In the meantime, BBA can be used since results from the two are very similar and the differences where they occur are within errors. Both algorithms have working versions currently running on SGI UNIX workstations at Goddard. ABA is only a slightly bigger program than BBA and there should not be any problem installing it in the NASDA system. An estimate of processing time for one month of SSM/I Level-3 daily average data is of the order of 1.2 minutes and 2.1 minutes on an SGI Octane workstation using BBA and ABA, respectively.

Input to the AMSR-E sea ice algorithms will consist of Level 2A AMSR brightness temperatures, latitude, longitude, time and a land/ocean flag. The output sea ice products will consist of sea ice concentration and sea ice temperature and will include latitude, longitude, and a time stamp. The algorithms are coded in C. As soon as AMSR data is available, ABA will be tested and a final version including documentation will be delivered to NASDA within a few months.

6.2 Data Management, Quality Control and Archival

The NASDA/Earth Observation management is primarily responsible in the acquisition and management of AMSR data. During the first year of operation, AMSR data will also be processed by the PI, using his own computer system, for comparative analysis with other data sets and for quality control. Enhanced techniques and procedures developed during this time will be delivered to NASDA for implementation and generation of the sea ice data sets.

Quality control of brightness temperatures will be done during the generation of the Level 2A products. The first step in the quality control of the sea ice products will consist of checking whether or not the retrieved sea ice products fall within reasonable limits. Diagnostics will be based in part on satellite sea ice climatology developed since the launch of the Nimbus 7 SMMR in 1978. These data will provide a useful measure of the seasonal and regional values for sea ice concentration and to some extent sea ice temperature.

Exception handling will consist of flagging missing data, land, and unreasonable retrievals. Missing brightness temperatures will result in setting a missing flag for the sea ice retrieval. The sea ice algorithm will not be run over land. It is presumed that out-of-range brightness temperatures will be handled in the generation of Level 2A products. Out-of-range retrievals will be handled within the algorithm. Diagnostics for checking out-of-range data will be used in the algorithms to determine whether the output should be flagged as unreasonable. In some cases, for example, sea ice concentrations greater than 100% will be set to 100% and sea ice concentrations less than 0 will be set to zero. Much larger discrepancies will be flagged as unreasonable.

6.3 Consistency Checks and Coordination with Other Projects

Sea ice concentration and ice temperature are two parameters that are obtainable using other satellite sensors. For example, one of the data products that are supposed to be generated from ADEOS-II/GLI and EOS-Agua/MODIS is sea ice concentration using visible channel data. There may be differences in sampling rate, resolution and sensitivity to clouds and weather but where there is good cloud free data available from GLI and MODIS, the retrieved product should agree with that of AMSR. Also, GLI and MODIS sensors have thermal infrared channels that provide surface skin temperatures. After a normalization is applied to the latter, to obtain ice temperature, as discussed earlier, the results should be compatible with ice temperatures derived from AMSR. If not, the reason for the discrepancies should be evaluated in terms of different resolution, different emissivities and reflectivities, and different types of surfaces. Retrieved geophysical parameters should be sensor independent but if the results from different sensors are different, users of the products should be advise about such differences and why.

Validation data are oftentimes very expensive to acquire and should be shared with other projects which might need them. Among the key validation data sets that will be used for AMSR data are the aircraft and Landsat data as described earlier. The same data sets could also be used for validating GLI and MODIS products. Similarly, validation data sets accumulated for GLI and MODIS may be useful for AMSR data validation.

Activities of the scientists and engineers involved in different projects should also be coordinated such that the same set of standards are applied to different sensors, especially those that are similar. For example, AMSR data from both ADEOS-II and EOS-Aqua should be processed with the same quality checks and calibration standards. Similarly for aircraft radiometer AMSR simulator data that need to be compared with satellite data. This will guarantee that data sets from different sensors are consistent and can be used interchangeably and/or in combination for scientific research.

7. Summary

The theoretical basis and description of the algorithm that will be used to derive sea ice parameters from AMSR data has been discussed. Two techniques with almost equal performance are presented. One is called the Basic Bootstrap Algorithm (BBA), which is the original algorithm that was proposed to NASDA for evaluation and was chosen to be used as the standard algorithm for AMSR. An enhanced technique has been developed in the meantime and called AMSR Bootstrap Algorithm (ABA) which is expected to provide more accurate results. The two algorithms, as tested, are currently providing very similar results but ABA has the advantage of accounting for abnormally cold ice surface temperatures and in providing an ice temperature product. The latter is a research product but could provide very valuable information needed for polar process studies that cannot be obtained otherwise. The error in the determination of ice concentration is estimated at about 5 to 15% during winter and 10 to 20 % during the summer using SSM/I data. This significantly improves when AMSR data is used since the latter have much better resolution and greater spectral range. The error in the determination of ice temperature is yet to be determined but is expected to be less than 4K.

8. References:

Aagaard, K., L. K. Coachman, and E. C.mack, On the halocline of the Arctic ocean, *Deep Sea Res.*, 28, 529-545, 1981.

Badgley, F. I., Heat budget at the surface of the Arctic Ocean, in Proc. of the Symp. on the Arctic Heat Budget and Atmospheric Circulation, J. O. Fletcher, ed., pp. 267-277, 1966.

Bjørgo, E., O.M. Johannessen, and M.W. Miles, Analysis of merged SSMR-SSM/I time series of Arctic and Antarctic sea ice parameters 1978-1995. *Geophys. Res. Lett.*, *24*(4), 413-416, 1997.

Bromwich, D.H., T.R. Parish, and C.A. Zorman, The confluence Zone of the intese katabatic winds at the Terra Nova Bay, Antarctica, as derived from airborne sastrugi surves and mesoscal numerical modeling, J. Geophys. res., 95(D5), 5495-5509, 1990.

Budyko, M.I., Polar ice and climate, In Proceedings of the Symposium of the Arctic Heat Budget and Atmospheric Circulation, ed. by J.O. fletcher (ed), RM5233-NSF, Rand Corporation, Santa Monica, CA, 3-21, 1966.

Businger, S., and R. J. Reed, Polar lows, in Polar and Arctic Lows, Twitchell, P. F., E. A. Rasmussen, and K. L. Davidson, eds., A. Deepak, Hampton, VA, pp. 3-45, 1989.

Carleton, A. M., Satellite climatological aspects of the "polar low" and "instant occlusion," Tellus 37A, 433-450, 1985.

Cavalieri, D. J., NASA Sea Ice Validation Program for the Defense Meteorological Satellite Program Special Sensor Microwave Imager, J. Geophys. Res., 96, 21,969- 21,970, 1991.

Cavalieri, D. J., The validation of geophysical parameters using multisensor data, Chapter 11 in Microwave Remote Sensing of Sea Ice, edited by F. D. Carsey, American Geophysical Union Monograph 68, 233-242, 1992.

Cavalieri, D. J., and S. Martin, The contribution of Alaskan, Siberian, and Canadian coastal polynyas to the cold halocline layer of the Arctic Ocean, *J. Geophys. Res.*, 18,343-18,362, 1994.

Cavalieri, D. J., P. Gloersen, and W. J. Campbell, Determination of sea ice parameters with the Nimbus 7 SMMR, J. Geophys. Res., 89, 5355-5369, 1984.

Cavalieri, D. J., J. Crawford, M. R. Drinkwater, D. Eppler, L. D. Farmer, R. R. Jentz and C. C. Wackerman, Aircraft active and passive microwave validation of sea ice concentration from the DMSP SSM/I, *J. Geophys. Res.*, 96, 21,989-22,008, 1991.

Cavalieri, D.J., C.L. Parkinson, P. Gloersen, J.C. Comiso, and H.J. Zwally, Deriving long-term time series of sea ice cover from satellite passive microwave data sets, *J. Geophys. Res.*, *104*(C7), 15803-15814, 1999.

Cho, K., N. Sasaki, H. Shimoda, T. Sakata, and F. Nishio, Evaluation and improvement of SSM/I sea ice concentration algorithms for the Sea of Okhotsk, *J. Remote Sensing Soc. of Japan, 16*(2), 47-58, 1996.

Comiso, J. C., Sea ice effective microwave emissivities from satellite passive microwave and infrared observations, J. Geophys. Res., 88, 7686-7704, 1983.

Comiso, J. C., Characteristics of winter sea ice from satellite multispectral microwave observations, *J. Geophys. Rev., 91*(C1), 975-994, 1986.

Comiso, J.C., Arctic Multiyear ice Classification and Summer Ice Cover using Passive Microwave Satellite Data, *J. Geophys. Res.*, 95, 13411-13422, 1990.

Comiso, J.C., SSM/I Concentrations using the Bootstrap Algorithm, *NASA RP, 1380*, 40pp, 1995.

Comiso, J. C. and K. Steffen, Studies of Antarctic sea ice concentrations from satellite observations and their applications, *J. Geophys. Res.*, *106*(C12), 2001.

Comiso, J. C. and C. W. Sullivan, Satellite microwave and in-situ observations of the Weddell Sea Ice Cover and its Marginal Ice Zone, *J. Geophys. Res., 91(*C8), 9663-9681, 1986.

Comiso, J.C., and R. Kwok, The summer Arctic sea ice cover from satellite observations, J. *Geophys. Res.*,101(C2), 28397-28416, 1996.

Comiso, J. C., S. F. Ackley, and A. L. Gordon, Antarctic Sea Ice Microwave Signature and their Correlation with In-Situ Ice Observations, J. Geophys. Res. 89(C1):662-672, 1984.

Comiso, J. C., and H. J. Zwally, Antarctic Sea Ice Concentrations Inferred from Nimbus-5 ESMR and LANDSAT imagery, *J. Geophys. Res., 87*(C8), 5836-5844, 1982.

Comiso, J.C., and H.J. Zwally, Temperature Corrected Bootstrap Algorithm, IEEE *IGARSS'97 Digest*, Volume 3, 857-861, 1997.

Comiso, J. C., T. C. Grenfell, D. L. Bell, M. A. Lange,and S. F. Ackley, Passive Microwave In Situ Observations of Winter Weddell Sea Ice, *J. Geophy. Res., 94*, 10891-10905, 1989.

Comiso, J.C., P. Wadhams, W. Krabill, R. Swift, J. Crawford, and W.Tucker, Top/Bottom multisensor remote sensing of Arctic sea ice, J. Geophy. Res., 96(C2), 2693-2711, 1991.

Comiso, J.C, T.C. Grenfell, M. Lange, A. Lohanick, R.Moore, and P. Wadhams, "Microwave remote sensing of the Southern Ocean Ice Cover," Chapter 12, In, *Microwave Remote Sensing of Sea Ice*, (ed. by Frank Carsey), American Geophysical Union, Washington, D.C., 243-259, 1992.

Comiso, J.C., D. Cavalieri, C. Parkinson, and P. Gloersen, Passive microwave algorithms for sea ice concentrations, *Remote Sensing of the Env., 60*(3), 357-384, 1997.

Gloersen P., W. Campbell, D. Cavalieri, J. Comiso, C. Parkinson, H.J. Zwally, Arctic and Antarctic Sea Ice, 1978-1987: Satellite Passive Microwave Observations and Analysis, *NASA Spec. Publ. 511*, 1992.

Gloersen, P. and Barath, F. T., A Scanning Multichannel Microwave Radiometer for Nimbus-G and SeaSat-A, *IEEE Journal of Oceanic Engineering, OE-2,* 172-178, 1977.

Gloersen P., W. J. Campbell, D. J. Cavalieri, J. C. Comiso, C. L. Parkinson, H. J. Zwally, rctic and Antarctic Sea Ice, 1978-1987: Satellite Passive Microwave Observations and Analysis, NASA Spec. Publ. 511, 1992.

Gloersen, P., E. Mollo-Christensen, and P. Hubanks, Observations of Arctic polar lows with the Nimbus 7 Scanning Multichannel Microwave Radiometer, in Polar and Arctic Lows, P. F. Twitchell, E. A. Rasmussen, and K. L. Davidson, eds., A. Deepak, Hampton, Virginia, pp. 359-371, 1989.

Gloersen, P., T. C. Chang, T. T. Wilheit, and W. J. Campbell, Polar sea ice observations by means of microwave radiometry, in Advanced Concepts and Techniques in the Study of Snow and Ice, H. S. Santeford and J. L. Smith, eds., Nat. Acad. Sci, pp. 541-550, 1974.

Gordon, A., Deep Antarctic convection west of Maud Rise, J. *Phys. Oceanography.*, 8, 600-612, 1978.

Gordon, A. L., and J. C. Comiso, Polynyas in the Southern Ocean, *Scientific American, 256*(6), 90-97, 1988.

Grenfell, T.C., J.C. Comiso, M.A. Lange, H. Eicken, and M.R. Wenshahan, Passive microwave observations of the Weddell Sea during austral winter and early spring, J. Geophys, Res., 99(C5), 9995-10,010, 1994.

Grenfell, T. C., A theoretical model of the optical properties of sea ice in the visible and near infrared, *J. Geophys. Res.*, 88, 9723-9735, 1983.

Grenfell, T. C., and J. C. Comiso, Multifrequency passive microwave observations of first-year sea ice grown in a tank, IEEE *Trans. Geoscience and Remote Sensing,* GE-24, 826-831, 1986.

Grenfell, T. C., J. C. Comiso, M. A. Lange, H. Eicken, and M. R. Wenshahan, Passive microwave observations of the Weddell Sea during austral winter and early spring, *J. Geophys, Res.*, 99(C5), 9995-10010, 1994.

Grenfell, T.C, D.J. Cavalieri, J.C. Comiso, M.R. Drinkwater, R.G. Onstott, I. Rubinstein, K Steffen, I. Rubinstein, D.P. Winebrenner, "Microwave signatures of new and young ice," Chapter 14, *Microwave Remote Sensing of Sea Ice,* (ed. by Frank Carsey), American Geophysical Union, Washington, D.C., 291-301, 1992.

Honda, M., K. Yamazaki, Y. Tachibana, and K. Takeuchi, Influence of Okhhotsk sea-ice extent on atmospheric circulation, *Geophysical Research Letters,* 23, 3595-3598, 1996.

Jacobs, S. and J. C. Comiso, Satellite passive microwave sea ice observations and oceanic processes in the Ross Sea, Antarctica, *J. Geophys. Res.*, *94*, 18195-18211, 1989. Jacobs, S.S, and J.C. Comiso, A recent sea-ice retreat west of the Antarctic Peninsula, *Geophys. Res. Letter, 20*(12), 1171-1174, 1993.

Jacobs, S.S., and J.C. Comiso, A climate anomaly in the Amundsen and Bellingshausen Seas, *J. Climate, 10*(4), 697-709, 1997.Killworth, P. D., Deep convection in the world ocean, Rev. Geophys. and Space Phys. 21, 1-26, 1983.

Johannessen, O.M., E.V. Shalina and M.W. Miles, Satellite evidence for an Arctic sea ice cover in transformation, *Science, 286*, 1937-1939, 1999.

Jones, P.D., M. New, D.E. Parker, S. Martin, and I.G. Rigor, Surface air temperature and its changes over the past150 years, *Rev. Geophys., 37,* 173-199, 1999.

Kwok, R., J.C. Comiso, and G. Cunningham, Seasonal characteristics of the perennial ice cover of the Beaufort Sea, *J. Geophys. Res.,101*(C2), 28417-28439, 1996.

King, J. C. and S. A. Harangozo, Climate change in the western Antarctic Peninsula since 1945: observations and possible causes, Annals of Glac., 27, 571-575, 1998.

Killworth, P. D., Deep convection in the world ocean, Rev. Geophys. and Space Phys. 21, 1-26, 1983.

Markus, T. and D. J. Cavalieri, A revision of the NASA Team sea ice algorithm, *IEEE Transactions on Geoscience and Remote Sensing, 38*(3), 1387-1298, 2000.

Martin, S., K. Steffen, J.C. Comiso, D.J. Cavalieri, M. Drinkwater, B.M. Holt, "Microwave Remote Sensing of Polynyas," Chapter 15, *Microwave Remote Sensing of Sea Ice,* (ed. by Frank Carsey), American Geophysical Union, Washington, D.C., 303-311, 1992.

Massom, R., *Satellite remote sensing of polar regions,* Lewis Publishers, Florida, 307pp, 1991.

Massom, R.A., J.C. Comiso, A.P. Worby, V. Lytle, and L. Stock, Satellite and in situ observations of regional classes of sea ice cover in the East Antarctic pack in winter, Remote Sensing of the Env., 68(1), 61-76, 1999.

Mätzler, C., R.O. Ramseier, and E. Svendsen, Polarization effects in sea ice signatures, *IEEE J. Oceanic Eng. OE-9,* 33-338, 1984.

Maykut, G. A., Energy exchange over young ice in the central Arctic, J. Geophys. Res., 83(C7), 3646-3658, 1978.

Oelke, C., Atmospheric signatures in sea-ice concentration estimates from passive microwaves: modelled and observed, *Int. J. Remote Sensing, 18*, 1113-1136, 1997.

Parkinson, C. L., J. C. Comiso, H. J. Zwally, D. J. Cavalieri, P. Gloersen, and W. J. Campbell (1987), Arctic Sea Ice 1973- 1976 from Satellite Passive Microwave Observations, NASA Spec. Publ. 489, pp.296, 1987.

Parkinson, C. L., D. J. Cavalieri, P. Gloersen, H. J. Zwally, and J. C. Comiso, Variability of the Arctic Sea Ice Cover 1978-1996, *J. Geophys. Res.*, 104, 20,837-20,856, 1999.

Preller, R. H., J. E. Walsh, and J. A. Maslanik, The use of satellite observations in ice cover simulations, Chapter 22, in Microwave Remoate Sensing of Sea Ice, F. D. Carsey (ed.), Geophysical Monograph 68, American Geophysical Union, Washington, DC, 1992.

Rothrock, D. A., Y. Yu, and G. A. Maykut, Thinning of the Arctic sea-ice cover, G*eophys. Res. Lett.*, 26(23), 3469-3472, 1999.

Schluessel, P. and H. Grassl, SST in polynyas: A case study, International Journal of Remote Sensing, 11(6), pp.933-945, 1990.

Steffen, K. and A. Schweiger, NASA team algorithm for sea ice concentration retrieval from the Defense Meteo-rological Satellite Program Special SensorMicrowave Imager: Comparison with Landsat Imagery, J. Geophys. Res., 96(12), 21971-21987, 1991.

Stommel, H., On the smallness of sinking regions in the ocean, Proc. Nat. Acad. Sc., USA 48, 766-772, 1962.

Svendsen, E., K. Kloster, K., B. Farrelly, O. M. Johannessen, J. A. Johannessen, W. J. Campbell, P. Gloersen, D. J. Cavalieri, and C. Matzler, Norwegian Remote Sensing Experiment: Evaluation of the Nimbus 7 Scanning multichannel microwave radiometer for sea ice research, J. Geophys. Res., 88, 2781-2792, 1983.

Swift, C. T., L. S. Fedor, and R. O. Ramseier, An algorithm to measure sea ice concentration with microwave ra-diometers, J. Geophys. Res., 90, 1087-1099, 1985.

Tjuata, S., A.K. Fung, and J.C. Comiso, Effects of Snow Cover on Sea Ice Emission, *IEEE IGARSS'95 Digest*, Vol. 1, 697-699, 1995.

Tjuata, S., A.K. Fung, and M. Dawson, An analysis of scattering and emission from sea ice, *Remote Sensing Review*, *7*, 83-106, 1993.

Vowinckel, E., and S. Orvig, The climate in the north polar basin, in Climate of the Polar Regions, Vol.14 of World Survey of Climatology, Elsevier, Amsterdam, pp. 129-252, 1970.

Tucker III, W.B., D.K. Perovich, A.J. Gow, W.F. Weeks, and M.R. Drinkwater, Physical properties of sea ice relevant to remote sensing, Chapter 2, *Microwave Remote Sensing of Sea Ice*, (ed. by Frank Carsey), American Geophys. Union, Washington, DC., 201-231, 1992.

Wadhams, P., and N. Davis, Further evidence of ice thinning in the Arctic Ocean, *Geophy. Res. Lett.*, *27*(24), 3973-3976, 2000.

Walsh, J. E., and H. J. Zwally, Multiyear sea ice in the Arctic: model- and satellite-derived, J. Geophys. Res. 95, 11,613-11,628, 1990.

Wensnahan, M., Maykut, G. A., Grenfell, T. C., and D. P. Winebrenner, Passive microwave remote sensing of thin sea ice using principal component analysis, J. Geophys. Res., 98, 12,453-12,468, 1993.

Worby, A. P., and R. A. Massom, The structure and properties of sea ice and snow cover in East Antarctic pack ice, Antarctic CRC, Research report, 7, 191 pp., 1995. Worby, A.P., and J. Comiso, A study of the Antarctic Sea Ice Edge using SSM/I-Derived and in situ Observations, *IGARSS Digest 2001*, Sydney, Australia, July 2001.

Worby, A.P., and R.A. Massom, The structure and properties of sea ice and snow cover in East Antarctic pack ice, *Antarct. CRC Res. Rep., 7,* 191 pp., Antarct. Coop. Res. Cent., Hobart, Tasmania, 1995.

Yamanouchi, T., and K. Seko, Antarctica from NOAA satellites, National Institute of Polar Research Press, Tokyo, Japan, 91 pp., 1992.

Zwally, H. J., J. C. Comiso, C. L. Parkinson, W. J. Campbell, F. D. Carsey, and P. Gloersen, Antarctic Sea Ice 1973-1976 from Satellite Passive Microwave Observations, *NASA Spec. Publ. 459*, 1983.

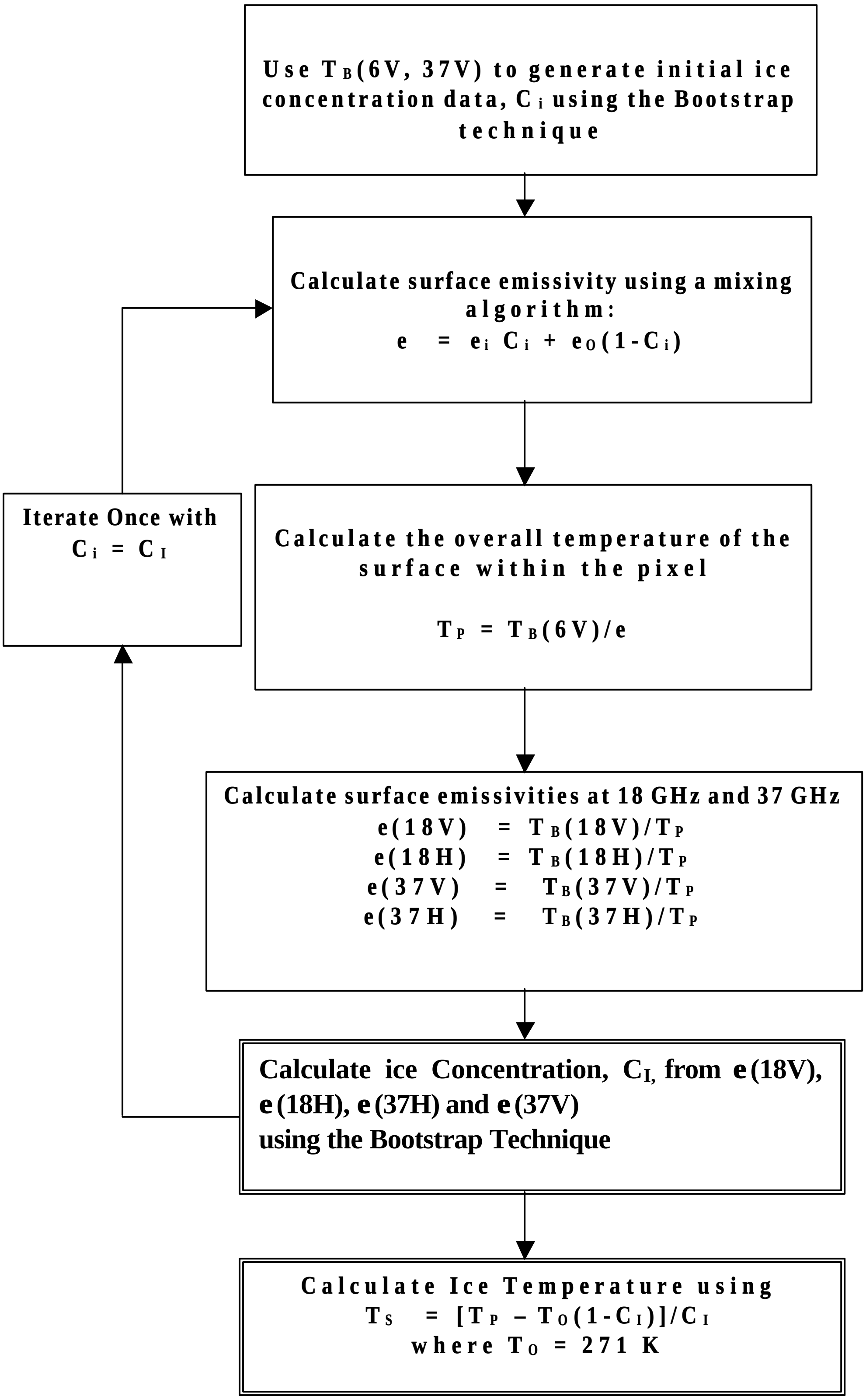

Figure 3. Schematics of the AMSR Bootstrap Algorithm

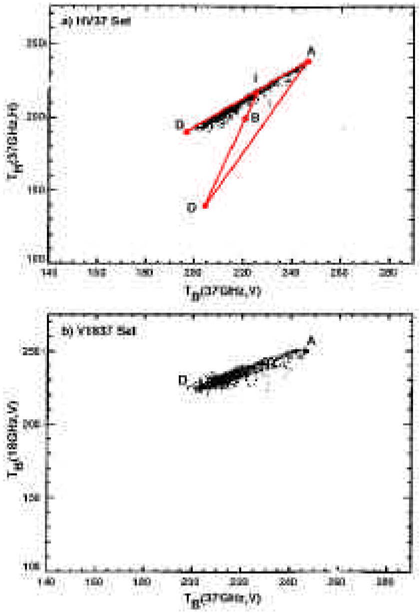
a) HV37 Set
A
I
B
D
D
T_H(37GHz,H)
T_B(37GHz,V)
100
150
200
250
140
160
180
200
220
240
260
280
b) V1937 Set
A
D
T_B(18GHz,V)
T_B(37GHz,V)

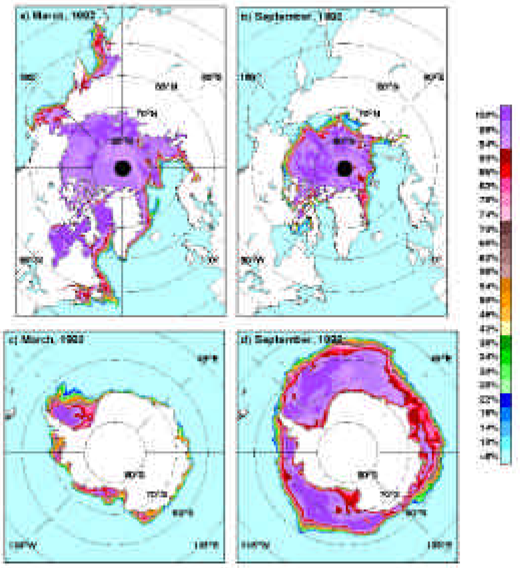
a) March, 1992
b) September, 1992
c) March, 1992
d) September, 1992
180°
90°E
90°W
0°
70°N
80°N
60°N
90°S
70°S
60°S

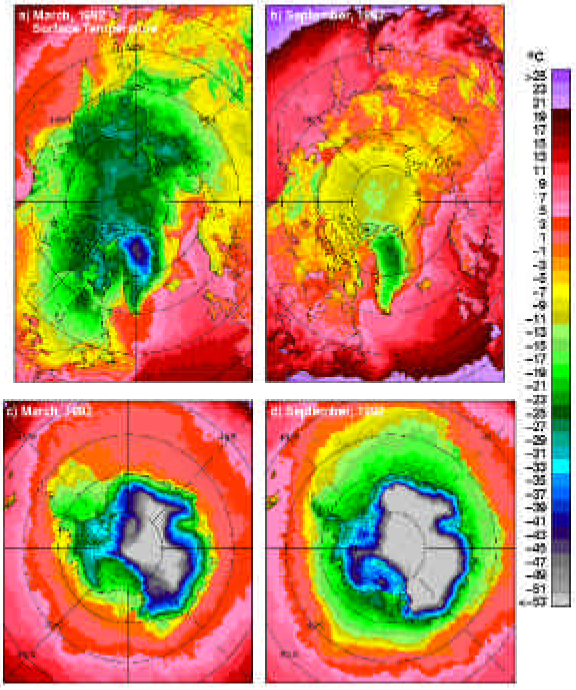
a) March, 1992
Surface Temperature
b) September, 1992
c) March, 1992
d) September, 1992
°C
>25
23
21
19
17
15
13
11
9
7
5
3
1
-1
-3
-5
-7
-9
-11
-13
-15
-17
-19
-21
-23
-25
-27
-29
-31
-33
-35
-37
-39
-41
-43
-45
-47
-49
-51
<-53

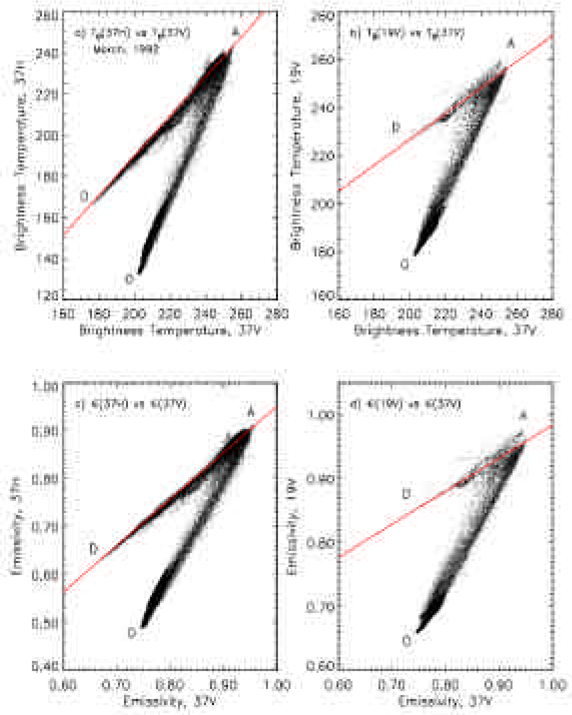
a) T_B(37H) vs T_B(37V)
March, 1992
b) T_B(19V) vs T_B(37V)
c) ε(37H) vs ε(37V)
d) ε(19V) vs ε(37V)
A
D
Brightness Temperature, 37H
Brightness Temperature, 19V
Brightness Temperature, 37V
Emissivity, 37H
Emissivity, 19V
Emissivity, 37V
120
140
160
180
200
220
240
260
280
0.40
0.50
0.60
0.70
0.80
0.90
1.00

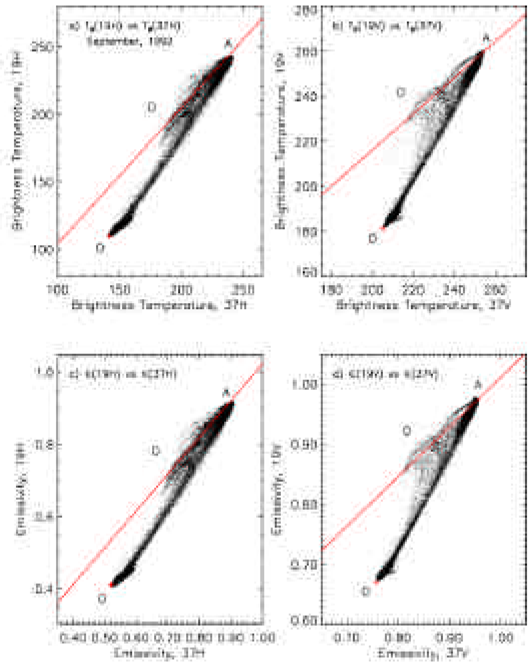
a) T_B(19H) vs T_B(37H)
September, 1992
b) T_B(19V) vs T_B(37V)
c) ε(19H) vs ε(37H)
d) ε(19V) vs ε(37V)
A
D
O
Brightness Temperature, 19H
Brightness Temperature, 37H
Brightness Temperature, 19V
Brightness Temperature, 37V
Emissivity, 19H
Emissivity, 37H
Emissivity, 19V
Emissivity, 37V
100
150
200
250
160
180
200
220
240
260
0.4
0.6
0.8
1.0
0.40
0.50
0.60
0.70
0.80
0.90
1.00
0.70
0.80
0.90
1.00

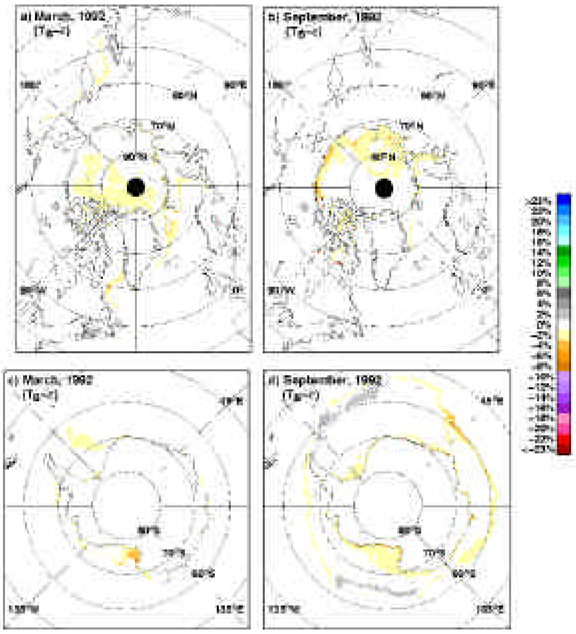
a) March, 1992
(T_B-ε)
b) September, 1992
(T_B-ε)
c) March, 1992
(T_B-ε)
d) September, 1992
(T_B-ε)
180°
90°E
90°W
0°
60°N
70°N
80°N
60°S
70°S
80°S
45°E
135°W
135°E

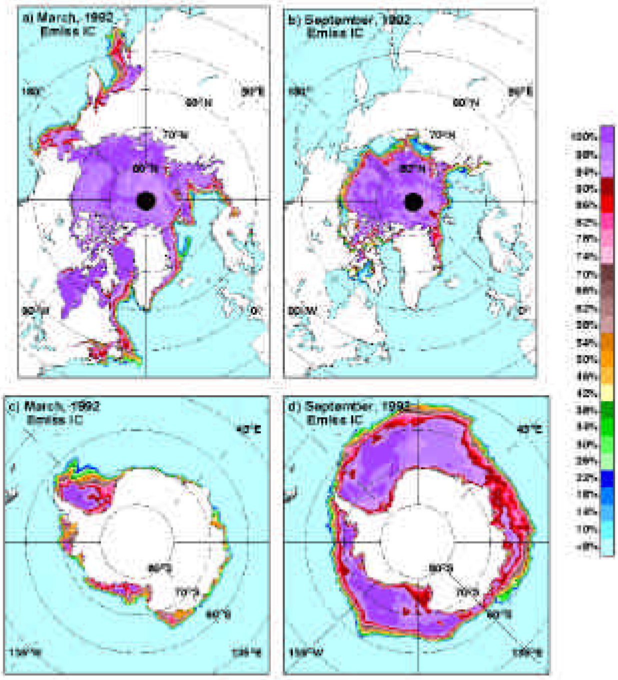
a) March, 1992
Emiss IC
b) September, 1992
Emiss IC
c) March, 1992
Emiss IC
d) September, 1992
Emiss IC
180°
90°E
90°W
0°
60°N
70°N
80°N
60°S
70°S
80°S
45°E
135°W
135°E
100%
98%
94%
90%
86%
82%
78%
74%
70%
66%
62%
58%
54%
50%
46%
42%
38%
34%
30%
26%
22%
18%
14%
10%
<6%

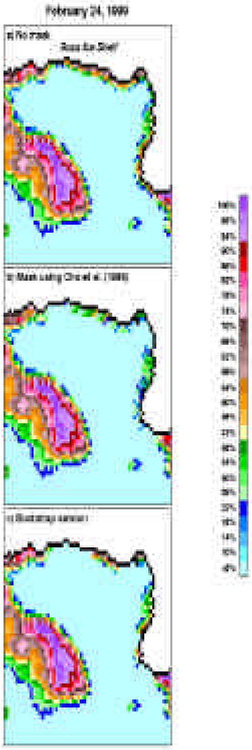
February 24, 1999
a) No mask
Ross Ice Shelf
b) Mask using Cho et al. (1996)
c) Bootstrap version

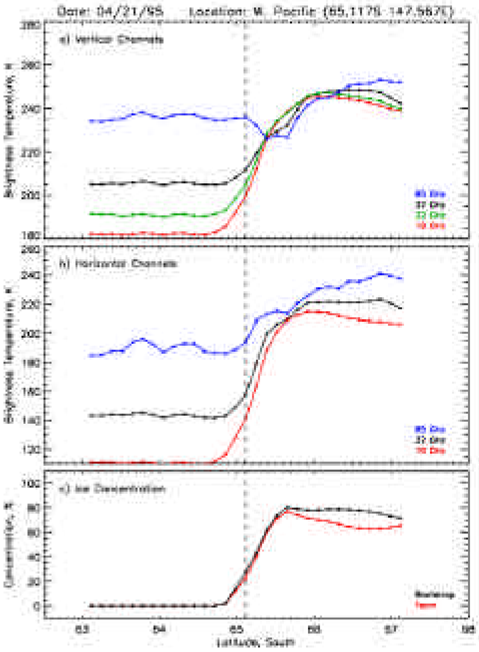
Date: 04/21/95 Location: W. Pacific (65.117S 147.567E)
a) Vertical Channels
Brightness Temperature, K
85 GHz
37 GHz
22 GHz
19 GHz
b) Horizontal Channels
Brightness Temperature, K
85 GHz
37 GHz
19 GHz
c) Ice Concentration
Concentration, %
Bootstrap
Team
63
64
65
66
67
68
Latitude, South

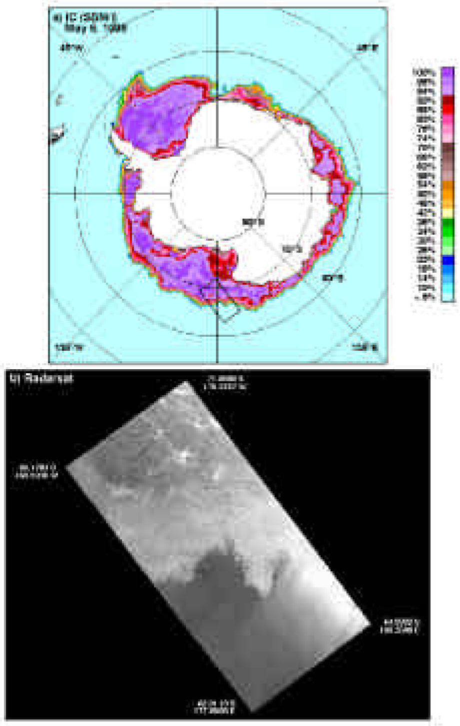
a) IC (SSM/I)
May 6, 1998
45°W
45°E
135°W
135°E
90°S
70°S
60°S
b) Radarsat

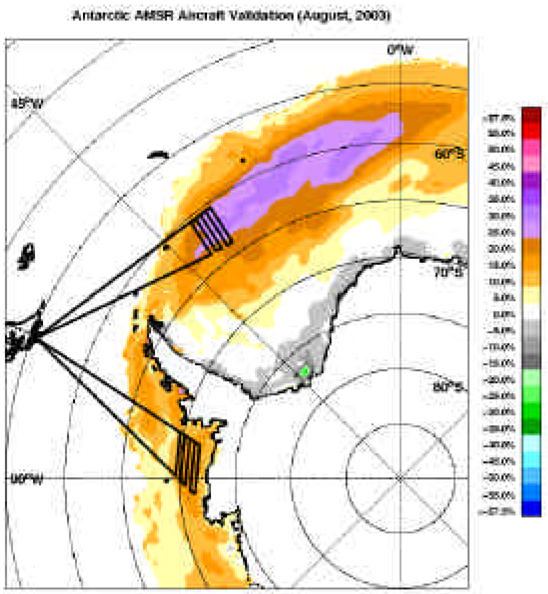
Antarctic AMSR Aircraft Validation (August, 2003)
0°W
45°W
60°S
70°S
80°S
90°W
>57.5%
55.0%
50.0%
45.0%
40.0%
35.0%
30.0%
25.0%
20.0%
15.0%
10.0%
5.0%
0.0%
-5.0%
-10.0%
-15.0%
-20.0%
-25.0%
-30.0%
-35.0%
-40.0%
-45.0%
-50.0%
-55.0%
<-57.5%

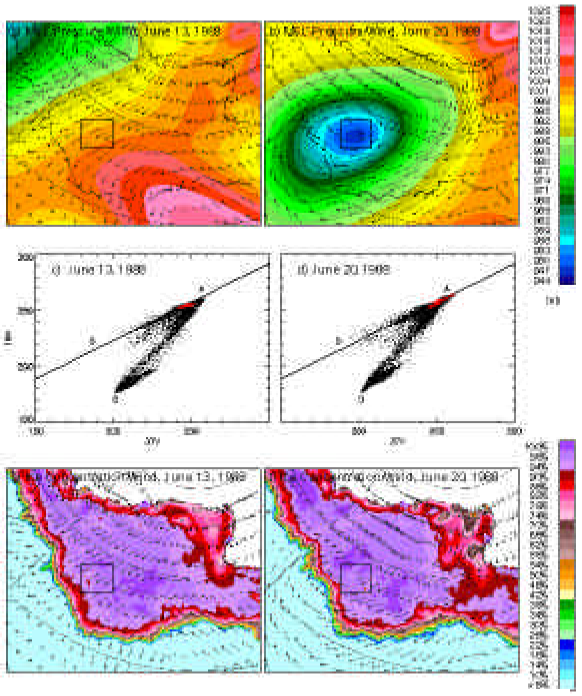
a) MSL Pressure/Wind, June 13, 1988
b) MSL Pressure/Wind, June 20, 1988
c) June 13, 1988
d) June 20, 1988
Ice Concentration/Wind, June 13, 1988
Ice Concentration/Wind, June 20, 1988

Description of Snow Depth Retrieval Algorithm for ADEOS II AMSR

Dr. Alfred Chang and Dr. Richard Kelly
NASA/GSFC

1. Introduction

The development of a snow depth retrieval algorithm for ADEOS II AMSR has been developed from current applications of snow depth retrievals from the Special Sensor Microwave Imager (SSM/I). While the SSM/I is not exactly identical in spatial and waveband configuration to the planned ADEOS II AMSR, it is sufficiently comparable over its four frequencies to be a useful instrument with which to develop a snow retrieval algorithm that is based on the microwave emission properties of snow. The AMSR will have an improved spatial resolution and expanded waveband range compared with the SSM/I and it is expected, therefore, that algorithm development will continue post launch.

2. Underlying principles for snow depth retrieval

There are two aspects to successful snow cover retrieval from space using passive microwave radiometers. First, the snowpack must be detected and second it must be quantified in terms of its snow depth. Fresh of dry snow (containing a negligible amount of liquid water) is a forward scatter of naturally upwelling radiation. Compared with non-snow surfaces, therefore, a snowpack has a distinctive electromagnetic signature at frequencies above 25 GHz. When viewed using passive microwave radiometers from above the snowpack, the scattering of upwelling radiation depresses the brightness temperature of the snow at increasingly high frequencies. This scattering behavior of snow can be exploited to detect the presence of snow on the ground. Having detected the snow, it is then possible to estimate the snow depth of the pack using the degree of scattering. Chang *et al.* (1987) proposed a scheme to estimate the snow depth of a dry, homogeneous, single layer snowpack using radiative transfer theory and the difference between two horizontally-polarized brightness temperature channels at high and low frequencies such that:

$$SD = a \quad DTB) + b \text{ [cm]}, \qquad (1)$$

where b is generally regarded as zero and a = 1.59 cm K^1 and the assumption is made that the snow grain radius is 0.3 mm and snow density is 300 kg m^{-3}. The *DTB* term is the difference in brightness temperature between 19 GHz and 37 GHz channels (horizontal polarization). This model works well under the non-complex snow conditions (flat land, no significant forest cover, single layer dry snow) and has been the basis for several SD or snow water equivalent (SWE) retrieval algorithms (e.g. Goodison and Walker, 1994, Foster *et al.*, 1997). However, for global applications there are several additional factors that need to be taken into consideration and incorporated into a retrieval scheme for successful snow depth estimation. These are described in the following section.

3. Confounding factors

Snowpack properties

It is known that at passive microwave wavelengths, shallow snow (less than 10 cm) is transparent to naturally upwelling microwave wavelengths (Armstrong and Brodzik, 1999). This factor can lead to non-detection of the snowpack and hence underestimation of the snow volume. This factor will be most prominent in the early and late parts of the winter season. Use of a high frequency channel (e.g. 89 GHz on AMSR) will assist with this detection although great care must be exerted when using this channel on account of potential atmospheric contamination.

Wet snow can confound snow depth retrievals by depressing the scattering behaviour of the snow. Ultimately, this leads to underestimation of the pack. Unfortunately, at present there is little that can be done to overcome this problem directly although at least the detection of wet snow is possible by using a combination of information about the surface temperature (Sun *et al.*, 1996), polarization difference at 37 GHz (Walker and Goodison, 1994) and immediate snow cover history.

Equation (1) above indicates a static parameterization based on radiative transfer properties of a snowpack (0.3 mm radius grains and 300 Kg m^{-3} density). While this can be applied in some areas around the world at certain times, the nature of snow is such that it can be temporally and spatially dynamic in evolution (Colbeck, 1986). To retain the *a* coefficient in (1) suggests that globally, snow covers are homogeneous in character which clearly is not the case. Although Josberger *et al.* (1995) found that snowpack properties can be homogeneous at regional scales, for continental applications this will not be the case. The *a* coefficient should, therefore, be varied both spatially and temporally and so we have computed a set of coefficients for each month of the year. The spatial distribution of the coefficients is achieved using the seasonal snowpack classification of Sturm *et al.* (1995) which divides the northern hemisphere into 6 dominant regional snow types: taiga, tundra, alpine, maritime, ephemeral and prairie. The *a* coefficients are re-computed for each of these regions based on dominant snowpack characteristics thought to dominate in each region.

False scatterers

Precipitation acts as a confounding effect on snowpack retrievals. This is because precipitation clouds consist of hydrometeors that act like a snowpack on the ground and scatter upwelling microwave radiation away from the radiometer's field of view. Currently it is not possible to detect the presence of snow or retrieve snow depth from beneath precipitating clouds but it is possible to detect precipitation and therefore flag the presence of rainfall. The method used was developed by Grody and Basist (1996).

Forest cover

A major problem in large areas of the globe is the effect that forest cover has on the retrieval of snow depth from passive microwave radiometers (Chang *et al.*, 1996). Dense coniferous (and perhaps deciduous forest at early/late times in the season) depress the microwave scattering signal from snow within the forest causing an under-retrieval of the snow depth. Attempts have been made to overcome the problem (e.g. Foster *et al.*, 1997) but the problem is not easily resolvable at the moment. The Robinson and Kukla (1985) global albedo data set has been used to estimate forest cover through the following relationship:

$$ff = -150albedo + 120 \qquad [\%] \qquad (2)$$

where *ff* is the forest fraction in percent and the two coefficients describe a straight line. This linear relationship is based in the fact that for land surfaces that are not water bodies, low albedos (<0.5) are likely to be indicative of dense forest whilst higher albedos (>0.5) are probably indicative of low stand or no vegetation. The range of forest cover is calibrated to between 0 % and 90 %and is then re-scaled linearly to 0 to 1 where 1 represents 100 % and 0 represents 0 % such that the data can be incorporated into (1):

$$SD = a \;\; DTB) / (1-ff) + b \qquad [\text{cm}]. \qquad (3)$$

A full account of this relationship can be found in Foster *et al.* (1997). This relationship is currently under further refinement since the Robinson and Kukla (1985) data set is at 1.0° spatial resolution which is coarser than the scale used in this project (9.28 km equal area grid). In addition, there are better products available and becoming available to provide more up-to date information about the global distribution of forest cover. For example, direct forest cover data are available through the International Geosphere and Biosphere Project (IGBP) (although these are derived from annual average land cover data sets based on the reflective properties of the land surface from AVHRR data). It is expected that in the future, more dynamic forest cover information will be available through MODIS reflectance or land category products that are produced every 16 days. This will provide a better characterization of the forest cover plus it will give improved information about stem volume (rather than percentage cover in a pixel) which is thought to be the key effect on microwave retrievals of snow in forested areas (Kurvonen *et al.*, 1998).

Mountainous terrain

Retrieval of snow depth from complex mountain topography is a challenge for low spatial resolution passive microwave radiometers. This is because within a given footprint in a mountain zone, the variability of snow depth is much greater than in flat terrain. Consequently, to avoid underestimation and overestimation, such terrain is flagged and avoided in the current version of the algorithm. The GTOPO30 product from the USGS is used to flag mountain topography.

4. Implementation of the algorithm

The algorithm, coded in C, is currently implemented from a Unix Bourne Shell. The procedure is shown by the flow chart in Figure 1 below. The first step is to determine the kind of surface present (flat land, water body on land, ice, ocean, mountainous terrain, snow climatologically (im)possible, forest cover). The climatological possibility of snow cover presence is obtained from Dewey and Heim (1981 and 1983). Unless the surface is flat land without heavy forest cover, the procedure flags the surface type and does not attempt to compute the snow depth. For flat land without heavy forest cover, the algorithm proceeds to Step 2, which reads, in AMSR channel brightness temperatures.

Step 3 determines that the AMSR data are within a reasonable range and that there are no gross data errors in the brightness temperature. Step 4 obtained the surface temperature estimate based global circulation model estimates from the Japanese Meteorological Agency. This step is used to determine whether or not the surface is likely to be too warm and, therefore, the probability is low for the presence of snow. Step 5 screens for precipitation and Step 6 determines whether there is wet or dry snow present and Step 7 estimates the snow depth. If the snow is dry, the algorithm computes the snow depth using equation (3) above. The applied *a* coefficient in (3) dependent on whether or not the underlying soil is dry or wet, the Sturm *et al.* (1995) seasonal snow class and also on the time of year.

5. Validation of algorithm

Two data sets were assembled to validate the algorithm developed for ADEOS II AMSR snow depth estimation. First, a four-year record from 1992 – 1995 of daily GTS meteorological station snow depth measurements and coincident SSM/I brightness temperatures prepared by NASDA, Japan were reanalyzed (see Chang and Koike, 2000). The second data set used was a month of daily global WMO meteorological station snow depth data for January 2001.

1992-1994 data set validation

This data set comprises 86 GTS meteorological stations distributed in the northern hemisphere and quality controlled (originally there were 100 but anomalous and erroneous readings were screened). The data comprise four years of gauged daily snow depth measurements from January 1992 to December 1995. Coincident SSM/I brightness temperatures at each station are also stored in the data set.

Snow depth was estimated using the simple algorithm from equation 1 (hereafter referred to as the “1.59” algorithm) and also using the spatially and temporally dynamic algorithm from equation 3 (hereafter referred to as the Chang algorithm). The estimated snow depths from both algorithms were compared with the gauge data and the mean absolute error (an indicator of the magnitude of algorithm error) and the mean error (a measure of algorithm bias) for both algorithms for the entire four-year period was computed. Figure 1 shows two histograms of the results. The mean absolute error (MAE) histogram shows that both algorithms perform similarly well at the global scale. The average MAE for the Chang algorithm is 16.6 cm while for the “1.59” algorithm it is 16.1 cm. This would suggest that the errors are similar in magnitude for each station over the four years. However, inspection of the bias in the adjacent histogram demonstrates that the Chang algorithm bias is much closer to 0 cm than the “1.59” algorithm (-5.9 cm and –0.3 cm for Chang and “1.59” respectively). This suggests that although the absolute errors are similar, the underestimation of snow depth traditionally found in the passive microwave estimates, is reduced in the new algorithm. The reason for this could be on account of the fact that the new Chang algorithm incorporates the “forest effect” in its estimates thus reducing the bias (underestimation) commonly found in retrievals. Figure 2 shows the MAE and ME for sites where the forest fraction is greater than 30%. Again a similar situation emerges with similar average MAE estimates for both algorithms (19.6 cm and 21.3 cm for the “1.59” and Chang algorithms respectively). However, the average bias in the Chang algorithm is much less under high forest fractions with an average ME of –13.7 cm and 1.3 cm for the “1.59” and Chang algorithm respectively.

Figure 1
AMSR Snow depth algorithm logic

Preliminaries

Get Ancillary Data:

- Land/sea/ice
- Topography
- Snow class (Sturm *et al.*, 1995)
- Snow (Im)possible

Locate AMSR data and read in one scan line of AMSR data.

Step 1 (For each AMSR sample)

Test for:

- Ocean, land water body, ice **FLAG**
- Snow Impossible **FLAG**
- Mountain **FLAG**
- Otherwise *continue to Step 2*

Step 2 Obtain AMSR brightness temperatures

Continue to Step 3

Step 3 Do range check of brightness temperatures in all channels

- Bad data **FLAG**
- Good data *continue to Step 4*

Step 4 Obtain surface temperature from Japan Meteorological Agency global circulation model data:

- If $T \geq 275$ K, surface too warm **FLAG**
- If $T < 275$ K *continue to Step 5*

Step 5 Precipitation screen (Grody and Basist (1996)):

$Scat = \max(Tb_{18V}-Tb_{36V} - 3,\ Tb_{23V}-Tb_{89V} - 3,\ Tb_{36V}-Tb_{89V} - 1)$

- If $(Tb_{23V} > 258)$ or $(Tb_{23V} > 254$ and $Scat < 2)$ or $(Tb_{23V} > (165+0.49Tb_{89V})$ then rainfall is present **FLAG**
- Otherwise *continue to Step 6*

Step 6 Wet or dry snow screen (Walker and Goddison, 1994)

- If $(Tb_{36V} - Tb_{36H} > 10)$ and $(T \geq 270\ K)$ wet snow **FLAG**
- Otherwise *continue to Step 7*

Step 7 Wet or dry soil screen and Snow Depth (SD) Estimate

- If $\{[(Tb_{36V} - Tb_{18V})/18] \geq -0.3\}$ and $(T \geq 270$ K) and $(T \leq 273$ K) Wet soil snow depth estimate:

$$\mathbf{SD = 1.66(Tb_{18V}-Tb_{36V})} \qquad \mathbf{[cm]}$$

- Otherwise dry soil snow depth estimate:

$$\mathbf{SD = a(Tb_{18V}-Tb_{36V}-5) / (1 - ff)} \qquad \mathbf{[cm]}$$

- *Goto Step 1 for next sample*

January 2001 data set validation

A similar exercise was conducted for a relatively constrained (temporally) data set but which contained many more gauged snow depth measurements. Data were obtained from the WMO's network of approximately 600 stations (many in the GTS network) in the northern hemisphere. MAE and ME calculations were made at four distinct spatial scales to determine whether the Chang and "1.59" algorithms might perform differently. Computations were made at a global scale, North America data, Canadian data and Northern Great Plains data. The results are shown in the time plots in Figure 3. It is clear that the MAE values are, again, similar for both the "1.59" and Chang algorithms. However, the bias in the Chang algorithm is reduced significantly in the Chang algorithm estimates. This is the case at all spatial scales with the anomalous exception of the ME for the Northern Great Plains where the "1.59" algorithm does marginally better.

Again, it was suggested that the reason for the improved bias revealed in the Chang results is due to the fact that the forest effect is incorporated in the algorithm. Figure 4 is similar to Figure 3 except that again, computations of MAE and ME were performed only for pixels with forest fraction greater than 30%. The results support the argument that the Chang algorithm does reduce the overall bias in the estimates caused by forest cover.

Figure 5 Shows visually representation of the two algorithms for 1 January 2001. The left panel is the result of applying the "1.59" algorithm and the right panel is a representation of the Chang algorithm. The same screens (rainfall, mountains etc.) are applied in both algorithms so that the differences between the two retrievals are the spatial variation in snow depth.

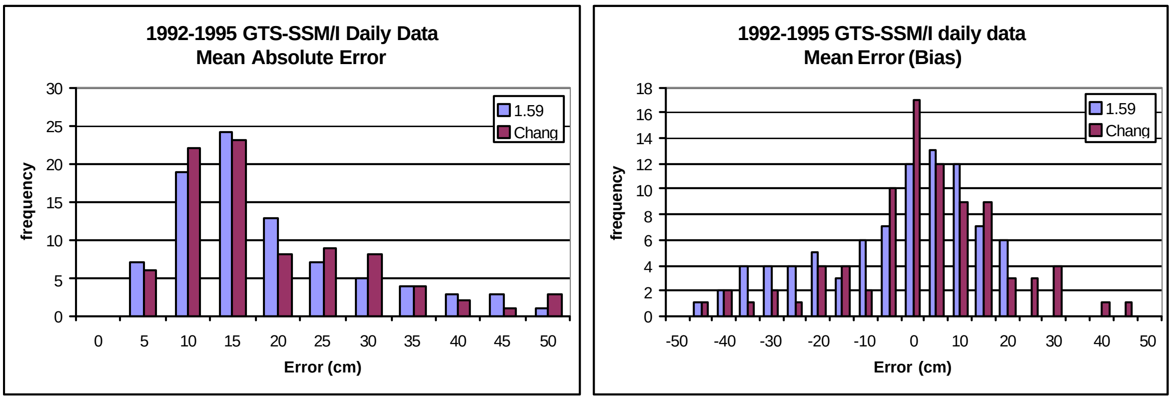

Figure 1. Global validation (mean absolute error and bias) of AMSR (chang) algorithm compared with standard 'static' algorithm (see equation 1) for 86 global GTS snow depth gauge stations.

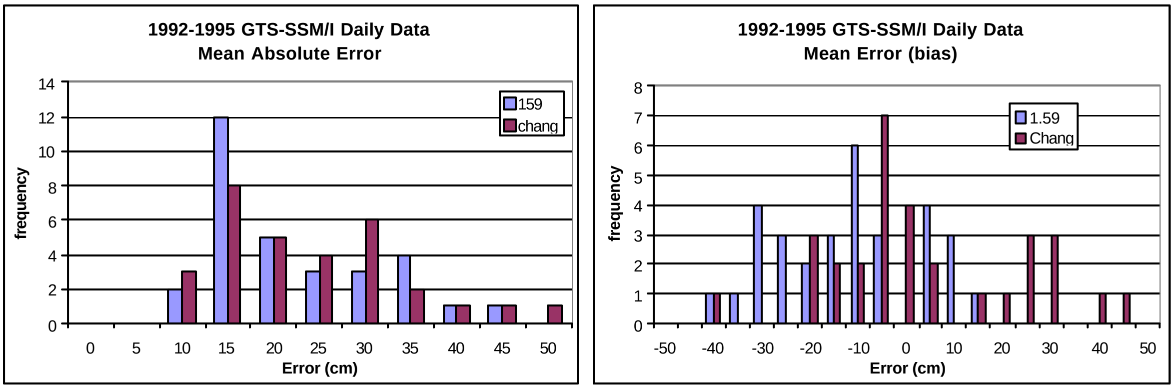

Figure 2. Global validation (mean absolute error and bias) of AMSR (chang) algorithm compared with standard 'static 1.59' algorithm (see equation 1) for 86 global GTS snow depth gauge stations where forest fraction is greater than 30%.

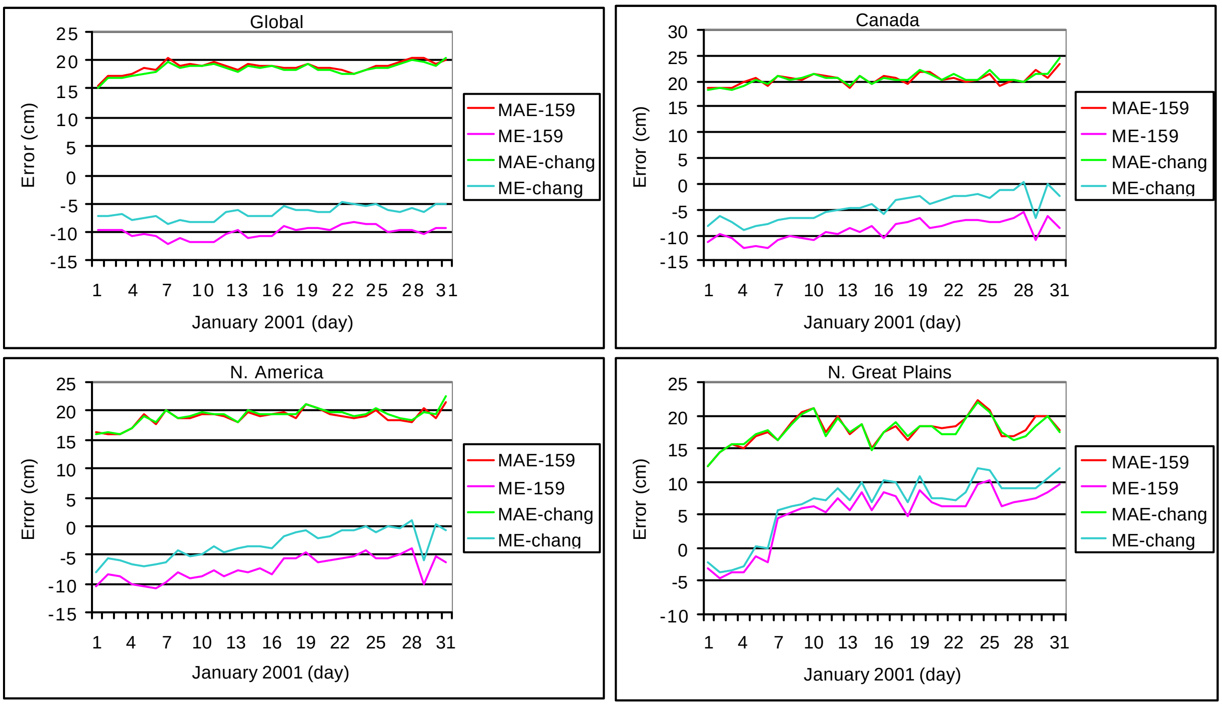

Figure 3. Comparison of 'Chang' and '1.59' snow depth algorithm validation. MAE is the mean absolute error and ME is the mean error (bias). The comparison is for applications of the algorithms in January 2001 and from all stations at global, North America, Canada and Northern Great Plains scales.

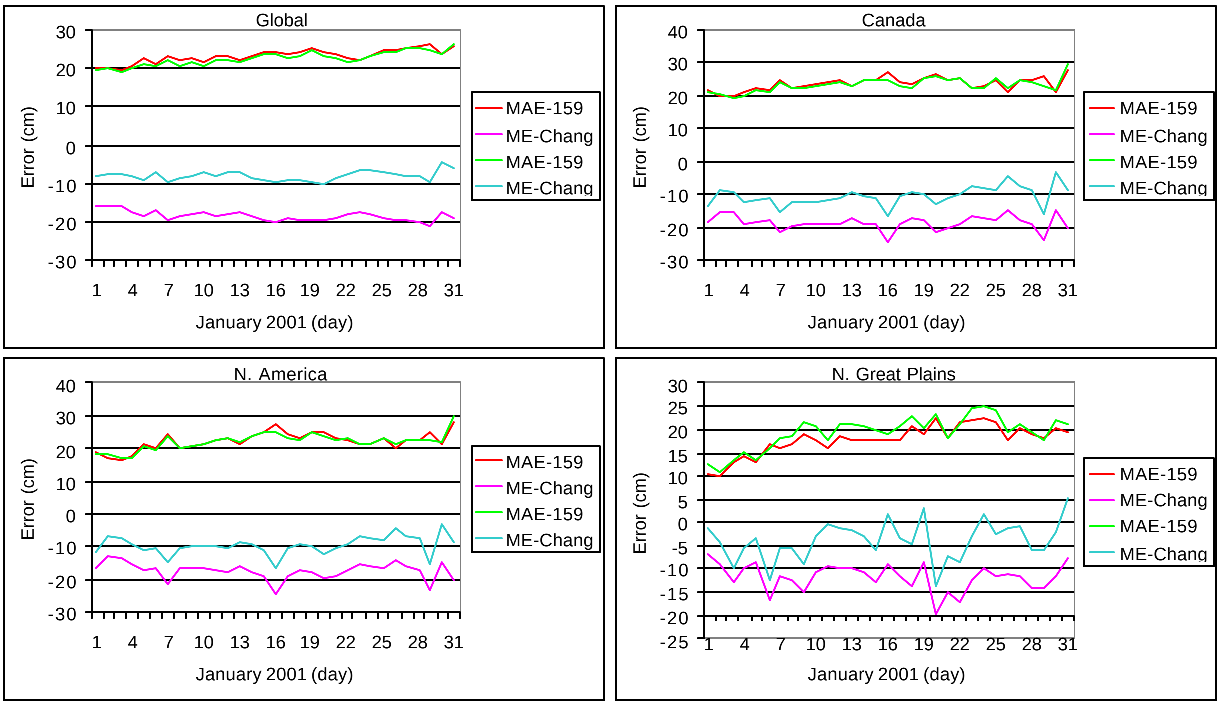

Figure 4. Comparison of 'Chang' and '1.59' snow depth algorithm validation. MAE is the mean absolute error and ME is the mean error (bias). The comparison is for applications of the algorithms in January 2001 for EASE grid pixels that are characterized with forest cover greater than 30% and from all stations at global, North America, Canada and Northern Great Plains scales.

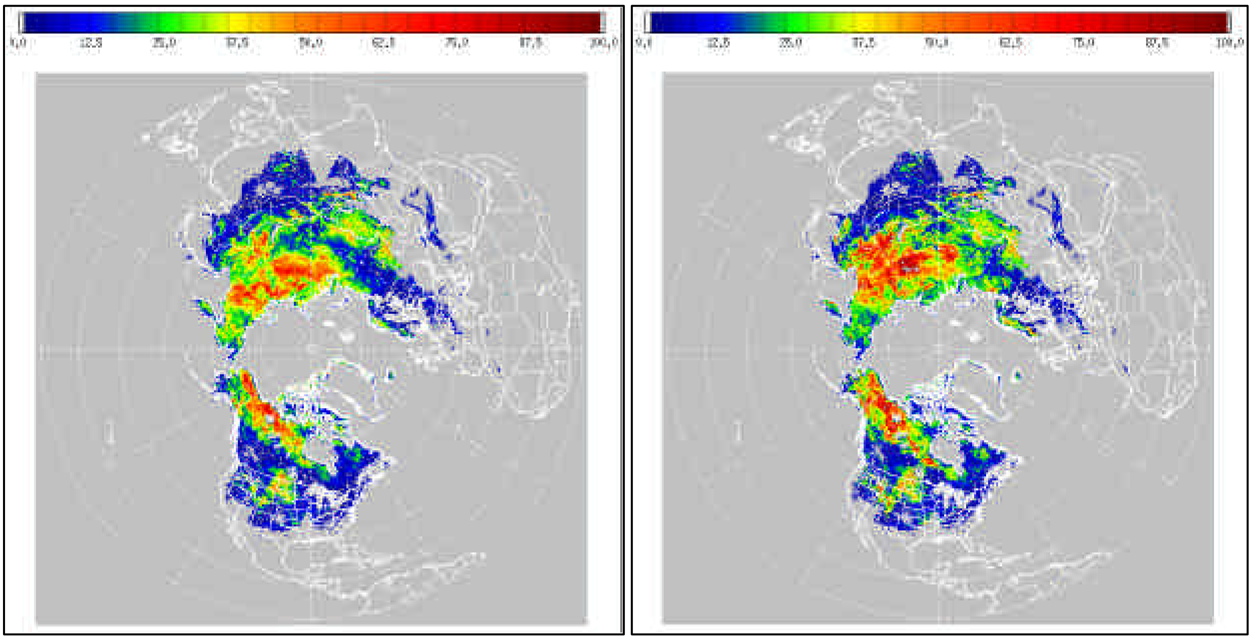

Figure 5. Visualisation of the “1.59” snow depth algorithm (left) and the Chang snow depth algorithm (right) for 1 January 2001. The colour scale units are in cm.

6. Future developments

Results from the work to date are very encouraging and suggests that the new algorithm development should improve the old static coefficient methodology described by equation 1. However, the retrieval residuals or errors still need further constraint. Despite a retrieved error (MAE) of 16.6 cm globally, translating this into a SWE produces a value of 1.6 mm for fresh snow (with a density of 100 kg m^{-3}) and more for seasonal snow with higher density. It is clear, however, that the spatial distribution of the coefficient *a* in equation 3 is important for successful snow depth retrievals. While the Sturm *et al.* (1995) seasonal snow classification is undoubtedly an invaluable global descriptor that can help, newer, more sensitive descriptors are needed that can provide higher spatial resolution for coefficient spatial extrapolation. This is one area that we are currently developing using geostatistics and land cover data sets and results to date are promising (with further reduced ME and reduced MAE values). In addition, it is clear that successful estimation of daily local snow depth variability will benefit from a dynamic temporal component that could be included in the algorithm to determine variations in snowpack properties. While problematic, this aspect is the subject of current development activities.

An important future development that will assist with the algorithm validation and development is our participation in the Cold Land Processes Field Experiment (CLPX) in North American planned for the 2002-2003 winter season in Colorado. This experiment is part of the NASA Global Water and Energy Cycle (GEWEC) initiative, the Global Energy and Water Cycle Experiment (GEWEX) and the GEWEX Americas Prediction Project (GAPP). The broad objectives of the CLPX are to develop our understanding of cold land processes by increasing our ability to characterize the spatial and temporal variability of snow, ice and frozen ground in the natural environment, and to identify and quantify the various uncertainties associated with remote sensing observations and models of cold land processes, thereby improving our abilities to predict the behavior of various cold land processes (NASA, 2001). As part of this, a significant number of field experiments are planned for February and March 2002 and 2003 to measure snowpack parameters intensively in three 25 km x 25 km and 1 km x 1 km cells in Colorado. The measurement suite will include snow depth, SWE, and surface wetness and roughness and various snow descriptors obtained from snow pits. It is planned that this experiment will also have access to ground-based and airborne radiometers plus a suite of satellite observations. The aircraft flight lines will cover several the AMSR foot-prints (25 km x 25 km). Consequently, it is anticipated that several of the outstanding uncertainties associated with snow depth and SWE retrieval form microwave radiometry will be addressed. This information will assist directly with out efforts for the development of ADEOS II AMSR snow depth retrieval algorithm.

References

Armstrong, R.L. and M.J. Brodzik, (1999) A twenty year record of global snow cover fluctuations derived from passive microwave remote sensing data, *5th Conference on Polar Meteorology and Oceanography*, American Meteorological Society. Dallas, TX, 113-117.

Chang, A.T.C., J.L. Foster and D.K. Hall, (1987) Nimbus-7 derived global snow cover parameters, *Annals of Glaciology*, 9, 39-44.

Chang, A.T.C., J.L. Foster and D.K. Hall, (1996) Effects of forest on the snow parameters derived from microwave measurements during the BOREAS winter field experiment. *Hydrological Processes*, **10**: 1565-1574.

Chang, A.T.C. and T. Koike (2000) Progress in AMSR snow algorithm development, in Pampaloni, P. and S. Paloscia (Eds), Microwave Radiometry and Remote Sensing of the Earth's Surface and Atmosphere, VSP, p515-523.

Colbeck, S.C. 1986 Classification of seasonal snow cover crystals, *Water Resources Research*, **22(29)**: 59S-70S.

Dewey, K.F. and R.Heim, Jr. (1981) Satellite observations of variation in Northern Hemisphere seasonal snow cover, NOAA Technical Report NESS 87, 83 pp.

Dewey K.F. and R. Heim, Jr. (1983) Satellite observations of variations in Southern Hemisphere snow cover, NOAA Technical Report NESDIS 1, 20 pp.

Foster, J.L, A.T.C. Chang and D.K. Hall, (1997) Comparison of snow mass estimates from a prototype passive microwave snow algorithm, a revised algorithm and snow depth climatology, *Remote Sensing of Environment*, **62**: 132-142.

Goodison, B. and A. Walker, (1994) Canadian development and use of snow cover information from passive microwave satellite data, In Choudhury, B., Kerr, Y., Njoku, E., and Pampaloni, P. (eds) *Passive Microwave Remote Sensing of Land-Atmosphere Interactions*, Utrecht: VSP BV, 245-62.

Grody, N.C. and A.N. Basist (1996) Global identification of snowcover using SSM/I measurements, *IEEE Transactions on Geoscience and Remote Sensing*, **34(1)**: 237-249.

Josberger, E., P. Gloersen, A. Chang and A. Rango, (1995) Snowpack grain size variations in the upper Colorado River basin for 1984-1992. *Journal of Geophysical Research*, 101, 6679-6688.

Kurvonen, L., J. Pulliainen, M. Hallikainen (1998) Monitoring of boreal forests with multitemporal special sensor microwave imager data, *Radio Science*, **33(3)**: 731-744.

NASA, (2001) NASA Cold Land Proccesses Field Experiment Plan 2002-2004, Cold Land Processes Working Group, NASA/ESE/LSHP, http://lshp.gsfc.nasa.gov.

Robinson, D.A. and G. Kukla, (1985) Maximum surface albedo of seasonally snow covered lands in the Northern Hemisphere. *Journal of Climate and Applied Meteorology* **24**: 402-411.

Sturm, M., J. Holmgren and G.E. Liston, (1995): A seasonal snow cover classification system for local to global applications. *Journal of Climate*, **8**, 1261-1283.

Sun, C.Y, C.M.U. Neale and J.J. McDonnell, (1996): Snow wetness estimates of vegetated terrain from satellite passive microwave data. *Hydrological Processes*, **10:** 1619-1628.

Walker, A., and B. Goodison, (1993) Discrimination of a wet snow cover using passive microwave satellite data, *Annals of Glaciology*, **17**: 307-311.

AMSR Snow Algorithm Development and Validation in the Eurasian continent

Toshio Koike
Department of Civil Engineering, University of Tokyo

The wavelength in the microwave region has sensitivity to the scattering effect of snow grains and leaves. Microwave remote sensing has potential of the measurement of snow water equivalent and water content of vegetation. The longer wavelength is one of the advantages of microwaves. It is long enough to reduce the scattering effect of cloud particles and to make microwave sensors useful all-weather ones. In this study, a new algorithm for snow depth and snow physical temperature by considering the effects of vegetation is developed based on the microwave radiative transfer theory. It is applied to the SSM/I and TMI data and validated by using the in-situ data in Russia and the Tibetan Plateau.

The microwave brightness temperature observed by satellites is expressed by the radiative transfer equation which consists of the soil surface radiation attenuated by snow and vegetation layers and their. A passive microwave sensor algorithm for snow is proposed based on the radiative transfer theory by introducing the effects of vegetation. The relationship between the land surface radiation and snow properties is obtained by the radiative transfer theory based on a scattering dielectric layer over a homogeneous half-space. The total land surface brightness temperature is the sum of the direct component and the diffuse component which corresponds to the reflected sky radiation and the thermal radio emission from snowpack and soil, and the radiation scattered from the direct and diffuse fields, respectively. By assuming snow grain size, snow density and radiation form soil-snow interface, brightness temperatures at two different frequencies are calculated by the radiative transfer equation by inputting snow depth and physical temperature. This forward model calculation was validated through the aircraft experiment in Japan. To evaluate the vegetation effects on microwave radiative transfer, three relationships among optical thickness in microwave region, water content of vegetation, LAI and NDVI. In microwave region, vegetation layer is characterized only by optical thickness, which is expressed by water content of vegetation. Water content of vegetation is related with LAI by using an empirical equation. According to the visible and infrared remote sensing, several relationships between LAI and NDVI were proposed. Based on those three relationships, the effects of vegetation on the microwave radiative transfer can be estimated by NDVI derived from visible and infrared radiometers.

By assuming constant values of snow grain size, snow density and soil surface emissivity, brightness temperatures at two different frequencies are calculated for each snow depth, snow physical temperature and NDVI. By applying a numerical inversion technique to the result of the forward model calculation, we can obtain a look-up table, which calculates snow depth and snow physical temperature by inputting observed brightness temperature at two different frequencies. In this paper, the proposed algorithm is applied to the data at 19GHz and 37GHz of DMSP SSM/I and TRMM TMI. NDVI is derived from NOAA AVHRR data.

A four years (1992-1995) data set based on in-situ measurements and SSM/I data was complied by Earth Observation Research Center (EORC) of National Space Development Agency (NASDA) of Japan. Snow parameters and climatology data from one hundred observational stations spread over the Northern Hemisphere were involved in the data set. Five closest SSM/I footprints were extracted from the swath data to form the coincide data set. A statistical analysis of the proposed algorithm was performed for the period of January 20 to 25, 1993. The algorithm retrieved snow depth at 69 stations from 100 and the mean absolute difference between the observations and estimations is 24.5cm. The algorithm was not able to infer accuracy the snow information from deep snowpacks. This is probably due to the limited penetration of 37GHz radiation.

The Tibetan Plateau has been suggested to play an important role in the variation of the Asian summer monsoon through its atmospheric heating processes. The Intensive Observing Period (IOP) was implemented in 1998 for the purposes of establishing the satellite-based observing systems and clarifying the interactions between the land surface and atmosphere over the Tibetan Plateau. The closest footprints of TMI to the Automatic Weather Stations (AWSs) were used to make a match-up data set. The estimated snow physical temperature is in good agreement with the observed surface temperature by using the infrared thermometer as shown in Fig. 3, although the snow depth has not been validated because the lack of the ground-based snow depth data.

AMSR soil moisture algorithm development and validation

Toshio Koike
Department of Civil Engineering, University of Tokyo

Microwave remote sensing can directly measure the dielectric properties which are strongly dependent on the liquid water content. The longer wavelength is one of the advantages of microwaves. It is long enough to reduce the scattering effect of cloud particles and to make microwave sensors useful all-weather ones. The wavelength in the microwave region has sensitivity to the scattering effect of leaves. Microwave remote sensing has potential of the measurement of water content of vegetation. The independence of sun as a source of illumination is also one of the important reasons for using microwaves. We can obtain the data even in night. This advantage is more important in the case of non-sunsynchronous observation.

Advanced Microwave Scanning Radiaometer (AMSR) is a passive microwave radiometer with frequency ranges from 6.9 GHz to 89 GHz. It will be flown on-board of the United States Earth Observation System (EOS) PM-1, "AQUA", by National Aeronautics and Space Administration (NASA) of the United States and the Advanced Earth Observing Satellite-II (ADEOS-II) by National Space Development Agency (NASDA) of Japan. With a large antenna, AMSR will provide the best spatial resolution of multi-frequency radiometer from space. The spatial resolution of the ADEOS-II AMSR varies from approximately 50km at 6.9 GHz to 5 km at 89 GHz. The AQUA AMSR-E has slightly coarser spatial resolution due to its 1.6m antenna aperture instead of the 2m one for ADEOS-II AMSR. The antenna beams scan by continuous rotation along a conical surface, which intersects the earth's surface at an angle of 55 degree.

Currently, NASDA is developing an AMSR standard algorithm for soil moisture. The proposed algorithms by the selected principle investigators (PIs) are now being carefully tested and evaluated using the SMMR and SMM/I data. There are basically four candidate algorithms. At the time of the test, all algorithms are still under development and subject to changes. Jackson proposes two types of regression algorithms in addition to his basic one. Paloscia adopts two ways for estimation of one parameter, a simple liner regression method and vegetation biomass classification one based on the polarization information. Njoke proposes both empirical and physically- based algorithms.

The match-up data between SMMR and in-situ soil moisture at 79 Former Soviet Union (FSU) agricultural fields were provided by NASDA Earth Observation Research Center (EORC). The soil moisture measurements were conducted at 8th, 18th, and 28th of each month. The algorithm inter-comparison was implemented under the three typical vegetation conditions, which are indicated by the histograms of NDVI distribution in the area corresponding to the SMMR foot print. Paloscia's algorithm works well in three cases due to the effect of regression adjustment. In the case of not so dense vegetation with heterogeneity, the estimated values by Njoke's and Koike's algorithms scatter around the observed ones. Under the uniform and dense vegetation, those two show under estimation or scatter and Jackson's algorithm can not retrieve soil moisture. To evaluate algorithm performance, it is necessary to obtain ground truth data in uniform areas or spatially distributed information in heterogeneous areas.

Heterogeneity is one of the critical issues of passive microwave remote sensing of soil moisture due to large foot print of microwave radiometers, especially at low frequency. A ground-based microwave radiometer (GBMR) was deployed in the SGP99 to respond this scientific requirement.

The GBMR with three frequencies and dual polarization was operated during the SGP99 to provide well controlled observations to enhance algorithm development and aircraft and satellite data validation. Every morning, the radiometer was calibrated by using liquid nitrogen and the ambient hot load just before the operation. It was kept working until the end of operation of the day. Incident angle was 55 degree. 100 samples were taken at each rotation angle by rotating the antenna from –10 degree to + 10 degree with 5 degree interval. Total number of samples is 500 at each point. After ground surface measurement, sky reference was also collected. The gravimetric soil moisture samples of 0 – 2.5cm and 2.5 – 5.0 cm layers were collected at three points which correspond to the centers of foot prints at the rotation angle, -10, 0 and +10 degree at each site. The horizontal soil moisture measurement at 1.0cm, 2.5cm and 5.0cm in depth and the vertical measurement were carried out by using the TDR system at the same points. The infrared thermometer was used for the measurement of surface temperature at the points where the soil samples were collected. The soil temperature profiles were measured at 1.0cm, 5.0cm and 10.0cm in depth at the same points. A spectrometer which covers from 380nm – 2500nm with 1 nm sample interval was used. Seven samples were collected along the soil measurement course in addition to three white board measurements. Two portable surface roughness indicators were used. Two samples, one along north-south direction and the other along east-west, were collected at each site.

The observation shows that the apparent emissivity, Tb/Ts at 6.9 GHz increases as soil moisture increases. It is considered that the soil temperature gradient affect the observed brightness temperature significantly in the dry soil cases. The soil temperature difference between the observed values and the estimated effective values decreases as soil moisture increases. By the simple numerical simulation, the effect of scattering extinction under dry condition causes the brightness temperature increase as soil moisture increase. This means that temperature gradient should be considered in dry case.

Description of Soil Moisture Retrieval Algorithm for ADEOS II AMSR

Thomas J. Jackson
USDA ARS Hydrology and Remote Sensing Lab

1. ALGORITHM DESCRIPTION

To a large degree, the research in microwave remote sensing of soil moisture has focused on the forward modeling problem. This is the process of predicting the brightness temperature from soil properties using radiative transfer theory. When measuring soil moisture we must be concerned with inversion of this model. This is more difficult than forward modeling. There are five steps involved in extracting soil moisture using passive microwave remote sensing. These are; normalizing brightness temperature to emissivity, removing the effects of vegetation, accounting for the effects of soil surface roughness, relating the emissivity measurement to soil dielectric properties, and finally relating the dielectric properties to soil moisture.

In our approach, soil moisture retrieval is based upon an algorithm developed by Jackson (1993). Brightness temperature for a single AMSR channel (6.9 GHz H) is converted to emissivity using a surrogate for the physical temperature of the emitting layer. This emissivity is corrected for vegetation and surface roughness to obtain the soil emissivity. The Fresnel equation is then used to determine the dielectric constant. Finally, a dielectric mixing model is used to obtain the soil moisture. The theory describing this follows.

Fundamental basis for a smooth bare soil. The measurement provided is the brightness temperature, T_B, that includes contributions from the atmosphere, reflected sky radiation, and the land surface. Atmospheric contributions are negligible at frequencies <6 GHz. Galactic and cosmic radiation contribute to sky radiation and have a known value that varies very little in the frequency range used for soil water content observations (T_{sky} ~4 K). The brightness temperature of a surface is equal to its emissivity (e) multiplied by its physical temperature (T).

Based upon the above, the equation for T_B is

$$T_B = eT + [1-e]T_{sky} \tag{1}$$

The second term of equation 1 will be on the order of 2 K and will be dropped for computational purposes. For inversion equation 1 is rearranged as follows

$$e = \frac{T_B}{T} \tag{2}$$

If the physical temperature is estimated independently, emissivity can be determined. This can be done using surrogates based on satellite surface temperature, air temperature observations, or forecast model predictions.

There are two important relationships that must be utilized to relate the sensor measurement to soil water content. In the first it is necessary to link the sensor measurement to a basic property of the soil that changes with water content. By assuming that the target being observed is a plane surface with surface geometric variations and volume discontinuities much less than the frequency, only refraction and absorption of the media need to be considered at low frequencies such as L band (at higher frequencies scattering must be included). This permits the use of the Fresnel reflection equations (Ulaby et al., 1986). These equations predict the surface microwave reflectivity as a function of dielectric constant (relative permittivity) of the target (ε_r) and the viewing angle (Θ) based on the polarization of the sensor, horizontal (H) or vertical (V). At these frequencies the reflectivity is equal to 1 minus the emissivity. The Fresnel equations can be simplified by including only the real part of the complex dielectric constant (the imaginary part of the complex dielectric constant is relatively small and often ignored). This simplification makes it possible to invert the Fresnel equations to solve for ε_r' given the measured emissivity.

$$e_H(\Theta) = 1 - \left| \frac{\cos\Theta - \sqrt{\varepsilon_r - \sin^2\Theta}}{\cos\Theta + \sqrt{\varepsilon_r - \sin^2\Theta}} \right|^2 \tag{3}$$

$$e_V(\Theta) = 1 - \left| \frac{\varepsilon_r \cos\Theta - \sqrt{\varepsilon_r - \sin^2\Theta}}{\varepsilon_r \cos\Theta + \sqrt{\varepsilon_r - \sin^2\Theta}} \right|^2 \tag{4}$$

For a bare soil surface, the target consists of an interface of air and soil plus a shallow contributing layer at the top of the soil column. Since the dielectric constant of air is a known value (~1), the reflectivity provides a measurement of the dielectric constant of the soil. The Fresnel equations apply when the two media at the interface each have uniform dielectric properties within the contributing depth. Although this is certainly valid for air, however, for a soil surface this is not always a valid assumption. It should also be noted that the basic formulations in equations 3 and 4 result in a larger dynamic range or sensitivity of emissivity to changes in the dielectric constant for H polarization. It is possible to invert equation 3 to solve for the dielectric constant given the measured emissivity.

The next critical relationship involves relating this derived dielectric constant to volumetric soil water content. The dielectric constant of soil is a composite of the values of its components: air, soil and water. Although the dielectric constant is a complex number, for soil mixtures the real part is much more important and variable. Values of the real part of the dielectric constant for air and soil particles are approximately 1 and 5, respectively. For water the value of the dielectric constant varies with frequency and is about 80 at the lower frequencies considered here (<6 GHz) (Ulaby et al., 1986).

The basic reason microwave remote sensing is capable of providing soil water content information is this large dielectric difference between water and the other soil components. Since the dielectric constant is a volume property, the volumetric fraction of each component must be considered. The computation of the mixture dielectric constant (soil, air and water) has been the subject of several studies and there are different theories as to the exact form of the mixing equation (Schmugge, 1980 and Dobson et al., 1985). A simple linear weighting function is typically used.

The dielectric constant of water referred to above is that of free water in which the molecules are free to rotate and align with an electrical field. It has been recognized for some time that not all the water in soil satisfies this condition. Schmugge (1980) suggested that some water in the soil had different properties. He proposed that for a given soil this could be estimated using soil texture in much the same way that pedo-transfer functions are used to estimate 15 bar and 1/3 bar water contents based on texture (Rawls et al., 1993). He proposed that the initial water added to dry soil below a "transition" water content were held more tightly by the soil particles and had the dielectric properties of frozen water (~3).

Vegetation and Surface Roughness. For natural conditions, varying degrees of vegetation will be encountered. The presence of vegetation will have a major impact on the microwave measurement. Vegetation reduces the sensitivity of the retrieval algorithm to soil water content changes by attenuating the soil signal and by adding a microwave emission of its own to the microwave measurement. The attenuation increases as frequency increases. This is an important reason for using lower frequencies. As described in Jackson and Schmugge (1991), at lower frequencies it is possible to correct for vegetation using a vegetation water content-related parameter.

When there is vegetation, the observed emissivity is a composite of the soil and vegetation. To retrieve soil water content it is necessary to isolate the soil surface emissivity (e^{surf}). Following Jackson and Schmugge (1991), the equation describing this is

$$e_p = [1 - \alpha_{p,f,v}][1 - \gamma_{p,f,v}][1 + [1 - e_p^{surf}]\gamma_{p,f,v}] + e_p^{surf}\gamma_{p,f,v} \tag{5}$$

Both the single scattering albedo (α) and the one-way transmissivity of the canopy (γ) are dependent upon the vegetation structure (v), polarization (p) and frequency (f).

The transmissivity is a function of the optical depth (τ) as described by the following equation

$$\gamma_{p,f,v} = \exp[-\tau_{p,f,v} \sec \Theta] \qquad (6)$$

At low frequencies the single scattering albedo can be assumed to be negligible, then substituting equation 6 into equation 5 and rearranging yields

$$e_p^{surf} = 1 + [e_p - 1] \exp[-2\tau_{p,f,v} \sec \Theta] \qquad (7)$$

The vegetation optical depth is also dependent upon water content (W). In studies reported in Jackson et al. (1982) and Jackson and Schmugge (1991), it was found that the following functional relationship between the optical depth and vegetation water content could be applied

$$\tau_{p,f,v} = b_{p,f,v} W \qquad (8)$$

There is a limited database of values of b available. The vegetation water content can be estimated using a variety of ancillary data sources. One approach is to establish a relationship between w and a satellite based vegetation index such as the Normalized Difference Vegetation Index (NDVI) as described in Jackson et al. (1999).

The emissivity that results from the vegetation correction is that of the soil surface. This includes the effects of surface roughness. These effects must be removed in order to determine the soil emissivity (e^{soil}) which is required for the Fresnel equation inversion. One approach to removing this effect is a model described in Choudhury et al. (1979) that yields the bare smooth soil emissivity

$$e_p^{soil} = 1 - [1 - e_p^{surf}] \exp[-h_{p,f,g} \cos^2 \Theta] \qquad (9)$$

The parameter h is dependent upon the polarization, frequency and geometric properties (g) of the soil surface. Typically, values are assigned based upon land use and tillage (Choudhury et al., 1979 and Jackson et al., 1999).

2. OPERATIONAL IMPLEMENTATIONN

For each AMSR pixel, the latitude and longitude (from the input file) are used to cross reference to the land cover and NDVI ancillary data files. The third set of ancillary data files representing soil texture and porosity, is not mapped to any projection and the resolution is 0.083 degrees. The AMSR footprint is readily located in the soil texture file and its latitude and longitude are retrieved from the input file.

Land cover is first used to screen the data for the selected number of categories that can be inverted for soil moisture. This also removes water pixels. The next step is another screening to check for anomalous T_B values. Following this, an index developed by Ferraro et al. (1994) is used to screen out pixels with active rainfall. The final screening is a check of the surface air temperature from the AMSR files versus T_B.

Having passed all of the tests above, the footprint data is used to compute soil moisture. T_B is divided by an adjusted surface air temperature to estimate emissivity.

Vegetation correction is performed using the pixel NDVI to compute the vegetation water content. Surface roughness effects are removed utilizing a single roughness parameter, fixed at 0.1 at this time.

The net result of these corrections is the soil emissivity. From this the dielectric constant of the soil is computed. The value of the dielectric constant is then used with the dielectric mixing model and the soil texture and porosity to compute the volumetric soil moisture.

3. ANCILLARY DATA SOURCES

Land Cover

The University of Maryland Geography Department produced a global land cover data base at a resolution of 8 km which is available at http://glcf.umiacs.umd.edu/. The codes for the land covers are as follows;

1	Evergreen Needleleaf Forests
2	Evergreen Broadleaf Forests
3	Deciduous Needleleaf Forests
4	Deciduous Broadleaf Forests
5	Mixed Forests
6	Woodlands
7	Wooded Grasslands/Shrubs
8	Closed Bushlands or Shrublands
9	Open Shrublands
10	Grasses
11	Croplands
12	Bare
13	Mosses and Lichens

AMSR data over areas covered by cover types 1 – 6 cannot be used for retrieving soil moisture due to the effects of forests. Data over cover types 7 – 10 and 12 – 13 can be used for retrieval. Croplands are considered for soil moisture retrieval if the NDVI is less than 0.5. Thus, the new land cover types are:

0	ocean and inland water – more than 20% of footprint covered by ocean or by inland water
1	good for retrieval – more than 60% of footprint covered by wooded grasslands/shrubs, closed bushlands or shrublands, open shrublands, grasses, bare, mosses and lichens
2	reasonable for retrieval – categories listed in 1. occupied more than 30% of footprint and croplands less than 30%
3	conditional for retrieval – categories listed in 1. occupied less than 30% of footprint and croplands over 30%
4	limited for retrieval – more than 60% of footprint covered by croplands
5	unable for retrieval – more than 30% of footprint covered by evergreen needleleaf, evergreen broadleaf, deciduous needleleaf, deciduous broadleaf, and mixed forests and woodlands

NDVI

The technique used to incorporate vegetation effects requires NDVI information. These products are available from various sources and can be acquired and updated to reflect current conditions. The GLI team may generate data products that can be used for this purpose. However, since this is a research algorithm and arrangements to import ancillary data sets such as NDVI are not in our control, we are providing an alternative that should be adequate for most conditions in soil moisture retrieval.

We are providing a series of NDVI data sets that represent the historical averages for each 10 day period throughout the year. The algorithm will retrieve the NDVI data set that is closest in time (day of the year) to the observation date for the AMSR data. This NDVI data set then represents the average condition expected for this date. The quality of the estimate will depend upon how the current year deviates from the average. It might be possible in the future to adjust these values for the current conditions by tracking climatological information and comparing this to the year to year conditions in the records.

To develop the historical averages we used the Pathfinder AVHRR Land data sets. These are global, land surface data derived from the Advanced Very High Resolution Radiometers (AVHRR) on the NOAA/TIROS operational meteorological satellites (NOAA-7, -9, and –11) that have provided continuous daily and composite data set from July 1981 through the present. The daily and composite products include 12 data layers, (NDVI, CLAVR flag, QC flag, Scan Angle, Solar Zenith Angle, Relative Azimuth Angle, Ch 1 Reflectance, Ch 2 Reflectance, Ch 3 Brightness Temperatures, Ch 4 Brightness Temperatures, Ch 5 Brightness Temperatures, and Day of Year). The composite is generated by comparing the NDVI values for each 8 km bin from 10 consecutive Daily Data Sets. Because data at the edge of a scan may contain distortion and bi-directional effect biases, only data within 42 degrees of nadir are used in the composite. For each 8 km pixel, the day with the highest NDVI during a 10 day period is chosen as the date for inclusion in the composite, and all 12 data layers are updated with data from that date. This composite process is effective for removing most of the clouds and atmospheric contaminants, thus providing as close to a cloud free field in each of the data layers as is possible (Holben, 1986). There are three composites per month. The first composite of each month is for days 1 to 10, the second composite is for days 11 to 20, and the third composite is for the remaining days.

The NOAA/NASA Pathfinder Land data team has completed their software development and data reprocessing. Their data are distributed by the Goddard Distributed Active Archive Center (DAAC) (ftp://daac.gsfc.nasa.gov/data/avhrr/global_8km). Data are available from July 13, 1981 to the present. For this analysis, we only used data from 1982 to 1999. The NDVI composite is mapped in a global 8 km equal area grid using the Goode Interrupted Homolosine projection. There are (36*18) data sets. The original AVHRR Pathfinder NDVI 8 km 10-day composite data from 1982 to 1999 that were used in our processing are on CDROMs (18 of them).

For each pixel in a 10-day composite data set which is not ocean, inland water or filler, all data points that fall in a 7x7 box centered at that pixel were averaged. In the averaging process, if there were any ocean, inland water or filler pixels in the 7x7 box, these were not included in the average computation. After this process was completed for each individual NDVI data set, the values for each 10 day interval were averaged over the 18 year record to produce the average annual time series 10-day composite.

Soil Texture

The soil texture and porosity data sets are a result of a study to estimate global soil water-holding capacities by linking the Food and Agriculture Organization (FAO) soil map of the world with global pedon databases and continuous pedotransfer functions (PTF) (Reynolds et al., 2000). The FAO-UNESCO Soil Map of the World (SMW) at 1:5,000,000 is the most comprehensive soil map with global coverage. Great efforts have been made to relate the FAO soil units to physical soil characteristics by statistically analyzing global pedon databases to estimate soil texture, bulk density and organic matter content. The data set images produced by Reynolds et al. (2000) have a 5-min spatial resolution to preserve the spatial integrity of the SMW, which is equivalent to a 9 km x 9 km cell size at equator. Soil properties were estimated at two depths, i.e., 0-30 cm and 30-100 cm. Only the 0-30 cm depth is needed here. Three of these soil properties were placed in the ancillary directory; clay content, sand content and porosity.

4. REFERENCES

Choudhury, B. J., Schmugge, T. J., Chang, A. T. C., and Newton, R. W. 1979. Effect of surface roughness on the microwave emission of soils. J. Geophysical Research, 84:5699-5705.

Dobson, M. C., Ulaby, F. T., Hallikainen, M. T., and El-Rayes, M. A. 1985. Microwave dielectric behavior of wet soil, II, Dielectric mixing models. IEEE Trans. Geoscience and Remote Sensing, GE-23:35-46.

Ferraro, R. R., Grody, N. C., and Marks, G. F. 1994. Effects of surface conditions on rain identification using the DMSP-SSM/I. Remote Sensing Reviews, 11:195-209.

Holben, B. N. 1986. Characteristics of maximum-value composite images from temporal AVHRR data. International Journal of Remote Sensing, 7:1417-1434.

Jackson, T. J. 1993. Measuring surface soil moisture using passive microwave remote sensing. Hydrological Processes, 7:139-152.

Jackson, T. J. and Schmugge, T. J. 1991. Vegetation effects on the microwave emission from soils. Remote Sensing of Environ., 36:203-212.

Jackson, T. J., Schmugge, T. J., and Wang, J. R. 1982. Passive microwave remote sensing of soil moisture under vegetation canopies. Water Resources Research, 18:1137-1142.

Jackson, T. J., Le Vine, D. M., Hsu, A. Y., Oldak, A., Starks, P. J., Swift, C. T., Isham, J. and Haken, M. 1999. Soil moisture mapping at regional scales using microwave radiometry: the Southern Great Plains hydrology experiment. IEEE Trans. On Geoscience and Remote Sensing, 37: 2136-2151.

fRawls, W. J., Gish, T. J., and Brakensiek, D. L. 1993. Estimating soil water retention from soil physical properties and characteristics. Advances in Soil Sciences, 16:213-234.

Reynolds, C. A., Jackson, T. J., and Rawls, W. J. 2000. Estimating soil water-holding capacities by linking the Food and Agriculture Organization soil map of the world with global pedon databases and continuous pedotransfer functions. Water Resources Research, 36:3653-3662.

Schmugge, T. J. 1980. Effect of texture on microwave emission from soils. IEEE Trans. on Geoscience and Remote Sensing GE-18:353-361.

Ulaby, F. T., Moore, R. K., and Fung, A. K. 1986. Microwave remote sensing: active and passive, Vol. III, from theory to application. Artech House, Dedham, MA.

The IROE algorithm

Simonetta Paloscia
Consiglio Nazionale delle Ricerche,Istituto di Ricerca sulle Onde Elettromagnetiche

On the basis of experimental results, obtained in past years by IROE Microwave Remote Sensing Group, it has been stated that the brightness temperature (Tb) of microwave emission measured at C-band (6.8 GHz) is able to estimate soil moisture content (SMC) in different conditions of roughness and vegetation biomass, provided that a correction for the presence of vegetation is introduced. An algorithm has been proposed for computing SMC and correcting the effects of vegetation by using the sensitivity of Polarization Index ($PI=Tb_V-Tb_H/Tb_V+Tb_H$) at X-band (10 GHz) to biomass.

The relation between the brightness temperature (Tb) at C-band and the soil moisture of bare soils has the following generic form:

$$SMC = M + N * Tb_C$$

When the soil is covered by vegetation, the slope (N) of the regression line decreases and the intercept (M) may also change. On the other hand, the (PI) at higher frequencies and in particular at X-band is more sensitive to the vegetation biomass, and can discriminate between several levels of Leaf Area Index (LAI) [Paloscia and Pampaloni 1988]. We can therefore assume that PI at X-band could be related to the slope (N) and intercept (M) of the regression line between PI at C-band and SMC, according to equations of the following type:

$$M = a + b * PI_X \qquad \text{and} \qquad N = a' + b' * PI_X$$

Substituting these relationships in equation (3), we can choose more adequate coefficients for the regression line of SMC retrieval, which becomes:

$$SMC= [a + b * PI_X] – [a'+ b' * PI_X] * Tb_C$$

This procedure can be summarized in the flow-chart of Fig.1.

This algorithm was first tested on microwave data sets collected on agricultural area using IROE airborne radiometers at C and X band. A comparison of SMC retrieved from radiometric measurements with SMC measured on the ground, is shown in Fig. 2, which refers to experimental data collected in the agricultural area of *"Les Alpilles"* in Southern France [Macelloni et al, 2000]. The resulting correlation coefficient is R=0.78 and the standard error of estimate is SE=4.31.

The algorithm was subsequently validated to a larger scale by using satellite data from SMMR. NASDA kindly provided us with a data set of SMMR collected over 79 Russian agro-meteorological stations during a period of about 3 years (from October 1978 to December 1981), together with the corresponding ground-measured values of gravimetric SMC. The latter data, archived by Dr. K. Masuda and Dr. V. Savelin, represented the average value of the first 10-cm layer: they were obtained, with a time interval of 10 days, from April to October. Five SMMR data were picked up within an area around the target station.

From the analysis of these data sets, the slope and the intercept of the regression line $SMC=M+ N*Tb_C$ were related to the corresponding values of PI at X-band (PI_X). In this case, we found that:

$$M= 60.5+7* (PI_X)$$

And

$$N= 0.0008 – 0.2156*Ln(PI_X)$$

The final equation for the retrieval of SMC therefore becomes:

$$SMC = [60.5+7* (PI_X)] + [0.0008 - 0.2156*Ln(PI_X)] *Tb_C$$

The results of this algorithm is shown in the diagram of Fig. 3, where SMC measured on the ground was compared with SMC computed from SMMR data with the algorithm. Although the dispersion of experimental data is rather high, we see that, at least for some ground stations, the algorithm is able to retrieve reasonable data of SMC with R on the order of 0.70 and SE ranging between 3 and 9 [Paloscia et al. 2001]. The main problem of this validation lies on the considerable coarse ground resolution of the SMMR at C-band. The retrieval of SMC can work only in the case of highly homogeneous areas, for which the SMC values measured at the agro-meteorological station can be assumed to be representative of the entire surrounding zone. Other problems were due to the poor calibration accuracy between the two polarization channels.

References

G. Macelloni, S. Paloscia, P. Pampaloni, R. Ruisi, C. Susini, 2000, “Airborne Microwave Radiometer Measurements on Agricultural Fields”, in ‘Microwave Radiometry of Earth’s Surface and Atmosphere’, (Pampaloni & Paloscia Eds), pp. 59-69, VSP press, Utrecht, The Netherlands

Paloscia S. and P. Pampaloni, , "Microwave Polarization Index for Monitoring Vegetation Growth", *IEEE Trans. on Geoscience and Remote Sensing*, GE-26, n. 5, pp. 617-621, 1988

S. Paloscia, G. Macelloni, E. Santi, and Toshio Koike, 2001, “A Multifrequency Algorithm for the Retrieval of Soil Moisture on a Large Scale using Microwave Data from SMMR and SSM/I Satellites, IEEE Trans.on Geosci. and Remote Sensing, Special Issue on Soil Moisture, vol.39, 8, pp. 1655-1661

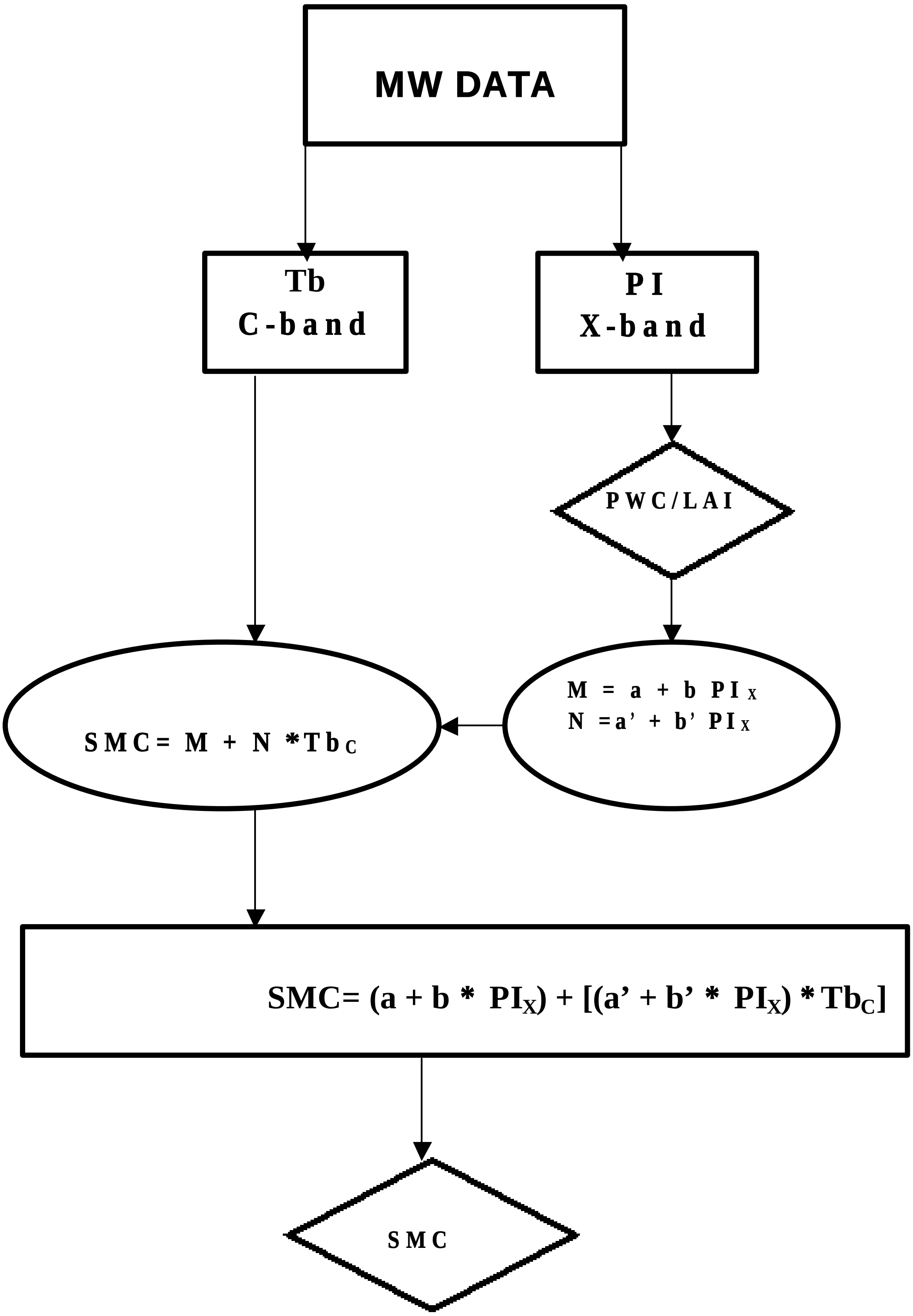

Fig. 1 – The proposed algorithm

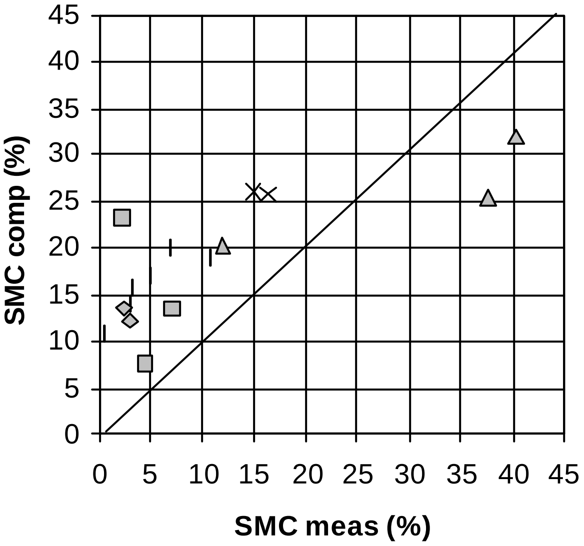

Fig. 2 - SMC % estimated with the algorithm as a function of SMC % of the first 5 cm layer measured on ground. The line represents the 1:1 line. Symbols refer to different crop types: = alfalfa, ▲= bare soil, x = sunflower, ♦ = wheat.

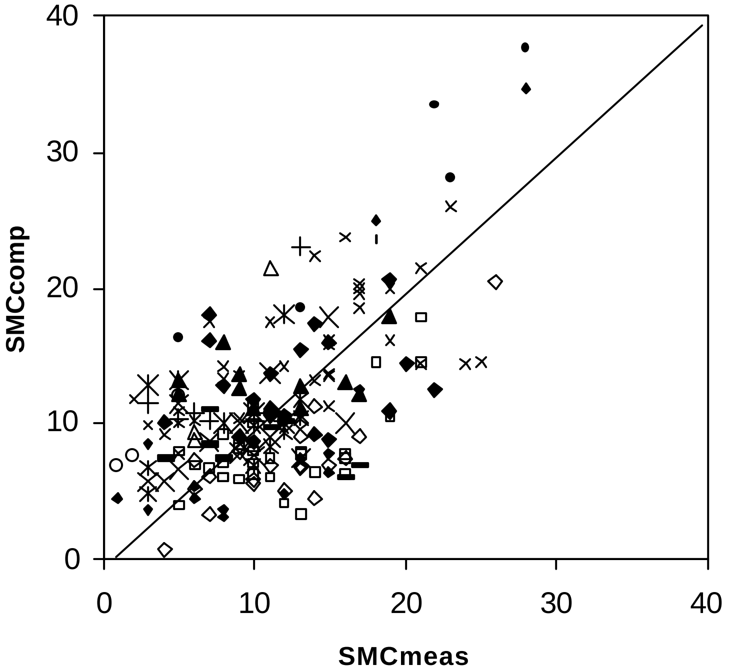

Fig. 3 - SMC% estimated from SMMR data of Tb at C-band vs. SMC% measured on ground. Different symbols refer to different Russian stations.

ADEOS-II AMSR Soil Moisture Algorithm

E. Njoku
Jet Propulsion Laboratory

The soil moisture algorithm involves a series of steps beginning with quality control of the input data followed by re-sampling of the data, surface type classification, screening of the data for retrieval, and inversion of the brightness temperatures to obtain soil moisture. A flowchart of the algorithm is shown in Figure 1.

Re-sampling of the data to an Earth-fixed grid is done to facilitate the surface type classification and retrieval steps. These steps use external data bases to identify water bodies, mountainous areas, soil texture, and other surface features. The surface type classification includes generation of flags that indicate snow, frozen ground, dense vegetation, or precipitation, where retrievals are either not possible or are likely to be of degraded quality.

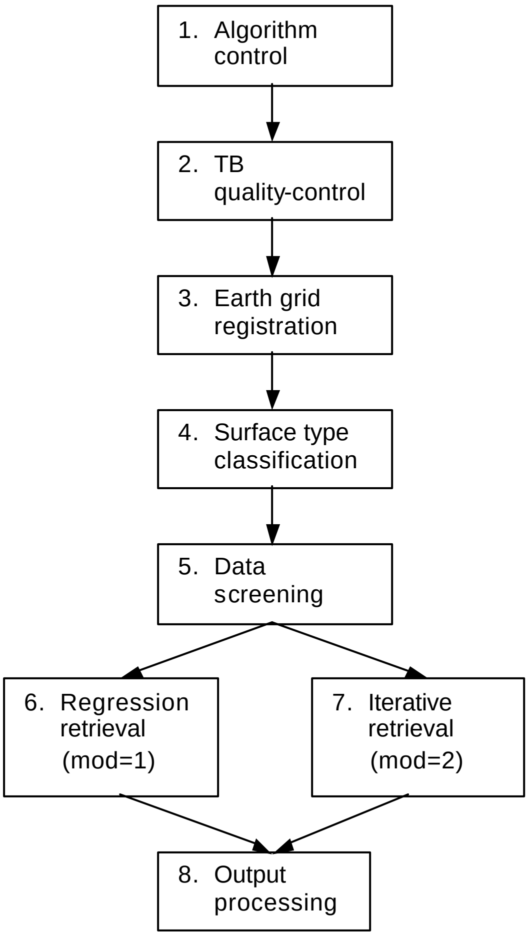

Fig. 1 Flowchart of the algorithm

The surface type flags are qualitative and are generated primarily to assist in screening the data and interpreting the soil moisture retrievals.

The algorithm is a model-based iterative retrieval using the model and approach described in Njoku and Li (1999). This model expresses the brightness temperature observed by AMSR at a particular frequency as:

$$T_{B_p} \; = \; T_e \left\{ \, (1 - r_{sp}) \exp \, (- t_c) + (1 - w_p) \, [\, 1 - \exp \, (- t_c) \,] \, [\, 1 + r_{sp} \, \exp \, (- t_c) \,] \, \right\}$$

where, T_e is the surface temperature; r_{sp} is the surface reflectivity, which is related to the volumetric soil moisture m_v through the Fresnel equations; w_p is the vegetation single scattering albedo, and t_c is the vegetation opacity, which is modeled as linearly related to the vegetation water content w_c. Fixed values are used for w_p and surface roughness height (which affects r_{sp}). The algorithm provides internal corrections for T_e and t_c in deriving m_v, through the use of information contained in the multichannel estimation. At each retrieval point the algorithm finds the set of T_e, t_c and m_v that minimize the weighted sum of squared differences between observed and model-computed multichannel brightness temperatures. Weights are used to select among the lowest six channels (6.9, 10.6, & 18 GHz; V & H). A backup algorithm mode uses a regression equation that is empirically based and is implemented as an alternate means for evaluating anomalous situations, such as where the iterative algorithm fails to converge. This mode uses a combination of the six lowest frequency AMSR channels with coefficients derived from Nimbus-7 SMMR data.

Njoku, E. and L. Li, “Retrieval of land surface parameters using passive microwave measurements at 6–18 GHz,” *IEEE Trans. Geosci. Rem. Sens., 37*, 79–93, 1999